National Library of Canada
Bibliothèque nationale du Canada

Canadian Theses Service
Services des thèses canadiennes

Ottawa, Canada
K1A 0N4

CANADIAN THESES

THÈSES CANADIENNES

NOTICE

The quality of this microfiche is heavily dependent upon the quality of the original thesis submitted for microfilming. Every effort has been made to ensure the highest quality of reproduction possible.

If pages are missing, contact the university which granted the degree.

Some pages may have indistinct print especially if the original pages were typed with a poor typewriter ribbon or if the university sent us an inferior photocopy.

Previously copyrighted materials (journal articles, published tests, etc.) are not filmed.

Reproduction in full or in part of this film is governed by the Canadian Copyright Act, R.S.C. 1970, c. C-30. Please read the authorization forms which accompany this thesis.

AVIS

La qualité de cette microfiche dépend grandement de la qualité de la thèse soumise au microfilmage. Nous avons tout fait pour assurer une qualité supérieure de reproduction.

S'il manque des pages, veuillez communiquer avec l'université qui a conféré le grade.

La qualité d'impression de certaines pages peut laisser à désirer, surtout si les pages originales ont été dactylographiées à l'aide d'un ruban usé ou si l'université nous a fait parvenir une photocopie de qualité inférieure.

Les documents qui font déjà l'objet d'un droit d'auteur (articles de revue, examens publiés, etc.) ne sont pas microfilmés.

La reproduction, même partielle, de ce microfilm est soumise à la Loi canadienne sur le droit d'auteur, SRC 1970, c. C-30. Veuillez prendre connaissance des formules d'autorisation qui accompagnent cette thèse.

THIS DISSERTATION
HAS BEEN MICROFILMED
EXACTLY AS RECEIVED

LA THÈSE A ÉTÉ
MICROFILMÉE TELLE QUE
NOUS L'AVONS REÇUE

NL 339 (r. 86/01)

Canada

National Library of Canada
Bibliothèque nationale du Canada

125

Ottawa, Canada
K1A 0N4

TC –

ISI 0-315-23322-2

CANADIAN THESES ON MICROFICHE SERVICE – SERVICE DES THÈSES CANADIENNES SUR MICROFICHE

PERMISION TO MICROFILM – AUTORISATION DE MICROFILMER

• Please print or type – Écrire en lettres moulées ou dactylographier

AUTHOR – AUTEUR

Full Name of Author – Nom complet de l'auteur

CARL KAR-KUI CHAN

Date of Birth – Date de naissance
11th Dec, 1958

Canadian Citizen – Citoyen canadien
☐ Yes / Oui ☑ No / Non

Country of Birth – Lieu de naissance
Hong Kong

Permanent Address – Résidence fixe
4D Humbert Street,
11th FL, M.F.S.C, Kln, HK

THESIS – THÈSE

Title of Thesis – Titre de la thèse

The Elastic Scattering of Intermediate Energy Protons From Oxygen

Degree for which thesis was presented
Grade pour lequel cette thèse fut présentée
M. Sc

Year this degree conferred
Année d'obtention de ce grade
1985

University – Université
Univ. of Alberta

Name of Supervisor – Nom du directeur de thèse
Dr W. C. Olsen

AUTHORIZATION – AUTORISATION

Permission is hereby granted to the NATIONAL LIBRARY OF CANADA to **microfilm** this thesis and to **lend** or **sell copies of the film.**

The author reserves other publication rights, and neither the thesis nor extensive extracts from it may be printed or otherwise reproduced without the author's written permission.

L'autorisation est, par la présente, accordée à la BIBLIOTHÈQUE NATIONALE DU CANADA de **microfilmer** cette thèse et de **prêter** ou de **vendre des exemplaires du film.**

L'auteur se réserve les autres droits de publication; ni la thèse ni de longs extraits de celle-ci ne doivent être imprimés ou autrement reproduits sans l'autorisation écrite de l'auteur.

ATTACH FORM TO THESIS – VEUILLEZ JOINDRE CE FORMULAIRE À LA THÈSE

Signature
Carl Chan

Date
14th May, 1985

NL-91 (r. 84/03)

Canada

THE UNIVERSITY OF ALBERTA

THE ELASTIC SCATTERING OF INTERMEDIATE ENERGY PROTONS FROM OXYGEN

by

CARL KAR-KUI CHAN

A THESIS

SUBMITTED TO THE FACULTY OF GRADUATE STUDIES AND RESEARCH

IN PARTIAL FULFILMENT OF THE REQUIREMENTS FOR THE DEGREE

OF MASTER OF SCIENCE

IN

NUCLEAR PHYSICS

DEPARTMENT OF PHYSICS

EDMONTON, ALBERTA

FALL 1985

THE UNIVERSITY OF ALBERTA

RELEASE FORM

NAME OF AUTHOR CARL KAR-KUI CHAN

TITLE OF THESIS THE ELASTIC SCATTERING OF INTERMEDIATE ENERGY PROTONS FROM OXYGEN

DEGREE FOR WHICH THESIS WAS PRESENTED MASTER OF SCIENCE

YEAR THIS DEGREE GRANTED FALL 1985

Permission is hereby granted to THE UNIVERSITY OF ALBERTA LIBRARY to reproduce single copies of this thesis and to lend or sell such copies for private, scholarly or scientific research purposes only.

The author reserves other publication rights, and neither the thesis nor extensive extracts from it may be printed or otherwise reproduced without the author's written permission.

(SIGNED) Carl Chan

PERMANENT ADDRESS:

c/o Dept. of Physics
University of Alberta
Edmonton, Alberta

DATED 1st May, 1985

THE UNIVERSITY OF ALBERTA

FACULTY OF GRADUATE STUDIES AND RESEARCH

The undersigned certify that they have read and recommend to the Faculty of Graduate Studies and Research for acceptance a thesis entitled THE ELASTIC SCATTERING OF INTERMEDIATE ENERGY PROTONS FROM OXYGEN submitted by Carl Kar-Kui CHAN in partial fulfillment of the requirements for the degree of MASTER OF SCIENCE in Physics.

.....
Supervisor

.....

.....

.....

.....
External Examiner

Date 1st May, 1985

Abstract

We measured differential cross section angular distributions for protons scattered by oxygen-16 at 200, 300, 400, and 500 MeV. This newly obtained data are used to renormalize previously measured differential cross sections. The analyzing power angular distributions obtained in earlier running periods together with the combined set of differential cross section angular distributions are fitted with the non-relativistic optical model. The simple Woods-Saxon form factors are used for the potential shapes.

We were able to obtain relatively unambiguous parametrizations for the 200, 400 and 500 MeV data. However, we discovered substantial ambiguities in the 300 MeV parametrization: two very different parametrizations were found, neither of these falls in line with that of the neighbouring energies.

It has been indicated (El 66) that at energies between 200 and 600 MeV where the real central potential changes progressively from attractive to repulsive, the potential shape differs from that of the nuclear density distribution which was found to be appropriate at lower or higher energies. Theoretical calculations have shown that a pocket of minimum potential is present near the nuclear surface at the intermediate energies, in contrast to the monotonic Woods-Saxon shape. We conclude that the abnormal behaviour of the 300 MeV parametrization is probably due to the shape of the Woods-Saxon functions being substantially different

from that of the potential at this energy..

Acknowlegments

I would like to express my deep gratitude to my supervisor, Dr. W.C. Olsen, for his guidance and encouragement during the course of this work.

I wish to thank Dr. D.A. Hutcheon for his guidance during my stay at TRIUMF and his many useful suggestions on the data analysis, and Dr. H.S. Sherif for his advice on the theoretical aspects of this work.

Table of Contents

Chapter		Page
1.	Introduction	1
2.	Theory	4
	2.1 Scattering Theory	4
	2.2 Phase Shift Calculation	11
	2.3 Elastic Scattering of Spin-1/2 Particles From Spin-zero Targets	12
	2.4 The Optical Model	16
	2.4.1 The Phenomenological Optical Model	16
	2.4.2 Formal Theory of The Optical Potential	19
	2.4.3 The Folding Model	22
	2.4.4 The Plane Wave Impulse Approximation	26
3.	Experimental	32
	3.1 General	32
	3.2 The Target	36
	3.3 Data Acquisition	37
	3.4 Schematics of The Multwire Drift Chambers (MWC's)	37
	3.5 Focal Plane Calculation	38
	3.6 Quadratic Aberration Correction	38
	3.7 Kinematic Shift Correction	42
	3.8 Particle Identification	42
	3.9 The Drift Chamber Decoding	46
4.	Method of Analysis	54
	4.1 Investigation of The Drift Chamber Efficiencies	54
	4.2 Maximum Number of Adjacent Triggered Wires In The Front-end-chamber	57

4.3 Determination of The Central Ray Location In The Solid angle Defining Front-end-chamber 62

4.4 Determination of Energy Loss In Target 64

4.5 Calculation of The Differential Cross Section ...68

4.6 Results of Data Analysis 73

5. Optical Model Analysis 84

5.1 Non-relativistic Analysis Using The Standard Optical Model Code MAGALI 84

5.2 Techniques of Search 85

5.3 Ambiguity of The Parameters 87

5.4 Results and Conclusions 88

Bibliography 110

References 111

Appendix A 113

Appendix B 124

Appendix 1 131

Appendix 2 133

Appendix 3 137

Appendix 4 141

Appendix 5 144

List of Tables

Table		Page
3.1	Table of TDC channel assigment to the MWC wires.	47
3.2	Table of the *central* 'X' and 'U' TDC# and the corresponding relative channel number.	53
4.1	Table of definition for 'missing' and 'multiple' events in the MWC's	55
4.2	Table of number of events in the {ok,missing,multiple} VDC#2 histogram shown in figure (4.1)	55
4.3	Table of number of events in the {ok,missing,multiple} VDC#1 histogram shown in figure (4.2).	58
4.4	Table of number of events in the {ok,missing,multiple} FEC histogram shown in figure (4.3).	58
4.5	Table of number of events in the {ok,missing,multiple} FEC histrogram for NHIT $\leq$ 1.	63
4.6	Table of number of events in the {ok,missing,multiple} FEC histrogram for NHIT $\leq$ 2.	63
4.7	Table of angular range of data taken in July,1981, April,1982, and June,1984.	79
5.1	Table of one-geometry optical model parameterizations.	89
5.2	Table of optical parameterizations with the geometry parameters in search for minimun χ^2.	92
5.3	Table of volume integrals (MeV-fm^3) of the optical model potentials using the parameters given in table 5.2	93

List of Figures

Figure		Page
1.1	The "wine-bottle-bottom" shape of the real central potential (solid line). The Woods-Saxon shape is shown for comparison (dashed line).	3
2.1	Feynman diagram showing (i) first order term, and (ii) second order term of potential scattering by U.	10
2.2	Diagram showing the spin rotation angle β in relation to the in-coming and out-going wave-vectors.	15
2.3	Feynman diagrams showing i) potential scattering and ii) scattering through "excited states" of the nucleus.	23
3.1	Layout of the TRIUMF beam-line and experimental facilities.	33
3.2	An layout showing beam-line BL4B in TRIUMF.	34
3.3	The focal plane geometry of the MRS.	40
3.4	Diagram of the angle of trajactory, THET, through the VDC's	40
3.5	An SXFX0 spectrum showing vertical bands of constant XFCC.	41
3.6	An SXFY0 spectrum showing vertical bands of constant XFK.	43
3.7	An SXFTH spectrum showing vertical bands of constant XFK.	44
3.8	A particle identification scatter plot (SPID) showing proton and deuteron peaks.	45
3.9	Schematic diagram showing the numbering, and the relative position, of the wires in the FEC.	48
3.10	Schematic diagram showing the 'X' and 'U' wires in a VDC drift chamber.	48
3.11	Diagram showing a particle trajactory through a VDC drift chamber.	51

Figure Page

3.12 Vector diagram showing the calculation of 'Y' from 'X' and 'U' of the VDC's 51

4.1 {ok,missing,multiple} scatter plot of VDC#2. 56

4.2 {ok,missing,multiple} scatter plot of VDC#1. 59

4.3 {ok,missing,multiple} scatter plot of FEC. 60

4.4 Diagram showing the possibility of a single particle track triggering two adjacent wires in the FEC. 61

4.5 Spectrum showing the Y0 angular byte accepted by the spectrometer when the quadrupole is on. 65

4.6 Spectrum showing the Y0 angular byte accepted by the spectrometer when the quadrupole is off. 66

4.7 Graph of ground state to first excited state scattering ratio against Y0. 67

4.8 An SXF spectrum showing a clean oxygen elastic peak. 70

4.9 An SXF spectrum showing the carbon elastic peak close to the oxygen elastic peak. 71

4.10 The differential cross section angular distribution of the 200 MeV 'old' data before re-normalization. 74

4.11 The differential cross section angular distribution of the 300 MeV 'old' data before re-normalization. 75

4.12 The differential cross section angular distribution of the 400 MeV 'old' data before re-normalization. 76

4.13 The differential cross section angular distribution of the 500 MeV 'old' data before re-normalization. 77

Figure Page

4.14 Differential cross section angular distribution of 'new' data at 200 MeV. 80

4.15 Differential cross section angular distribution of 'new' data at 300 MeV. 81

4.16 Differential cross section angular distribution of 'new' data at 400 MeV. 82

4.17 Differential cross section angular distribution of 'new' data at 508 MeV. 83

5.1 Non-relativistic standard optical model fit to the differential cross section angular distribution at 200 MeV using the parametrization (i) in table 5.2. 94

5.2 Non-relativistic standard optical model fit to the analyzing power angular distribution at 200 MeV using the parametrization (i) in table 5.2 95

5.3 Non-relativistic standard optical model fit to the differential cross section angular distribution at 200 MeV using the parametrization (ii) in table 5.2 96

5.4 Non-relativistic standard optical model fit to the analyzing power angular distribution at 200 MeV using the parametrization (ii) in table 5.2 97

5.5 Non-relativistic standard optical model fit to the differential cross section angular distribution at 300 MeV using the parametrization (i) in table 5.2 98

5.6 Non-relativistic standard optical model fit to the analyzing power angular distribution at 300 MeV using the parametrization (i) in table 5.2 99

5.7 Non-relativistic standard optical model fit to the differential cross section angular distribution at 300 MeV using the parametrization (ii) in table 5.2 100

Figure Page

5.8 Non-relativistic standard optical model fit to the analyzing power angular distribution at 300 MeV using the parametrization (ii) in table 5.2 101

5.9 Non-relativistic standard optical model fit to the differential cross section angular distribution at 400 MeV using the parametrization given in table 5.2 102

5.10 Non-relativistic standard optical model fit to the analyzing power angular distribution at 400 MeV using the parametrization given in table 5.2 103

5.11 Non-relativistic standard optical model fit to the differential cross section angular distribution at 500 MeV using the parametrization given in table 5.2 104

5.12 Non-relativistic standard optical model fit to the analyzing power angular distribution at 500 MeV using the parametrization given in table table 5.2 105

5.13 Radial distributions of the real central potentials according to the parameters given in table 5.2. 106

5.14 Radial distributions of the imaginary central potentials according to the parameters given in table 5.2. 107

5.15 Radial distributions of the real spin-orbit potentials according to the parameters given in table 5.2. 108

5.16 Radial distributions of the imaginary spin-orbit potentials according to the parameters given in table 5.2. 109

1. Introduction

According to the optical model, the nucleon-nucleus interaction is represented by a complex central potential and a complex spin-orbit potential. The spin-orbit piece is introduced to explain polarization phenomena. Phenomenologically, one can parameterize the optical potential as

$$U_{op} = V_{coul} + V_c F_c + iW_c F_{ic} + (\hbar/m_\pi c)^2 \left[V_{so} \frac{1}{r}\frac{d}{dr} F_{so} + iW_{so} \frac{1}{r}\frac{d}{dr} F_{iso}\right] \underline{\sigma}\cdot\underline{l}. \qquad (1.1)$$

V_{coul} denotes the Coulomb interaction. V_x and W_x denote the real and imaginary potential depths, respectively, while F_x is a radial function giving a shape to the associated potential. The subscripts 'c', 'i', and 'so' denote central, imaginary, and spin-orbit, respectively.

Elementary calculations have shown that F_x has the same shape as the nuclear density distribution. (See section 2.4.3.) Various forms for this function have been introduced (HOD 63), some of them are for the purpose of computational convenience, the commom forms used to date pertain to the Woods-Saxon function which has been successful in fitting differential cross section and polarization data for proton scattering up to 200 MeV.

At higher energies, relativistic treatment of the nucleon-nucleus interaction and reduction to Schrödinger form shows that at intermediate energies the central potential has reduced strength near the nuclear surface

region. At the transition energy region (about 300 MeV) where the central potential changes from attractive to repulsive, the pocket of attraction near the nuclear surface is so pronounced that the radial distribution of the potential resembles a "wine-bottle-bottom" shape as shown in figure (1.1). Recent experimental results (Glo 85, Arn 81) are in favour of this prediction. Indeed, more sophisticated calculations using either non-relativistic (Bri 77) or relativistic (Jam 74) approach also predict such features.

Proton scattering experiments at intermediate energies have been done at TRIUMF with Pb-208 and Ca-40 targets. The present experiment extends the existing data to a light nucleus.

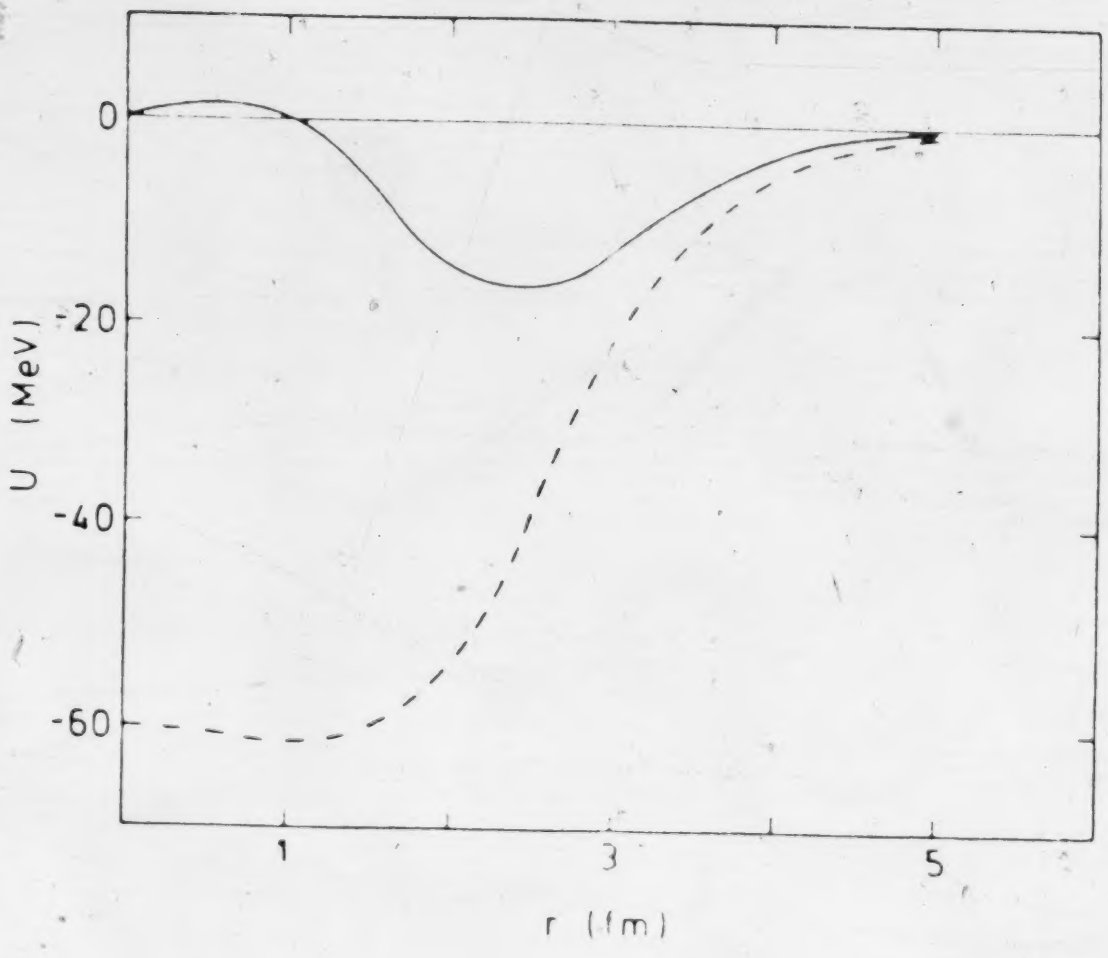

Figure 1.1 The "wine-bottle-bottom" shape of the real central potential (solid line). The Woods-Saxon shape is shown for comparison (dashed line).

2. Theory

2.1 Scattering Theory

We start by giving a brief summary of the scattering theory that we shall use. Consider a nuclear potential, U, the time-independent Schrödinger equation for nucleon-nucleus scattering can be written as

$$[E - H_o - U] \, |\psi\rangle = 0 \tag{2.1}$$

where H_o is the kinetic energy operator. Expanding $|\psi\rangle$ in terms of a complete set of plane wavefunctions $|\Phi_k\rangle$ which satisfy

$$(E_k - H_o) \, |\Phi_k\rangle = 0 \tag{2.2}$$

gives

$$|\psi\rangle = \sum_k |\Phi_k\rangle\langle\Phi_k|\psi\rangle = \sum_k a_k |\Phi_k\rangle \tag{2.3}$$

where the summation over k is to be replaced by integration over k for continuous k.

The Schrödinger equation can now be written as

$$\sum_k (E - H_o) \, a_k |\Phi_k\rangle = U |\psi\rangle \tag{2.4}$$

or

$$\sum_k (E - E_k) \, a_k |\Phi_k\rangle = U |\psi\rangle \, . \tag{2.5}$$

Multiply on the left by $\langle\Phi_{k'}|$,

$$\sum_k (E - E_k)\, a_k \langle \Phi_{k'} | \Phi_k \rangle = \langle \Phi_{k'} | U | \psi \rangle \ , \tag{2.6}$$

and making use of

$$\langle \Phi_{k'} | \Phi_k \rangle = (2\pi)^3 \, \delta(\mathbf{k}-\mathbf{k}') \ , \tag{2.7}$$

we have

$$(2\pi)^3 \, (E - E_{k'})\, a_{k'} = \langle \Phi_{k'} | U | \psi \rangle \ . \tag{2.8}$$

The general solution for $|\psi\rangle$ is therefore

$$|\psi\rangle = |\Phi\rangle + G_o U |\psi\rangle \tag{2.9}$$

where

$$G_o = \sum_k (2\pi)^{-3} \, (E - E_k)^{-1} \, |\Phi_k\rangle\langle\Phi_k| \ . \tag{2.10}$$

Equation (2.9) is the well known Lipmann-Schwinger equation.

In coordinate space representation, writing

$$\langle r | \psi \rangle = \psi(\mathbf{k},\mathbf{r}), \tag{2.11}$$

we have

$$(2\pi)^3 \, (E - E_{k'})\, a_{k'} = \int d\mathbf{r}' \, \Phi^*(\mathbf{k}',\mathbf{r}') \, U(\mathbf{r}') \, \psi(\mathbf{k}',\mathbf{r}') \ . \tag{2.12}$$

Substituting $a_{k'}$ from the last equation into eqn.(2.3) yields,

$$\psi(\mathbf{k},\mathbf{r}) = \sum_{k'} a_{k'} \, \Phi(\mathbf{k}',\mathbf{r}) = \int d\mathbf{r}' \, G_o(\mathbf{r},\mathbf{r}') \, U(\mathbf{r}') \psi(\mathbf{k},\mathbf{r}') \tag{2.13}$$

where

$$G_0(\mathbf{r},\mathbf{r}') = (2\pi)^{-3} \sum_{\mathbf{k}'} (E - E_{\mathbf{k}'})^{-1} \Phi^*(\mathbf{k}'\mathbf{r}')\Phi(\mathbf{k}',\mathbf{r}) , \tag{2.14}$$

the poles of which are to be handled by the boundary conditions.

Thus, the general solution for ψ in coordinate space can be written as

$$\psi(\mathbf{k},\mathbf{r}) = \Phi(\mathbf{k},\mathbf{r}) + \int d\mathbf{r}' \; G_0(\mathbf{r},\mathbf{r}') \; U(\mathbf{r}') \; \psi(\mathbf{k},\mathbf{r}') . \tag{2.15}$$

Inserting the explicit plane wavefunctions

$$\Phi(\mathbf{k},\mathbf{r}) = e^{i\mathbf{k}\cdot\mathbf{r}} \tag{2.16}$$

and converting the sum into integration over $\mathbf{k}$, the Green's function $G_0(\mathbf{r},\mathbf{r}')$ can be written as

$$\begin{aligned} G_0^{\pm}(\mathbf{r},\mathbf{r}') &= \lim_{\epsilon \to 0} (2\pi)^{-3} \int \exp[i\mathbf{k}'\cdot(\mathbf{r}-\mathbf{r}')] \\ &\qquad (k^2 - k'^2 \pm i\epsilon)^{-1} \, (2\mu/\hbar^2) \, d\mathbf{k}' \\ &= -(\mu/2\pi\hbar^2) \, e^{\pm ik|\mathbf{r}-\mathbf{r}'|} / |\mathbf{r}-\mathbf{r}'| \end{aligned} \tag{2.17}$$

where $\pm$ denotes the boundary conditions; '+' for an outgoing spherical wave and '-' for an incoming spherical wave. These Green's functions are known as the 'retarded' and 'advanced' Green's functions, respectively.

The nomenclature can be understood by considering the following. Since the nuclear potential is only of finite range, then in the asymptotic region where r is very much greater than r' which contributes to the integrand, the

asymptotic wavefunctions obtained from eqn.(2.15), eqn.(2.16) and eqn.(2.17) can be written as

$$\psi^{\pm}(\mathbf{k},\mathbf{r}) \to e^{i\mathbf{k}\cdot\mathbf{r}} - (\mu/2\pi\hbar^2)\int d\mathbf{r}' \frac{1}{r} e^{\pm ik(r-\hat{\mathbf{r}}\cdot\mathbf{r}')} U(\mathbf{r}')\psi^{\pm}(\mathbf{k},\mathbf{r}')$$

$$= e^{i\mathbf{k}\cdot\mathbf{r}} - (\mu/2\pi\hbar^2)\frac{1}{r} e^{\pm ikr}\int d\mathbf{r}' e^{\mp i\mathbf{k}\cdot\mathbf{r}'} U(\mathbf{r}')\psi^{\pm}(\mathbf{k},\mathbf{r}')$$

$$U(\mathbf{r}')\,\psi^{\pm}(\mathbf{k},\mathbf{r}') \qquad (2.18)$$

where we have written

$$\mathbf{k}' = k\hat{\mathbf{r}} \ , \qquad (2.19)$$

that is , $\mathbf{k}'$ has magnitude k and direction in which the scattering amplitude is measured.

The time evolution of $\psi^{\pm}$ therefore follows $e^{\mp iEt/\hbar}$, thus ψ^{+} propagates forwards in time while ψ^{-} propagates backwards in time; hence the names 'retarded' and 'advanced' wavefunctions.

If we define the scattering amplitude, $f(\theta,\phi)$, by the asymptotic form of the wavefunction

$$\psi^{+} \to e^{i\mathbf{k}\cdot\mathbf{r}} + f(\theta,\phi)\frac{1}{r} e^{i\mathbf{k}\cdot\mathbf{r}} \qquad (2.20)$$

, by comparison with eqn.(2.18), we obtain the expression for the scattering amplitude

$$f(\theta,\phi) = -(\mu/2\pi\hbar^2)\int e^{-i\mathbf{k}'\cdot\mathbf{r}'} U(\mathbf{r}')\,\psi^{+}(\mathbf{k},\mathbf{r}')\,d\mathbf{r}' \ . \qquad (2.21)$$

Formally, $G_o^{\pm}$ can be written as

$$G_o^{\pm} = (E - H_o \pm i\epsilon)^{-1} \ . \qquad (2.22)$$

If we define the operators $G^{\pm}$ corresponding to the total Hamiltonian

$$H = H_0 + U \tag{2.23}$$

as

$$G^{\pm} = (E - H \pm i\epsilon)^{-1} , \tag{2.24}$$

then by

$$\frac{1}{A} - \frac{1}{B} = \frac{1}{B}(B - A)\frac{1}{A} , \tag{2.25}$$

we obtain

$$G_0^{\pm} = G^{\pm} + G^{\pm} U G_0^{\pm} . \tag{2.26}$$

Substituting into the Lipmann-Schwinger equation yields

$$\begin{aligned} |\psi^{\pm}\rangle &= |\Phi\rangle + G^{\pm} U [|\psi^{\pm}\rangle - G_0 U|\psi^{\pm}\rangle] \\ &= |\Phi\rangle + G^{\pm} U|\Phi\rangle \end{aligned} \tag{2.27}$$

or

$$|\psi^{\pm}\rangle = [1 + G^{\pm} U]|\Phi\rangle = \Omega^{\pm}|\Phi\rangle \tag{2.28}$$

where Ω is the Møller wave operator that takes initial plane wave states into scattered states.

Using

$$G^{\pm} = G_0^{\pm} + G_0^{\pm} U G^{\pm} , \tag{2.29}$$

one can write

$$\psi^{\pm}(k,r) = \Phi(k,r) + \int G_o^{\pm}(r,r')\, U(r)\, \Phi(k,r')\, dr'$$

$$+ \int\int G_o^{\pm}(r,r")\, U(r")\, G_o^{\pm}(r",r')\, U(r')\, \Phi(k,r')\, dr'dr"$$

$$+ \cdots\cdots . \qquad (2.30)$$

Each of these terms can be represented by a Feynman diagram (FEY 49) as shown in figure (2.1), where the second term on the right hand side of eqn.(2.30) is represented by (i), the third term by (ii), etc.

Defining the transition operator $T^{\pm}$ as

$$T^{\pm} = U\Omega^{\pm}$$

$$= U + UG^{\pm}U$$

$$= U + UG_oT^{\pm}\,, \qquad (2.31)$$

the transition matrix element, T_{fi}, between the initial state, i, and the final state, f, is given by

$$T_{fi} = \langle\Phi_f|T^{+}|\Phi_i\rangle$$

$$= \langle\Phi_f|U\Omega^{\pm}|\Phi_i\rangle$$

$$= \langle\Phi_f|U|\psi^{\pm}_i\rangle\,. \qquad (2.32)$$

By comparison with eqn.(2.21), one obtains the relation between the scattering amplitude and the transition matrix element, thus

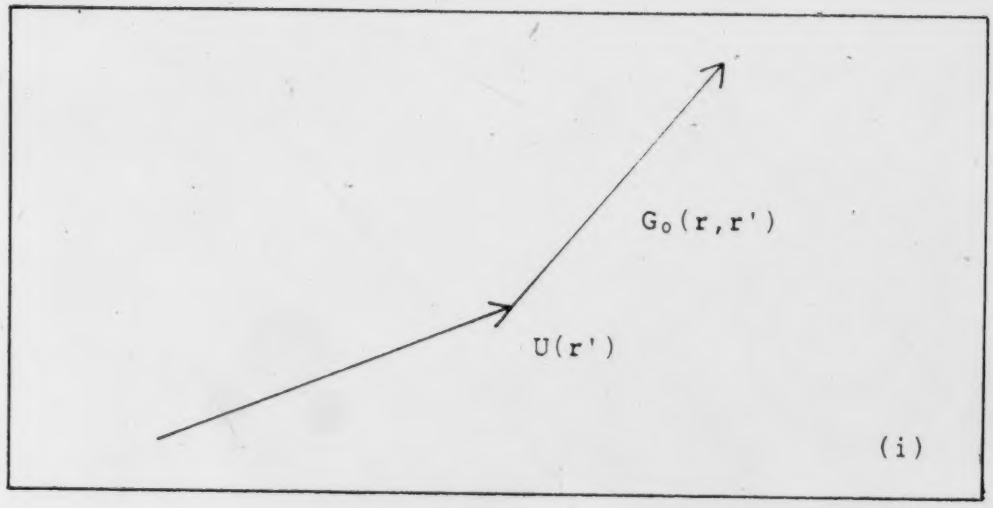

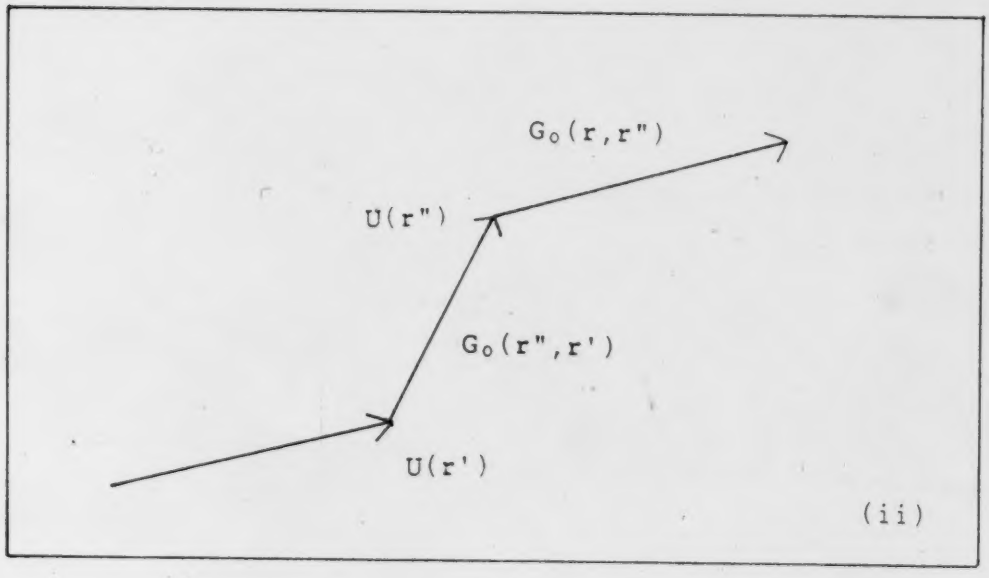

Figure 2.1 Feynman diagram showing (i) first order term, and (ii) second order term of potential scattering by U.

$$f(\theta,\phi) = -(\mu/2\pi\hbar^2)\, T_{fi} \quad . \tag{2.33}$$

2.2 Phase Shift Calculation

Recall the expression for the total wavefunction obtainable by partial wave analysis

$$\psi = \sum_{jlm} \frac{1}{r} u_{jl}(r)\, C^{jls}_{m\lambda\mu}\, i^{l}\, Y^{\lambda}_{l}(\theta\phi)\, \chi^{\mu}_{s} \tag{2.34}$$

where $C^{jls}_{m\lambda\mu}$ is a Clebsch-Gordan coeffecient which couples the orbital angular momentum, l, to the spin, s, of the projectile. u_{jl} is a radial wavefunction, Y^{λ}_{l} a spherical harmonic function and χ^{μ}_{s} a spin wavefunction.

Inserting ψ into the Schrödinger equation one obtains the radial equation for u_{jl}

$$\left[\frac{d^2}{dr^2} + k^2 - \frac{1}{r^2}\, l(l+1) - V_{coul} + V\right] u_{jl}(kr) = 0 \tag{2.35}$$

where we have seperated the Coulomb interaction V_{coul} from the nuclear potential, V

$$U = V_{coul} + V \quad . \tag{2.36}$$

Equation (2.35) can be numerically integrated for each angular momentum l to determine u_{jl}. The solutions u_{jl} and their derivatives are matched to that of the asymptotic wavefunction to obtain the phase shifts δ_l.

The asymptotic form of $u_{jl}(kr)$ can be written as

$$u_{jl}(kr) \to \frac{1}{2} kr \left[H_l^{(2)}(kr) + \exp(2i\delta_l) H_l^{(1)}(kr)\right] \tag{2.37}$$

where $H_l^{(1)}$ and $H_l^{(2)}$ denote the solutions to the radial equation without the nuclear potential V. For neutrons, the Coulomb term vanishes so that $H_l^{(1)}$ and $H_l^{(2)}$ are just the spherical Hankel functions

$$H_l^{(1)} = h_l^{(1)} = j_l + i\eta_l \tag{2.38}$$

$$H_l^{(2)} = h_l^{(2)} = j_l - i\eta_l . \tag{2.39}$$

For protons, the Bessel functions j_l and η_l are replaced by the regular and irregular Coulomb functions, F_l and G_l.

The scattering amplitude can be determined from the phase shifts by the relation

$$f(\theta) = (2ik)^{-1} \sum_l (2l+1) [\exp(2i\delta_l)-1] P_l(\cos\theta) \tag{2.40}$$

whereby observables can be calculated.

2.3 Elastic Scattering of Spin-1/2 Particles From Spin-zero Targets

Recall that for spinless particles scattered from a spinless target, the asymptotic wave function ψ is given by

$$\psi \to e^{ikz} + f(\theta,\phi) \frac{1}{r} e^{ikr} \tag{2.41}$$

where θ and ϕ are the spherical coordinates.

Similarly, for the scattering of spin-1/2 particles, one has

$$\psi_{s,\mu} \rightarrow \chi^{\mu}_{s} e^{ikz} + \sum_{\nu} \chi^{\nu}_{s} f_{\nu\mu}(\theta,\phi) \frac{1}{r} e^{ikr} \tag{2.42}$$

where χ^{μ}_{s} denotes the spin wavefunction with spin s and projection μ. One may write

$$\mathbf{M}\chi^{\mu}_{s} = \sum_{\nu} f_{\nu\mu} \chi^{\nu}_{s} \tag{2.43}$$

where **M** is the scattering operator so that

$$\psi_{s,\mu} \rightarrow [e^{ikz} + \frac{1}{r} e^{ikr} \mathbf{M}]\chi^{\mu}_{s} . \tag{2.44}$$

For spin-1/2 projectile and spin zero target, **M** is a 2x2 matrix the most general form of which is given by [1]

$$\mathbf{M} = f(\theta)1 + g(\theta)\, \underline{\sigma}\cdot\hat{n} \tag{2.45}$$

where $\hat{n}$ is an axial vector defined by

$$\hat{n} = (\mathbf{k}_i \times \mathbf{k}_f) / |\mathbf{k}_i \times \mathbf{k}_f| \tag{2.46}$$

with $\mathbf{k}_i$ and $\mathbf{k}_f$ the initial and final wave vectors, respectively.

The differential cross section is then given by

$$\frac{d\sigma}{d\Omega} = 1/2\ \mathrm{tr}(\mathbf{M}^{\dagger}\mathbf{M}) = |f|^2 + |g|^2 \tag{2.47}$$

where the factor one-half comes from averaging over the initial spin states.

The polarization, P, is given by

$$P = \langle\sigma_n\rangle = (\mathrm{tr}\mathbf{M}^{\dagger}\mathbf{M}\sigma_n)/(\mathrm{tr}\mathbf{M}^{\dagger}\mathbf{M}) = 2\,\mathrm{Re}(f g^{*})/(|f|^2 + |g|^2) \tag{2.48}$$

---

[1] *The three Pauli spin matrices together with the unit matrix form a basis of all 2x2 matrices.*

and the analyzing power A_y is equal to P for elastic scattering assuming time-reversal-invariance.

The fact that $f(\theta)$ and $g(\theta)$ are complex quantities implies that there are four real numbers involved, one of which is an overall phase factor. This gives rise to three independent observables. A candidate for the third independent observable has been defined by Glauber and Osland (Gla 79) as

$$Q(q) = 2\,\mathrm{Im}(f\,g^{*})/(|f|^{2} + |g|^{2}) \quad . \tag{2.49}$$

Now $|P| \leq 1$, $|Q| \leq 1$, and $P^{2}+Q^{2} \leq 1$ so that Q(q) can be expressed in terms of an angle β such that

$$Q(q) = \sqrt{[1 - P^{2}(q)]}\,\mathrm{Sin}(\beta) \tag{2.50}$$

The angle β, known as the spin rotation angle, corresponds to the angle by which the projection of the spin in the scattering plane rotates (figure 2.2). In this context, β is the third observable which can be experimentally measured. In practice, however, one measures the Wolfenstein asymmetry parameter, A, and rotation parameter, R, which are related to Q by

$$Q_{lab} = A\,\mathrm{Cos}(\theta_{lab}) + R\,(\theta_{lab}) \quad . \tag{2.51}$$

Recently it has been shown (Glo 85, Sch 83) that all three independent observables seem to be needed to define the optical model parameters unambigiously.

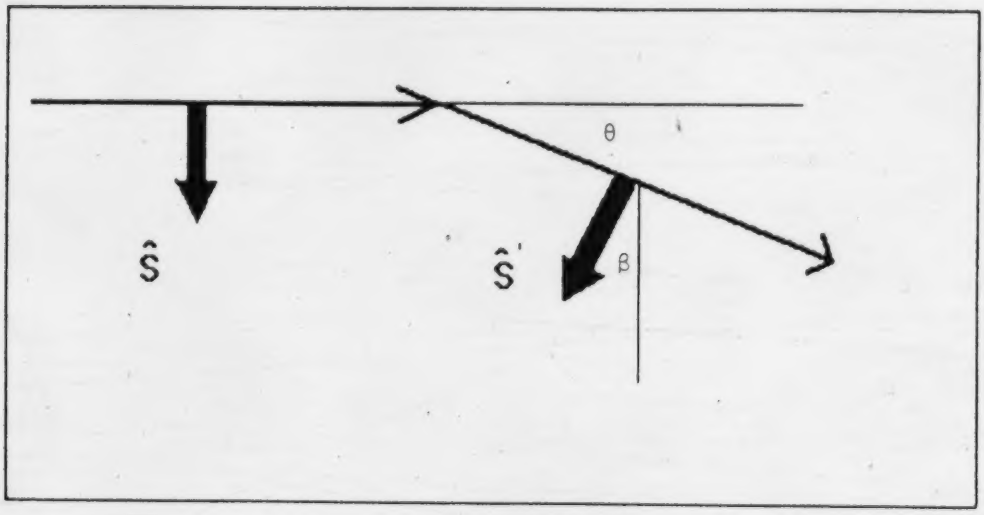

Figure 2.2 Diagram showing the spin rotation angle β in relation to the in-coming and out-going wave-vectors.

2.4 The Optical Model

2.4.1 The Phenomenological Optical Model

Let us consider the scattering of nucleons by a nucleus. In the non relativistic treatment of quantum mechanics, the time-evolution of the system is governed by the Schrödinger equation. The fact that the nucleus is composed of particles implies that even at the level of uniform nuclear matter (where we can ignore boundary effects of the finite size nucleus), the interaction is so complicated that an exact solution is formidable, if not impossible.

On the other hand, since the energy resolution in an actual experiment has a spread which is large compared to the spacings between "resonances" of the detailed interaction, the latter will be smoothed out by averaging so that it is conceivable that an effective potential of the actual interaction would suffice under most circumstances.

A basic requirment of a successfull model of the effective interaction should take care of both "absorptions" as well as elastic (or propagation) channels. Let us consider a complex potential of the form

$$M = -V - iW. \tag{2.52}$$

It follows that the momentum, k, of a nucleon with energy E is complex :

$$k = \sqrt{\{2m(E+V+iW)\}} \simeq \sqrt{\{2m(E+V)\}} + imW/\sqrt{\{2m(E+V\}} = k' + ik'' \tag{2.53}$$

to first order, where

$$k' \equiv \sqrt{\{2m(E+V)\}} \equiv mv' \tag{2.54}$$

and

$$k'' \equiv W/v' \ . \tag{2.55}$$

Hence,

$$e^{ikz} = e^{ik'z} \cdot e^{-k''z} \tag{2.56}$$

Clearly, the imaginary part of the potential gives rise to an attenuation of the wavefunction corresponding to a mean free path

$$L \simeq v'/2W \ . \tag{2.57}$$

Thus, the imaginary part of the potential takes care of all non-"shape elastic" channels (absorptions), hence the name optical potential in analogy to refraction and absorption of electromagnetic waves in a medium.

Experimentally one finds that scattered particles are polarized. This indicates that a spin dependent term must be present in the effective potential, the simplest form of which is a spin-orbit interaction. Phenomenologically one writes the standard optical model potential, U_{op} as

$$U_{op} = V_{coul} + V_c F_c + i(W_c - 4W_D \frac{d}{dr})F_{ic} + (\hbar/m_\pi c)^2[V_{so}\frac{1}{r}\frac{d}{dr}F_{so} + W_{so}\frac{1}{r}\frac{d}{dr}F_{iso}]\,\underline{\sigma}\cdot\mathbf{l} \quad (2.58)$$

where $\mathbf{l}$ and $\underline{\sigma}$ are the orbital and spin angular momenta of the projectile, respectively.

$$F_x(r) = \{1 + \exp[(r-R_x)/a_x]\}^{-1} \quad (2.59)$$

are the Woods-Saxon functions (two-parameter fermi form factors) with

$$R_x = r_x A^{1/3} \quad (2.60)$$

giving an explicit mass dependence on the optical potential.

V_{coul} is the Coulomb interaction between the projectile with charge $Z_i e$ and a nucleus with charge $Z_0 e$. In most cases it is adequate to treat the nucleus as a uniformly charged sphere of radius R_0 so that

$$V_{coul} = (Z_0 Z_i e^2)/(2R_0)(3 - r^2/R_0^2)\ ,\ r < R_0$$
$$= (Z_0 Z_i e^2)/r\ ,\ r \geq R_0\ . \quad (2.61)$$

The central imaginary potential contains two terms: a volume term, W_c and a surface term, W_D, corresponding to volume and surface absorption, respectively. Surface absorption is only important at energies below 50 MeV when Pauli blocking is appreciable inside the nucleus. For higher energies, volume absorption is dominant. Generally, it is not necessary to use both terms to obtain a good χ^2 fit. In

our case, W_D is fixed at zero.

2.4.2 Formal Theory of The Optical Potential

We now show how the form given to the *phenomenological* optical potential can be justified from a *microscopic* point of view. We first follow Feshbach (Fes 58) to give a formal "unified theory" of the optical potential.

From a non-relativistic point of view, one has to solve the Schrödinger equation

$$(E - H)\psi = 0 \tag{2.62}$$

pertaining to the problem at hand. For scattering of a nucleon by a nucleus, the full Hamiltonian H can be separated as

$$H = H_0 + V + H(\xi) \tag{2.63}$$

where H_0 is the kinetic energy operator for the incident nucleon, V is the interaction potential and $H(\xi)$ is the internal Hamiltonian of the target nucleus as a function of all internal coordinates ξ.

One may expand the total wavefunction ψ in terms of a complete set of eigenfunctions of the nuclear states $\Phi_\alpha(\xi)$ such that

$$\psi = \sum_\alpha \psi_\alpha \Phi_\alpha$$

$$H(\xi)\,\Phi_\alpha(\xi) = \epsilon_\alpha \Phi_\alpha(\xi)\ . \tag{2.64}$$

For incident nucleons indistinguishable from the target nucleons the total wavefunction must be antisymmetrized. For simplicity we will assume the incident nucleon as distinguishable. Equivalently, the following is a good approximation if exchange effects can be ignored.

If we are only interested in elastic scattering, we would like to project the elastic channel out of the total wavefunction. We define the projection operators **P** and **Q** by

$$\mathbf{P}\,\psi = \psi_o\Phi_o \tag{2.65}$$

$$\mathbf{Q}\,\psi = (1 - \mathbf{P})\psi \tag{2.66}$$

where $\psi_o\Phi_o$ is the 'elastic' projection of ψ.

Since the Φ_α form a complete set of states, it is easy to see that **P** can be written as

$$\mathbf{P} = |\Phi_o\rangle\langle\Phi_o| \ . \tag{2.67}$$

Now multiplying the Schrödinger equation

$$(E - \mathbf{H})(\mathbf{P} + \mathbf{Q})\psi = 0 \tag{2.68}$$

on the right by **P** ,and **Q**, give

$$(E - \mathbf{PHP})\mathbf{P}\psi = (\mathbf{PHQ})\mathbf{Q}\psi \tag{2.69}$$

and

$$(E - \mathbf{QHQ})\mathbf{Q}\psi = (\mathbf{QHP})\mathbf{P}\psi \tag{2.70}$$

,respectively. Rearranging the second of these and substituting into the first yields

$$[E - PHP - PHQ\,(E - QHQ)^{-1}\,QHP]\,P\psi = 0 \quad . \tag{2.71}$$

Putting $P = |\Phi_o\rangle\langle\Phi_o|$, we have

$$PHP = |\Phi_o\rangle\langle\Phi_o|\,H\,|\Phi_o\rangle\langle\Phi_o|$$

$$= |\Phi_o\rangle[H_o + \langle\Phi_o|V|\Phi_o\rangle]\langle\Phi_o| \tag{2.72}$$

where we have assumed that the energy eigenvalue of the ground state $\Phi_o(\xi)$ is zero.

On the other hand,

$$PHQ = P\,[H_o + V + H(\xi)]\,Q$$

$$= E_o PQ + PVQ + \epsilon PQ$$

$$= |\Phi_o\rangle\langle\Phi_o|VQ \tag{2.73}$$

since $PQ\psi = QP\psi = 0$.

Similarly,

$$QHP = QV|\Phi_o\rangle\langle\Phi_o| \quad . \tag{2.74}$$

Hence,

$$\{E - |\Phi\rangle[H_o + \langle\Phi_o|V|\Phi_o\rangle]\langle\Phi_o|$$

$$- |\Phi_o\rangle\langle\Phi_o|VQ(E-QHQ)^{-1}QV|\Phi_o\rangle\langle\Phi_o|\}|\Phi_o\rangle\langle\Phi_o|\psi = 0 \quad . \tag{2.75}$$

Multiplying on the left by $\langle\Phi_o|$, one obtains,

$$[E - H_o - \langle\Phi_o|V|\Phi_o\rangle - \langle\Phi_o|VQ(E-QHQ)^{-1}QV|\Phi_o\rangle]\,\psi_o = 0 \tag{2.76}$$

where

$$\psi_o = \langle\Phi_o|\psi\rangle \tag{2.77}$$

Thus, formally we can write the optical potential U_{op} as

$$U_{op} = \langle\Phi_o|V|\Phi_o\rangle + \langle\Phi_o|VQ(E-QHQ)^{-1}QV|\Phi_o\rangle \ . \tag{2.78}$$

Qualitively, the above expression represents: 1) direct scattering by the interaction potential V, and 2) scattering which proceeds through "excited states" of the nucleus. These are represented in terms of Feynman diagrams in (figure 2.3).

2.4.3 The Folding Model

If we assume that scattering through 'excited states' of the nucleus is negligible, then

$$U_{op} = \langle\Phi_o|V|\Phi_o\rangle \ . \tag{2.79}$$

Now we follow Greenlees et al (Gre 68) and write the interaction potential V as

$$V = \sum_i^A v(r,r_i) \ . \tag{2.80}$$

The general from of the nucleon-nucleon interaction $v(r,r_i)$ can be written

$$v(r,r_i) = v_d(|r-r_i|) + v_\tau(|r-r_i|)\underline{\tau}\cdot\underline{\tau}_i + v_\sigma(|r-r_i|)\underline{\sigma}\cdot\underline{\sigma}_i +$$
$$v_{\sigma\tau}(|r-r_i|)\underline{\sigma}\cdot\underline{\sigma}_i\,\underline{\tau}\cdot\underline{\tau}_i + [v_t(|r-r_i|) +$$
$$v_{t\tau}(|r-r_i|)\underline{\tau}\cdot\underline{\tau}_i]\,S_{12} + v_{ls}\frac{1}{\hbar}[(r-r_i)x(p-p_i)\cdot(\underline{\sigma}+\underline{\sigma}_i)]$$

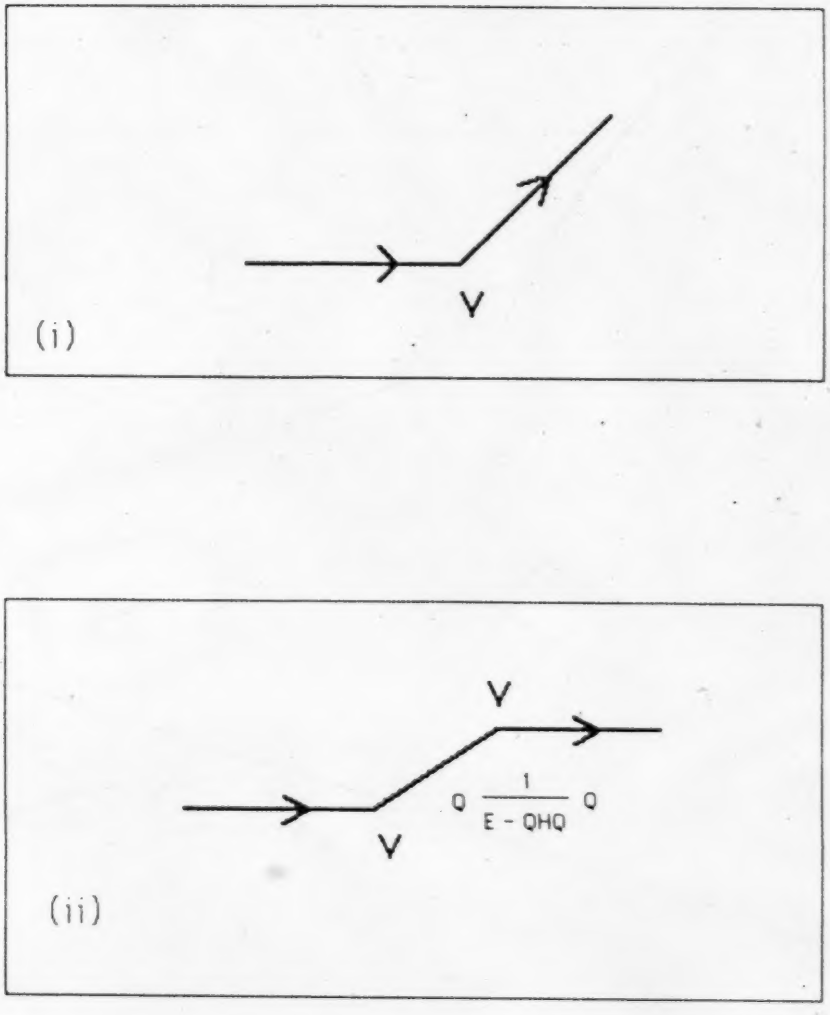

Figure 2.3 Feynman diagrams showing i) potential scattering and ii) scattering through "excited states" of the nucleus.

(2.81)

where τ and σ denote isospin and spin, respectively, and $S_{1,2}$ is the tensor operator.

For targets with zero total angular momentum, we have

$$U_{op} = U_d + U_s + U_{so} \tag{2.82}$$

with

$$U_d = \langle\Phi_o| \sum_i^A v_d(|r-r_i|) |\Phi_o\rangle \tag{2.83}$$

$$U_s = \langle\Phi_o| \sum_i^A v_\tau(|r-r_i|) \underline{\tau}\cdot\underline{\tau}_i |\Phi_o\rangle \tag{2.84}$$

$$U_{so} = \langle\Phi_o| \sum_i^A v_{ls}(|r-r_i|) \frac{1}{\hbar}(r-r_i)\times(p-p_i)\cdot(\underline{\sigma}+\underline{\sigma}_i) |\Phi_o\rangle \tag{2.85}$$

Now,

$$\begin{aligned} U_d &= \langle\Phi_o| \sum_i^A v_d(|r-r_i|) |\Phi_o\rangle \\ &= \int dr' \langle\Phi_o| \sum_i^A v_d(|r-r'|) \delta(r-r') |\Phi_o\rangle \\ &= \int dr' v_d(|r-r'|) \langle\Phi_o| \sum_i^A \delta(r-r') |\Phi_o\rangle \\ &= \int dr' v_d(|r-r'|) \rho_m(r') \end{aligned} \tag{2.86}$$

where

$$\rho_m(r') = A\,\rho(r') = \langle\Phi_o| \sum_i^A \delta(r-r') |\Phi_o\rangle\ , \tag{2.87}$$

$\rho_m(r')$ is the nucleon density.

Similarly, writing

$$\tau_{iz} = (1/2)[(1+\tau_{iz})-(1-\tau_{iz})], \tag{2.88}$$

one gets

$$U_s = \tau_z \int dr' \, \rho_n(r') - \rho_p(r') \, v_c(|r-r'|)$$

$$= (N-Z)/A \, \tau_z \int dr' \, v_\tau(|r-r'|) \, \rho_m(r') \, . \qquad (2.89)$$

Thus, for N=Z targets, U_s vanishes.

Finally,

$$U_{so} = \frac{1}{\hbar} \langle \Phi_o | \sum_i^A v_{ls}(|r-r_i|) \, (r-r_i) x (p-p_i) \cdot (\underline{\sigma}+\underline{\sigma}_i) \, | \Phi_o \rangle$$

$$= \frac{1}{\hbar} \int dr' \, v_{ls}(|r-r'|) \, (r-r') x \langle \Phi_o | \sum_i^A \delta(r-r') \, (p-p_i) \cdot (\underline{\sigma}+\underline{\sigma}_i) \, | \Phi_o \rangle$$

$$= \frac{1}{\hbar} \int dr' \, v_{ls}(|r-r'|) \, (r-r') \, x \, \langle \Phi_o | \sum_i^A \delta(r-r') \, | \Phi_o \rangle \, p \cdot \underline{\sigma}$$

$$= \frac{1}{\hbar} \int dr' \, v_{ls}(|r-r'|) \, (r-r') x \rho_m(r') \, p \cdot \underline{\sigma}$$

$$= \frac{1}{\hbar} \int dr' \, v_{ls}(|r-r'|) \, \rho_m(r') \, (1 - \frac{r}{r^2} \cdot r') \, r x p \cdot \underline{\sigma} \qquad (2.90)$$

Expanding $(1 - \frac{r}{r^2} \cdot r')$ about $r-r' = 0$ and keeping only the first non-vanishing term, one has

$$U_{so} \simeq [-\frac{1}{2\hbar} \frac{1}{r dr} \frac{d}{dr} \rho_m r' \, (4\pi/3) \int_0^\infty \eta^4 \, v_{ls}(\eta) \, d\eta] \, \underline{\sigma} \cdot l \qquad (2.91)$$

where η is a dummy variable integrated over all positive values.

Thus, we see that the central term U_d is obtained by 'folding' with the nuclear density distribution whereas the spin-orbit term U_{so} is obtained by 'folding' with the derivative of the nucleon density distribution. If one

assumes the Woods-Saxon function for the nucleon density distribution, one can parametrize the phenomenological optical potential as given by eqn.(2.58).

2.4.4 The Plane Wave Impulse Approximation

At higher energies the approximation made in eqn.(2.79) might not be justified. We present here the plane wave impulse approximation which is more appropriate at intermediate to high energies.

As before, we seperate the full Hamiltonian **H** as

$$\mathbf{H} = \mathbf{H}_0 + \mathbf{V} + \mathbf{H}(\xi) \tag{2.92}$$

so that G^+ can be be written as

$$G^+ = [E - \mathbf{H}_0 - \mathbf{V} - \mathbf{H}(\xi) + i\epsilon]^{-1} . \tag{2.93}$$

We can define a transition operator t(j) which describes the scattering of the projectile by the j-th nucleon in the target nucleus, thus

$$t(j) = V(j) + V(j)\, G_0\, t(j) \tag{2.94}$$

where V(j) is the nuclear potential due to nucleon j.

At energies above 100 MeV the kinetic energy of the projectile is considerabely greater than the binding energy of the target nucleons. Moveover, the lifetime of the compound states is of the same order as the transit time. Consequently, we can consider the projectile interacts with only one nucleon at a time. In this case, the transition

operator t(j) can be replaced by the free-scattering two-nucleon transition operator $\tau(j)$,

$$\tau(j) = V(j) + V(j)\, G_I\, \tau(j) \tag{2.95}$$

where

$$G_I = [E - H_o + i\epsilon]^{-1} . \tag{2.96}$$

Thus, for elastic scattering in the impulse approximation, the transition matrix element becomes

$$T_{fi} = \langle \psi_o \Phi_o |\, \Sigma_j\, \tau(j)\, | \psi_o \Phi_o \rangle_i \tag{2.97}$$

where we have substituted

$$T = \Sigma_j\, \tau(j) \tag{2.98}$$

for the transition operator.

With $\mathbf{k}$ and $\mathbf{k}'$ the initial and final momenta of the projectile, $\mathbf{k}_j$ and $\mathbf{k}'_j$ the initial and final momenta of the j-th nucleon, then, working in momentum space and invoking conservation of momentum, the transition matrix element is given by

$$T_{fi}(\mathbf{k}';\mathbf{k}) = \langle \Phi_o |\, \Sigma_j \int d\mathbf{k}_j\, d\mathbf{k}'_j\, \delta(\mathbf{k} + \mathbf{k}_j - \mathbf{k}' - \mathbf{k}'_j) \int d\mathbf{r}_j\, d\mathbf{r}'_j\, \exp(i\mathbf{k}'_j \cdot \mathbf{r}'_j)\, \langle \mathbf{k}', \mathbf{k}'_j |\, \tau(j)\, | \mathbf{k}, \mathbf{k}_j \rangle \exp(-i\mathbf{k}_j \cdot \mathbf{r}_j)\, | \Phi_o \rangle . \tag{2.99}$$

Integrating over the δ-function and putting the momentum transfer

$$\mathbf{q} = \mathbf{k} - \mathbf{k}', \tag{2.100}$$

gives

$$T_{fi}(\mathbf{k}',\mathbf{k}) = \langle\Phi_o| \sum_j \int d\mathbf{k}_j \iint d\mathbf{r}_j\, d\mathbf{r}'_j \exp[-i\mathbf{k}_j\cdot(\mathbf{r}_j-\mathbf{r}'_j)]$$
$$\exp[i(\mathbf{k}-\mathbf{k}')\cdot\mathbf{r}'_j]\, \langle \mathbf{k}', \mathbf{q}+\mathbf{k}_j | \tau(j) | \mathbf{k}, \mathbf{k}_j \rangle\, |\Phi_o\rangle \tag{2.101}$$

If we assume that (KER 59) the dependance of the two-nucleon scattering amplitude $\tau(j)$ on the initial momentum $\mathbf{k}_j$ of the target nucleon j is negligible, then integration over $\mathbf{k}_j$ yields $(2\pi)^3\delta(\mathbf{r}_j-\mathbf{r}'_j)$ and

$$T_{fi}(\mathbf{k}',\mathbf{k}) = \langle\Phi_o| \sum_j (2\pi)^3 \langle \mathbf{k}', \mathbf{q} | \tau | \mathbf{k}, 0 \rangle$$
$$\int d\mathbf{r}_j \exp(i\mathbf{q}\cdot\mathbf{r}_j)\, |\Phi_o\rangle\ . \tag{2.102}$$

The two-nucleon matrix element is off the energy shell unless $\mathbf{q}=0$. Therefore, the matrix element depends on the incident energy as well as the momentum transfer $\mathbf{q}$. One can put

$$\langle \mathbf{k}', \mathbf{q} | \tau | \mathbf{k}, 0 \rangle = \tau(E, q^2) \tag{2.103}$$

which is related to the scattering matrix $M(E,q^2)$ by

$$M(E,q^2) = -(\mu_o/2\pi\hbar^2)\,(2\pi)^3\,\tau(E,q^2) \tag{2.104}$$

with μ_o being the two-nucleon reduced mass

$$\mu_o = \frac{m}{2}. \tag{2.105}$$

Recalling eqn.(2.33), we obtain the scattering amplitude in the impulse approximation as

$$f(\theta,\phi) = -(\mu_A/2\pi\hbar^2)\, T_{fi}(\mathbf{k}',\mathbf{k})$$

$$= (\mu_A/\mu_0) \langle\Phi_0| \sum_j \exp(i\mathbf{q}\cdot\mathbf{r}_j)\, M_j(E,q^2)\, |\Phi_0\rangle$$

$$= (2A/A+1) \langle\Phi_0| \sum_j \exp(i\mathbf{q}\cdot\mathbf{r}_j)\, M_j(E,q^2)\, |\Phi_0\rangle \qquad (2.106)$$

where we have used

$$\mu_A = (Am/A+1)\ . \qquad (2.107)$$

The first Born approximation for the scattering amplitude is obtained by substituting eqn.(2.30) into eqn.(2.21) and retaining only the first term. We get

$$f(\theta,\phi) \simeq -(\mu_A/2\pi\hbar^2) \int U(\mathbf{r}) \exp(i\mathbf{q}\cdot\mathbf{r})\, d\mathbf{r}\ . \qquad (2.108)$$

Substituting into eqn.(2.106) yields

$$(\mu_A/\mu_0) \langle\Phi_0| \sum_j \exp(i\mathbf{q}\cdot\mathbf{r}_j)\, M_j(E,q^2)\, |\Phi_0\rangle$$

$$= -(\mu_A/2\pi\hbar^2) \int U(\mathbf{r}') \exp(i\mathbf{q}\cdot\mathbf{r}')\, d\mathbf{r}'\ . \qquad (2.109)$$

Multiplying through by $\exp(-i\mathbf{q}\cdot\mathbf{r})$ and integrating over $d\mathbf{q}$ yields

$$U(\mathbf{r}) = -(2\pi\hbar^2/\mu_0) \int \exp(i\mathbf{q}\cdot\mathbf{r}) \langle\Phi_0| \sum_j \exp(i\mathbf{q}\cdot\mathbf{r}_j)\, M_j(E,q^2)\, |\Phi_0\rangle\, d\mathbf{q}\ . \qquad (2.110)$$

For a target nucleus with J=0 and T=0, the scattering matrix is given by eqn.(2.45) so that

$$U(\mathbf{r}) = -(2\pi\hbar^2 A/\mu_0) \int \exp(i\mathbf{q}\cdot\mathbf{r}) [f(q) + g(q)\underline{\sigma}\cdot\hat{n}]\, F(q)\, d\mathbf{q} \qquad (2.111)$$

where

$$F(q) = \langle \Phi_o | \exp(i\mathbf{q}\cdot\mathbf{r}) | \Phi_o \rangle \tag{2.112}$$

is the ground state form factor of the target nucleus.

Using notations developed above, we can write

$$V_c(r)\, F_c(r) = (\hbar^2 A/2\pi\mu_o) \int \exp(i\mathbf{q}\cdot\mathbf{r})\, \mathrm{Re}[f(q)]\, F(q)\, d\mathbf{q} \tag{2.113}$$

and

$$W_c(r)\, F_{ic}(r) = (\hbar^2 A/2\pi\mu_o) \int \exp(i\mathbf{q}\cdot\mathbf{r})\, \mathrm{Im}[f(q)]\, F(q)\, d\mathbf{q} \,. \tag{2.114}$$

If f(q) varies slowly compared with the form factor F(q), then, for elastic scattering,

$$V_c(r)\, F_c(r) \simeq (\hbar^2 A/2\pi\mu_o)\, \mathrm{Re}[f(q)] \int \exp(i\mathbf{q}\cdot\mathbf{r})\, F(q)\, d\mathbf{q}$$

$$= A\,(2\pi\hbar^2/\mu_o)\, \mathrm{Re}[f(0)]\, \rho(r) \tag{2.115}$$

where $\rho(r)$ is the ground state nuclear density of the target nucleon.

Similarly,

$$W_c\, F_{ic}(r) \simeq A\,(2\pi\hbar^2/\mu_o)\, \mathrm{Im}[f(0)]\, \rho(r) \,. \tag{2.116}$$

Also, for the spin-orbit terms, in the Born approximation,

$$f_{so} \simeq -(\mu_A/2\pi\hbar^2)\,(\hbar/m_\pi c)^2\, V_{so} \int \exp[i(\mathbf{k}-\mathbf{k}')\cdot\mathbf{r}]\, \frac{1}{r}\frac{d}{dr} F_{so}\, \underline{\sigma}\cdot(\mathbf{r}\times\hbar\mathbf{k})\, d\mathbf{r}$$

$$= -(\mu_A/2\pi\hbar)(\hbar/m_\pi c)^2 V_{so} \int \exp[i(\mathbf{k}-\mathbf{k}')\cdot\mathbf{r}]\, \underline{\sigma}\cdot(\nabla F_{so} \times \mathbf{k})\, d\mathbf{r}$$

$$= -(\mu_A/2\pi\hbar)(\hbar/m_\pi c)^2 V_{so}\, \mathbf{k}\cdot\underline{\sigma}\times \int \nabla\{\exp[i(\mathbf{k}-\mathbf{k}')\cdot\mathbf{r}]\} F_{so}\, d\mathbf{r}$$

$$= -(\mu_A/2\pi\hbar)\,(\hbar/m_\pi c)^2\, V_{so}$$

$$\mathbf{k}\cdot\underline{\sigma}\times i(\mathbf{k}-\mathbf{k}')\int\{\exp[i(\mathbf{k}-\mathbf{k}')\cdot\mathbf{r}]\}F_{so}\,d\mathbf{r}$$

$$= -(\mu_A/2\pi\hbar)\int \exp(i\mathbf{q}\cdot\mathbf{r})$$

$$[-(\hbar/m_\pi c)^2\, iV_{so}\, k^2\sin\theta\, F_{so}\, \underline{\sigma}\cdot\hat{n}]\,d\mathbf{r} \qquad (2.117)$$

where we have used

$$\mathbf{k}\cdot\underline{\sigma}\times(\mathbf{k}-\mathbf{k}') = k^2\sin\theta\ \underline{\sigma}\cdot\hat{n}\ . \qquad (2.118)$$

Comparing eqn.(2.117) with eqn.(2.108) and eqn.(2.111), we obtain

$$(\hbar/m_\pi c)^2\, V_{so}\, k^2\sin\theta\, F_{so}$$

$$= (2\pi\hbar^2 A/\mu_o)\int d\mathbf{q}\,\exp(i\mathbf{q}\cdot\mathbf{r})\,F(q)\,\mathrm{Im}[g(q)]$$

$$\simeq A\,(2\pi\hbar^2 A/\mu_o)\,\mathrm{Im}[g(0)]\,\rho(r)\ . \qquad (2.119)$$

Similarly,

$$(\hbar/m_\pi c)^2\, W_{so}\, k^2\sin\theta\, F_{iso} \simeq -A\,(2\pi\hbar^2 A/\mu_o)\,\mathrm{Re}[g(0)]\,\rho(r). \qquad (2.120)$$

Inspection of eqn.(2.115), (2.116), (2.119), and (2.120) reveals that, through the impulse approximation which is appropriate at high energies, we again obtain the same general form of the phenomenological optical model potential.

3. Experimental

3.1 General

The TRIUMF six-sector isochronous cyclotron accelerates H- ions to a maximum energy of 520 MeV. Extraction of beam is done by means of the insertion of a stripper foil, (carbon) the location of which can be adjusted to provide beams of continuously variable energies between 180 to 520 MeV. Figure 3.1 is a layout of the TRIUMF beam-line and experimental facilities.

The present experiment was done at beam line BL4B in the proton hall (figure 3.2). The target is located at 4BT2. A solid-angle defining front-end x-y drift chamber (FEC) is located 62.7*cm* from the target.

Downstream of the FEC is the vertical-bend, Medium-Resolution-Spectrometer (MRS) consisting of a quadrupole and a 60°-bend dipole magnet.

The location of particles in the focal plane is determined by means of two sets of vertical drift chambers (VDC's) oriented at 45° to the central ray.

Following the VDC's is an array of eight plastic scintillation counters. The pulses from these counters provide energy loss information of the particles. These counters are also used in conjunction with trigger counters at the spectrometer entrance to provide time-of-flight information. The time-of-flight together with the energy loss information is used to provide a 'cut' to discriminate

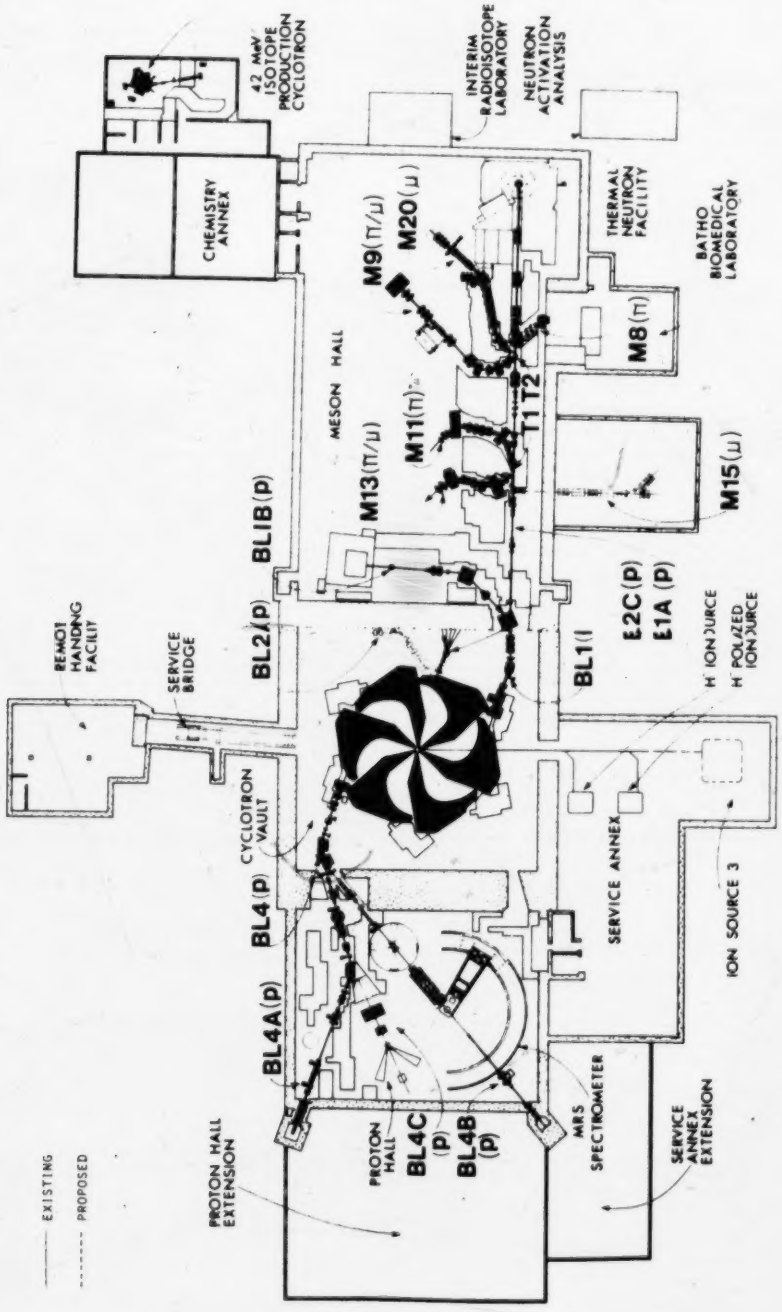

Figure 3.1 Layout of the TRIUMF beam-line and experimental facilities.

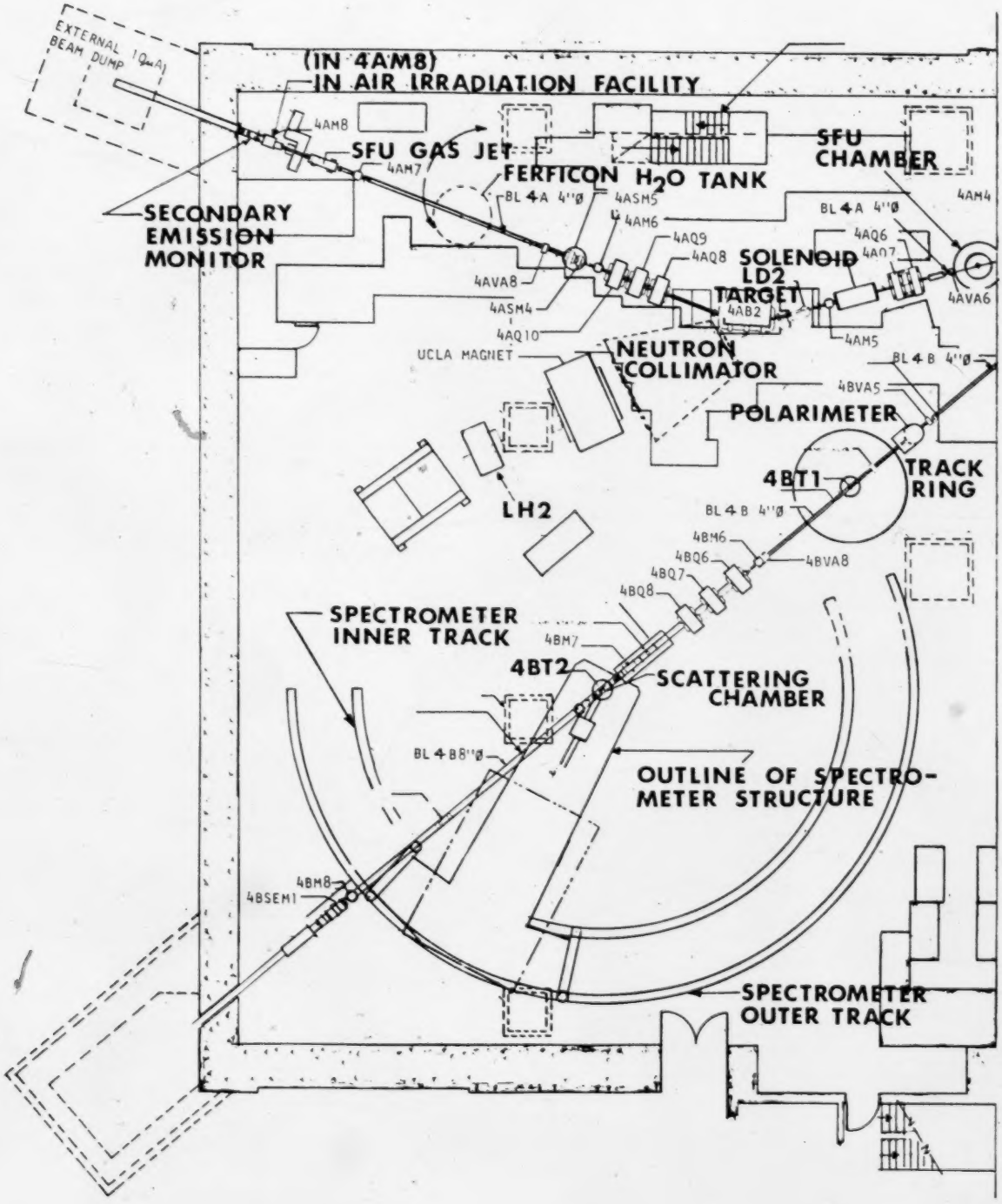

Figure 3.2 An layout showing beam-line BL4B in TRIUMF.

against scattered deuterons and tritrons having the same momentum as the elastically scattered protons.

The number of incident protons is measured by means of a left-right polarimeter located upstream of the scattering chamber. A CH2 target intercepts the incident beam and the charge measured by the polarimeter measures the incident proton flux.

Pulser generated 'events' are used to monitor the deadtime of the computer. The pulser generated signal is AND'ed with the polarimeter signal so that the number of pulser events is proportional to the beam current. This procedure is essential to ensure that the deadtime will not be affected by fluctuations in the beam current.

The MRS can be rotated about the target position so that angular distributions over the range of angles from 12° to 132° can be measured. The FEC and the target rotate with the MRS while the scattering chamber remains fixed. In the large angle configuration (LAC) a flexible aluminium 'bellows' connects the entrance of the FEC to any of the ports of the scattering chamber. These ports are located at scattering angles 28°, 57°, 103°, 128° and 152°. The minimum scattering angle attainable with the 28° port is about 14°. When operating in the LAC mode, the unscattered beam goes through a continuation of the beam pipe, exits through the opposite side of the scattering chamber, passes through a secondary emission moniter (SEM) and eventually is stopped in a beam dump located outside the south-west corner of the

proton hall. The proton beam current is limited to 100 *nA* at 500 MeV when running in this mode. The charge measured by the SEM provides a check on the beam current provided all or a constant portion of the beam is focused on the SEM.

For scattering angles less than 14°, the beam pipe downstream of the scattering chamber must be removed. The quadrupole magnet on the MRS is moved two meters upstream and a 'horn' is installed to replace the removed section of the beam line and to connect the scattering chamber to the FEC. The unscattered beam is stopped by a small beam-stop inside the 'horn'. When running in the small angle configuration (SAC), the beam current must be reduced to less than 0.2 *nA*.

3.2 The Target

The oxygen target consisted of distilled water sandwiched between two Kapton sheets mounted inside a cylindrical shell which was maintained at atmospheric pressure. This was seen to be necessary to prevent excessive bulging of the water target which would otherwise occur if the cell were evacuated.

An identical 'dummy' target cell without the water was installed in the target chamber so that background measurements could be obtained for each oxygen run.

3.3 Data Acquisition

Data acquisition is facilitated by CAMAC and the data acquisition program (DACS) using the Eclipse/200 computer in the MRS counting-room.

Data are acquired from CAMAC by issuing the command EA (Enable Acquisition). Events are processed on-line according to the event processing subroutine (EPROC) so that experimenters can modify the control parmeters as necessary until the desired spectra are obtained. The EA/T command is used to write all events on magnetic tape before processing on-line. On-line analysis moniters the quality of data; scalers and beam-quality spectra acquired on-line also shortens the time required for replay-analysis.

A listing of the EPROC subroutine for this experiment is given in appendix (A). Documentation on the data acquisition software (DACS) already exist (Tin 84) , and will not be discussed in detail here.

3.4 Schematics of The Multwire Drift Chambers (MWC's)

The particle trajactories are monitored by three sets of MWC's. The first MWC, located at the entrance of the spectrometer, is a low-pressure drift chamber. This is of dimensions 5" x 5" and consists of two geometrical planes, defining the 'X0' and 'Y0' axes, each in turn made up of two planes of wires, 32 each, 'offset' to give a coordinate on that axis. 'Y0' is the coordinate in the non-bend direction of the spectrometer and 'X0' is at right-angles to 'Y0'.

The other two sets of MWC's are vertical drift chambers located at the upper end of the spectrometer and oriented at 45° to the central ray of the spectrometer. These are of the 'MIT' type, each consisting of two wire planes. The first plane of wires runs perpendicular to the bend plane and generates the 'X' coordinate while a second plane of wires running at 30° to the 'X' wires determines the 'U' coordinate. The 'X','U' coordinates provided by the lower and upper VDC's are labeled X1,U1 and X2,U2, respectively.

3.5 Focal Plane Calculation

The focal plane geometry is shown in (figure 3.3). The constants G and H define the VDC's locations. F and δ define the focal plane location. The focal plane coordinate X_F is calculated by

$$X_F = [X1 + H - (F/G)(X1+H-X2)] /\{1-[(X1+H-X2)/G] \tan(\delta)\} \quad (3.1)$$

For this experiment, the values for F, G, H, δ are F=-4200, G=5472, H=7392, and δ=0.

3.6 Quadratic Aberration Correction

In order to obtain good resolution, X_F must be corrected for quadratic aberration. The corrected focal plane coordinate, XFCC, is calculated from

$$XFCC = (Y0-C)^2/A + THPC^2/B + X_F \quad (3.2)$$

where

$$THPC = (R \cdot THET + S \cdot X_F)/T + Q \qquad (3.3)$$

with A=-5000, B=-60, C=-810, R=10000, S=-70, T=10000, and Q=-175, all determined empirically.

THET is the angle of trajactory as shown in (figure 3.4). There,

$$\begin{aligned} &\tan(45°+THET) \\ &\quad = G/(H+X1-X2) \\ &\quad = (1+\tan(THET))/(1-\tan(THET)) \\ &\quad = 1/(1-2\cdot THET) \qquad \text{for small THET.} \end{aligned} \qquad (3.4)$$

Thus,

$$THET = [G-H+X2-X1]/2 \ . \qquad (3.5)$$

For G and H having the values given above, THET is given by

$$THET = 0.0914(X2-X1)-175 \qquad (3.6)$$

in milliradians.

To check the quadratic correction, it is useful to form a spectrum of X0 against XFCC, (SXFX0). If the target is heavy (e.g. Pb), the kinematic shift is small so that one should see straight verticle bands with constant XFCC (figure 3.5) if the quadratic correction is applied properly.

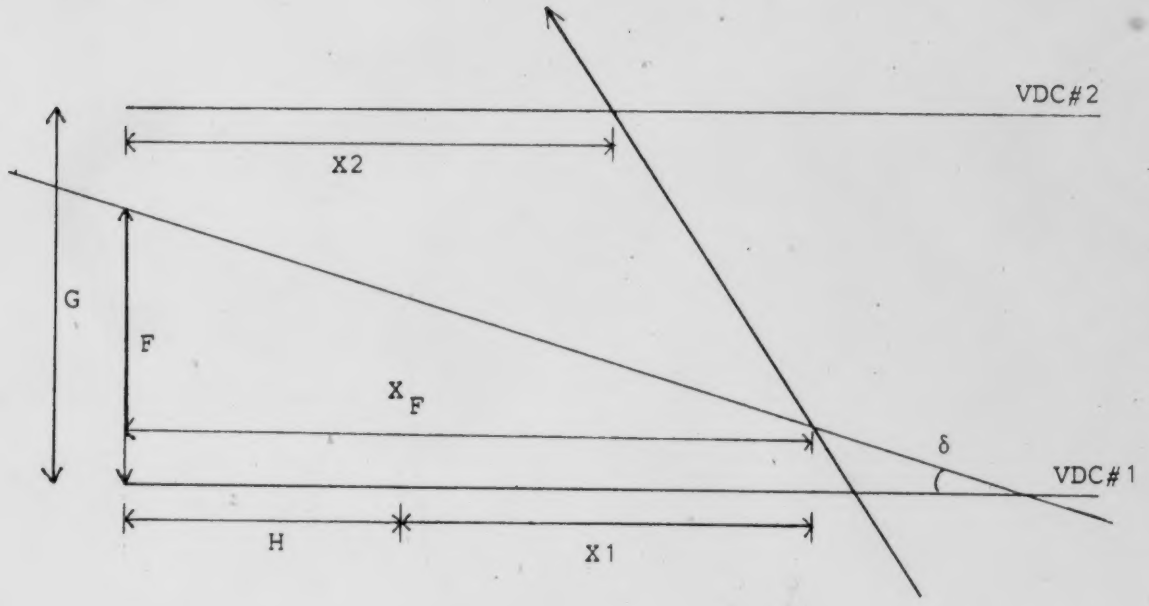

Figure 3.3 The focal plane geometry of the MRS.

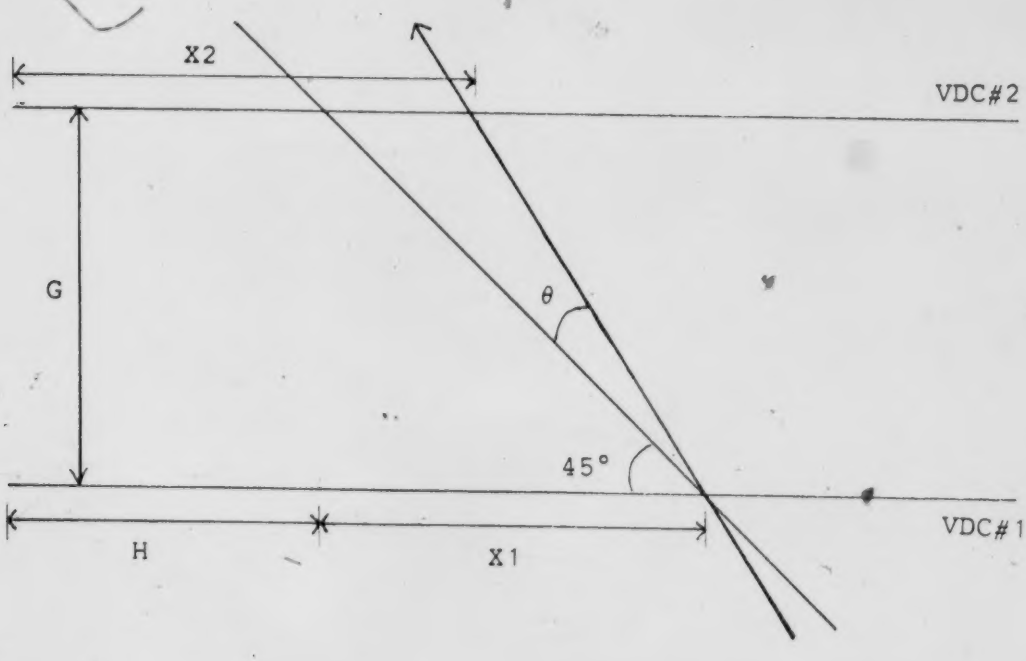

Figure 3.4 Diagram of the angle of trajactory, THET, through the VDC's

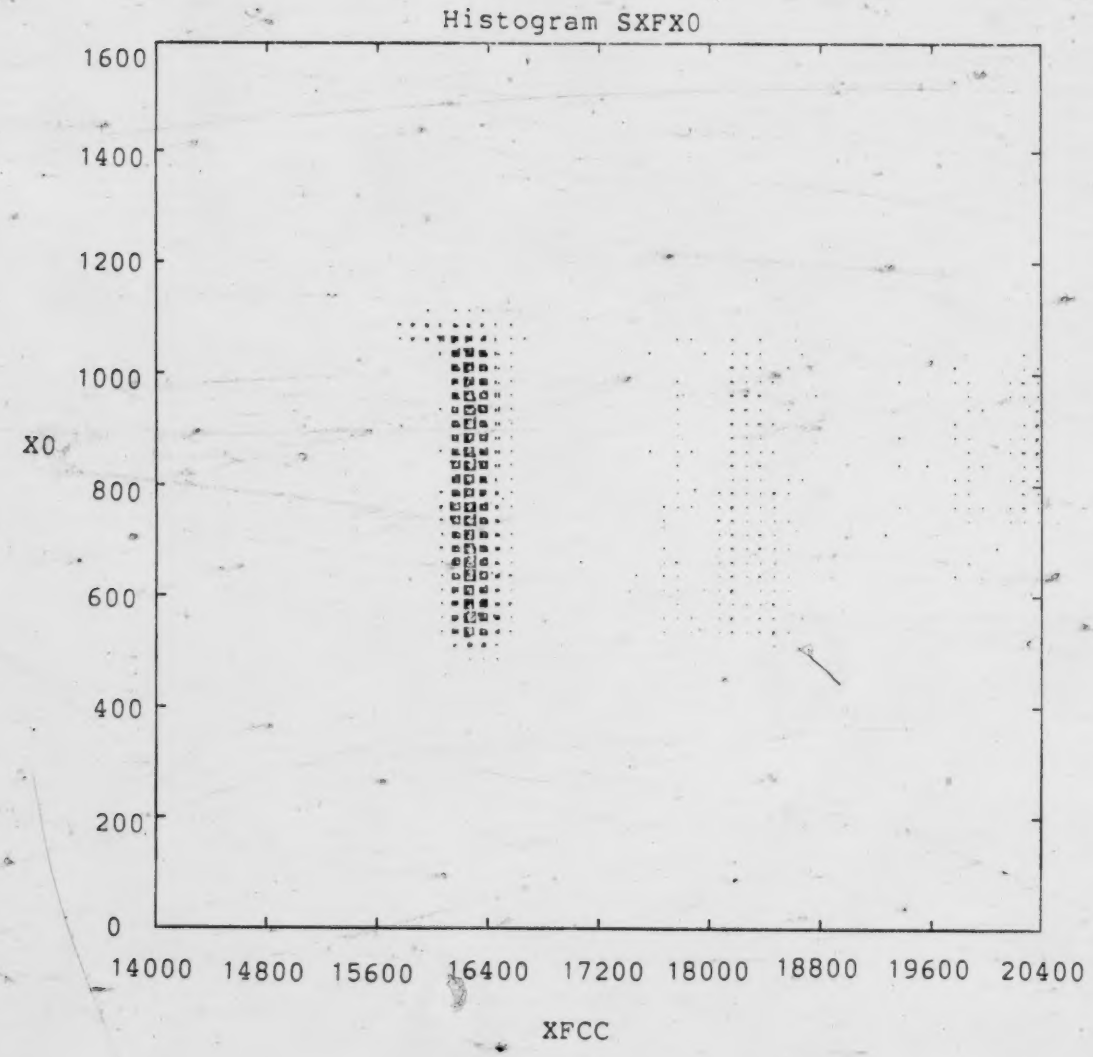

Figure 3.5 An SXFX0 spectrum showing vertical bands of constant XFCC.

3.7 Kinematic Shift Correction

When a light target nucleus is used, the focal plane coordinate will be coupled to the scattering angle by kinematic shift. To correct for this, one lets XFCC depend on Y0. The kinematically corrected focal plane coordinate XFK is calculated from

$$XFK = (L \cdot XFCC + N \cdot Y0)/P + M \ . \tag{3.7}$$

The kinematic shift is energy and angle dependent so that the 'constants' L, M, N, P have to be found for each energy and angular region.

To check the kinematic correction, (with quadratic aberration corrected), one looks at the spectrum of XFK plotted against Y0, (SXFY0). If the correction is properly applied, vertical bands of nearly constant XFK should be seen (figure 3.6).

If the focal plane calculation, the quadratic aberration, and the kinematic shift corrections are applied property, vertical bands of constant XFK should be obtained in the spectrum of THPC plotted against XFK, (SXFTH). (Figure 3.7.)

3.8 Particle Identification

Particle identification is achieved by plotting the scintillator pulse height against the time-of-flight from bottom to top (TTB). (Figure 3.8.) The intense peak seen in this scatter plot consists of protons with the correct TTB

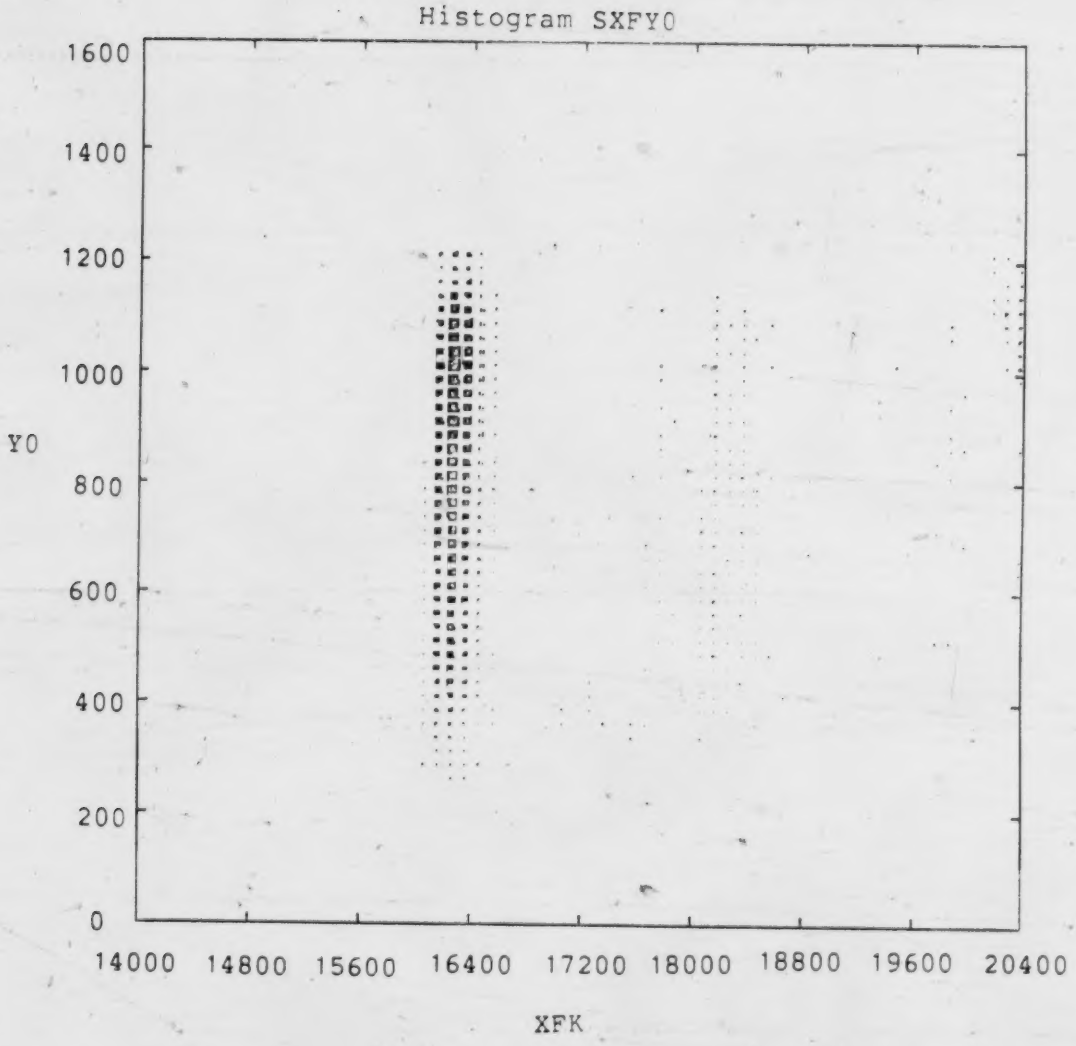

Figure 3.6 An SXFY0 spectrum showing vertical bands of constant XFK.

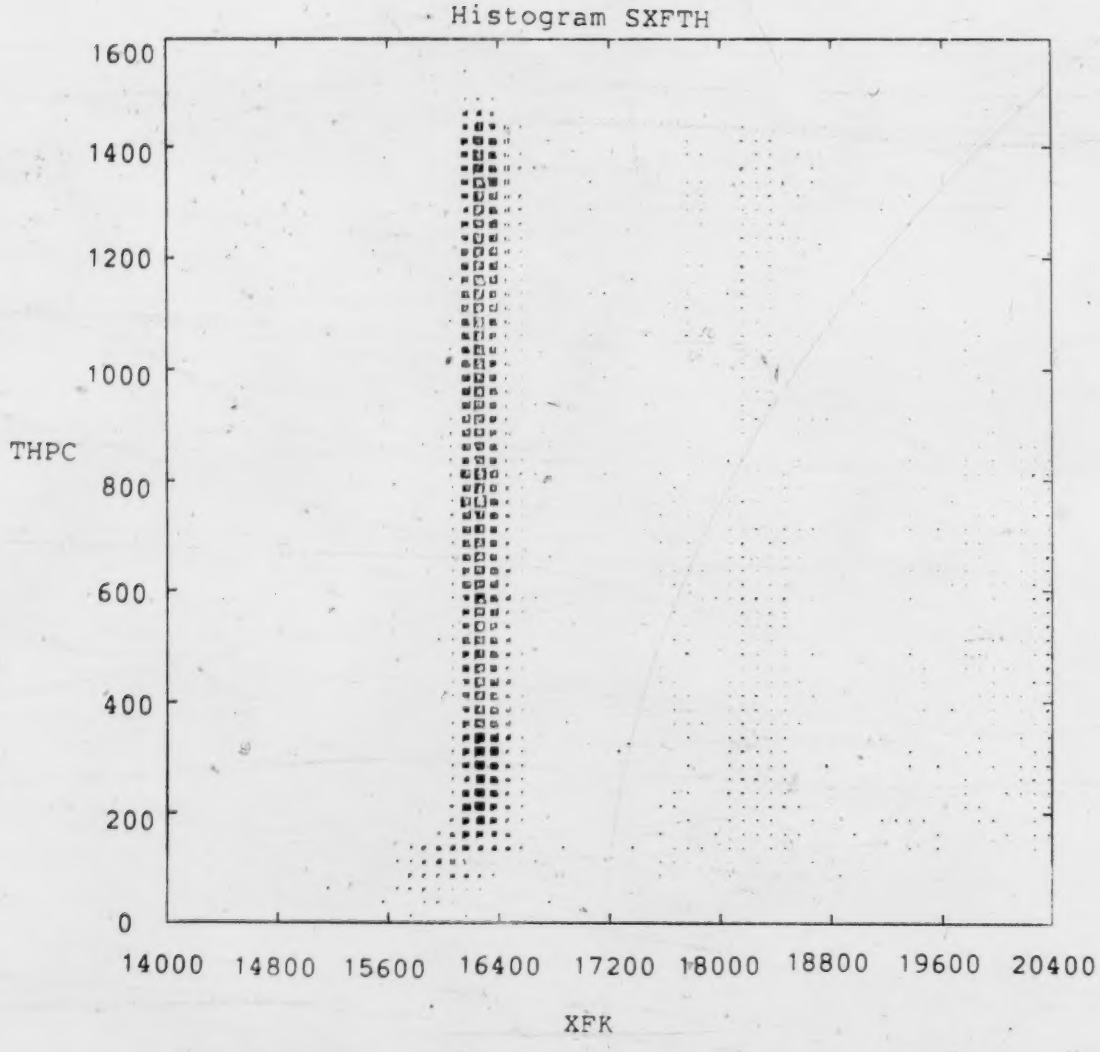

Figure 3.7 An SXFTH spectrum showing vertical bands of constant XFK.

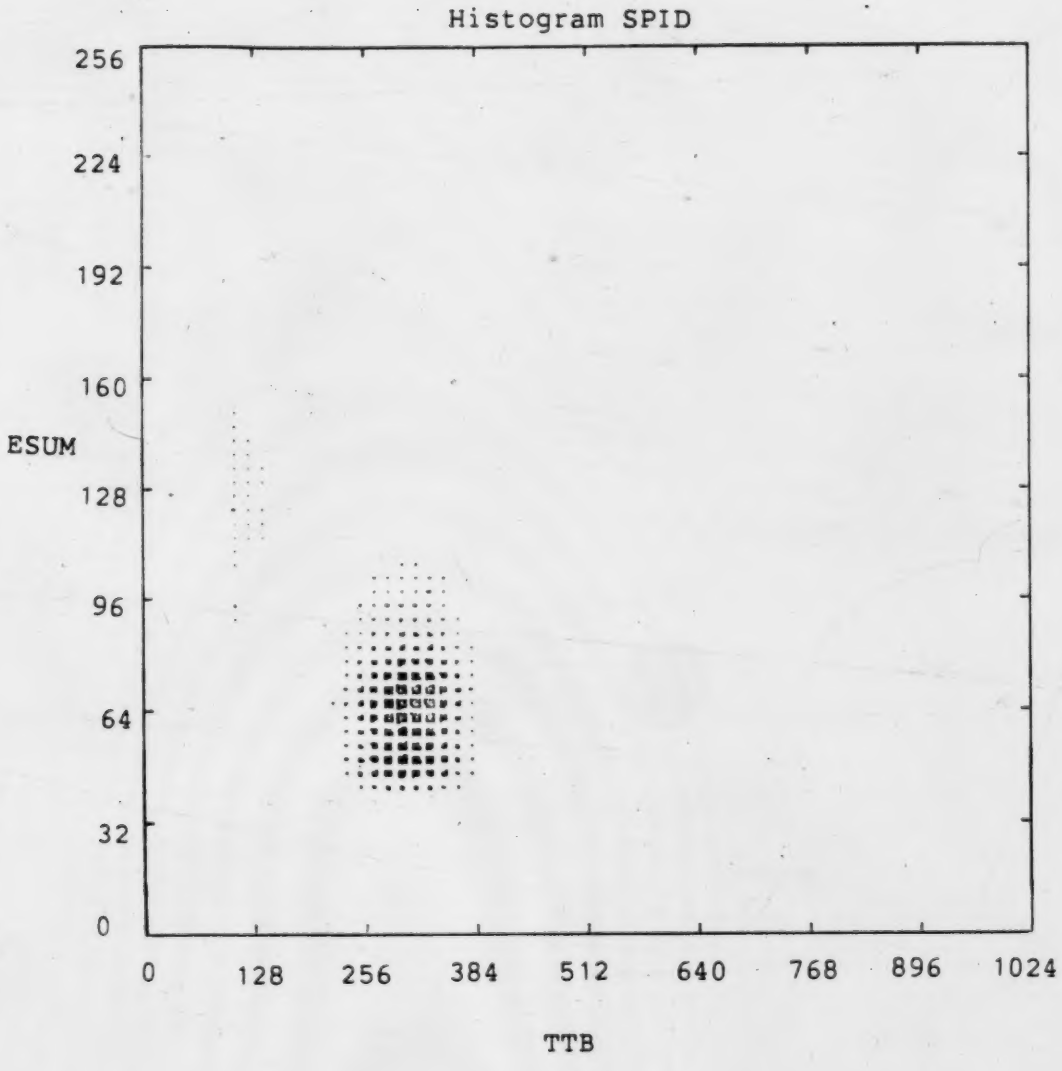

Figure 3.8 A particle identification scatter plot (SPID) showing proton and deuteron peaks.

values. A window around the proton peak selects the proton events. The fainter peak at the upper left corner of the proton peak corresponds to deuterons.

This scatter plot must be checked from time to time during the experiment to see that not too many deuterons are coming into the system. If the proton peak appears 'double', it is likely that the beam has two energies.

3.9 The Drift Chamber Decoding

Twenty-three CAMAC TDC modules are required to encode all the wire chamber signals. There are thirty-two channels in each module. Each wire in the MWC system is attached to a TDC channel. Thus, the sixteen wires in the first of the X0-defining planes are given TDC channels 0 to 15, and the second of these planes given channels 16 to 31, etc. The complete scheme of numbering is given in table 3.1.

The TDC's are used in a common stop mode so that the first one triggered has the largest time value, i.e. the shortest distance from the particle track to the wires corresponds to the largest TDC time, and vice versa.

For the front end chamber (FEC), the assignment of TDC channels in either set of the two axis-defining planes is shown in figure 3.9. The 'numbering' of wires is given by

$$\begin{aligned} n &= \text{chn\#} && \text{(first plane)} \\ n &= 31 - \text{chn\#} && \text{(second plane)} \end{aligned} \tag{3.8}$$

so that wire n in the first plane is adjacent to wires n and

Table 3.1 Table of TDC channel assigment to the MWC wires.

Plane	Name	Module	# TDC's	lower chn.	upper chn.
1	$X0_1$	0	16	0	15
2	$X0_2$	0	16	16	31
3	$Y0_1$	1	16	32	47
4	$Y0_2$	1	16	48	63
5	U1	2-16	160	64	223
6	X2	7-12	176	224	399
7	U2	12-17	176	400	575
8	X1	18-22	160	576	735

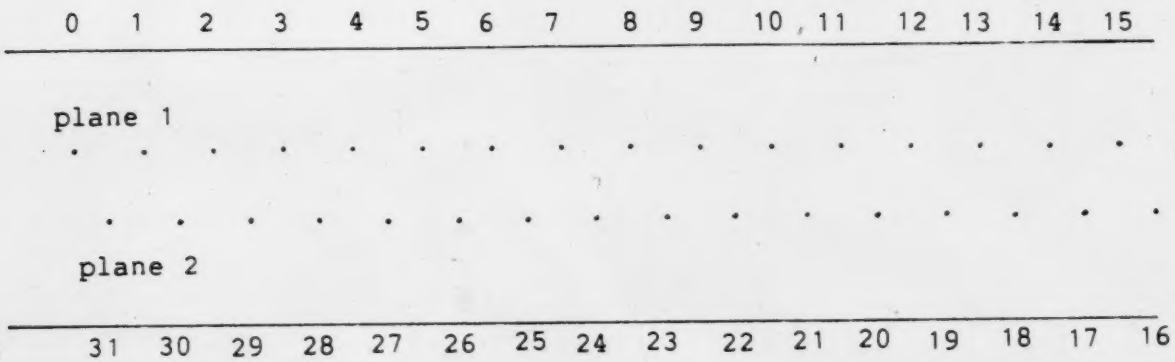

Figure 3.9 Schematic diagram showing the numbering, and the relative position, of the wires in the FEC.

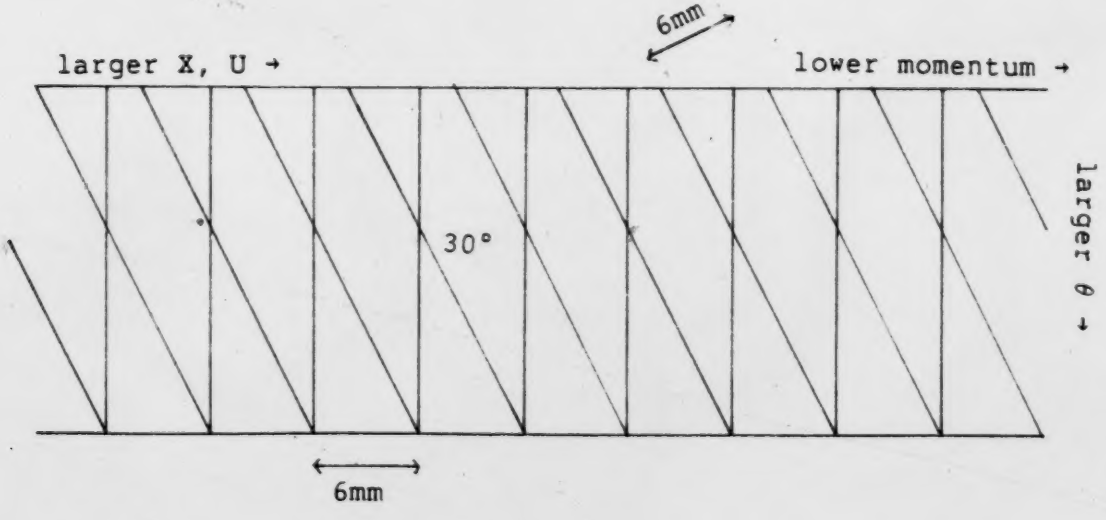

Figure 3.10 Schematic diagram showing the 'X' and 'U' wires in a VDC drift chamber.

n-1 in the second plane. The advantage of this numbering scheme is that adjacent wires in two different planes also have adjacent numbers.

The position of a 'hit' in the FEC can be calculated as follows. [2] There are three cases to consider.

1) Only the first plane is hit: in this case, the location, say X, is given by

$$X = N1 \cdot M \tag{3.9}$$

where M is a metric constant representing the intrinsic chamber resolution. In this experiment, M is 100μ.

2) Only the second plane is hit: in this case, X is given by

$$X = (N2 - \frac{1}{2})M \ . \tag{3.10}$$

The 1/2 takes into account the fact that the second plane is 'offset' as shown in figure 3.9.

3) Both axis-defining planes are hit: in this case, X is given by

$$X = (N1 \cdot M) + \Theta\,[(TDC2-TDC1)/DELT + M/4] \tag{3.11}$$

where

$$\Theta = 2(N2-N1)+1 \quad = +1 \ , \ N1=n, \ N2=n$$

$$= -1 \ , \ N1=n, \ N2=n-1 \ . \tag{3.12}$$

DELT is, in principle, the maximum difference of the TDC

---

[2] *The following discussion is based on the MWC decoding subroutine DRIFT (appendix B).*

time values of the two hits (TDC2-TDC1). DELT is usually set at 50.

The configuration of the X,U wires in the verticle drift chambers (VDC's) is shown in figure 3.10. Let us consider the X wires only, the U wires can be treated in a similar fashion.

Recall that the VDC's are oriented at 45° to the central ray. Consequently, a single particle track would trigger three to five adjacent wires as shown in figure 3.11. With three adjacent TDC's, the position at which the particle crosses the wire plane, the angle of the trajactory, and the time of passage of the particle can be calculated. If we define

N = channel number with the largest non-overflow TDC time value

T_{max} = largest TDC value

T_{min} = minimum of T_{N+1} and T_{N-1},

then

$$\theta = T_{max} - T_{min} \tag{3.13}$$

$$T_{mean} = T_{max} + (1/2)\,|(T_{N+1} - T_{N-1})| \tag{3.14}$$

and

$$X = M' \,[N - (1/2)(T_{N+1} - T_{N-1})/(T_{min} - T_{max})] \tag{3.15}$$

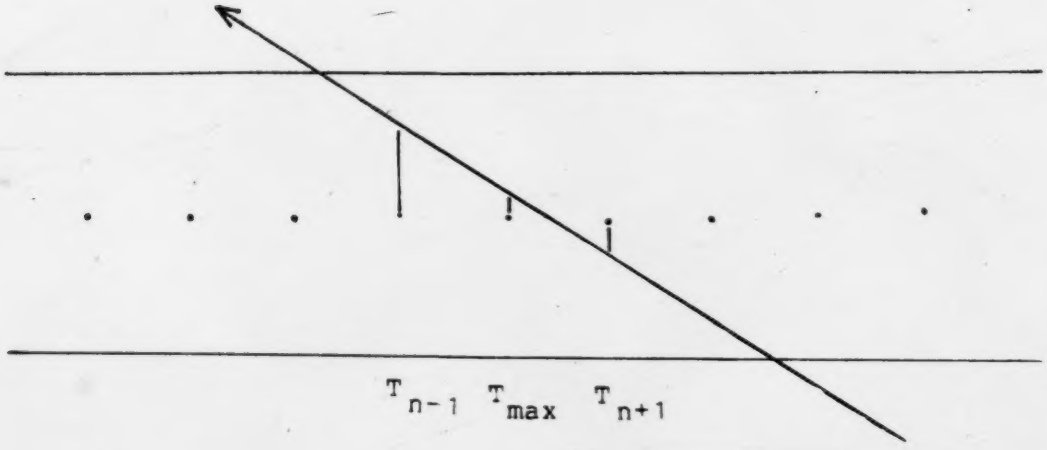

Figure 3.11 Diagram showing a particle trajactory through a VDC drift chamber.

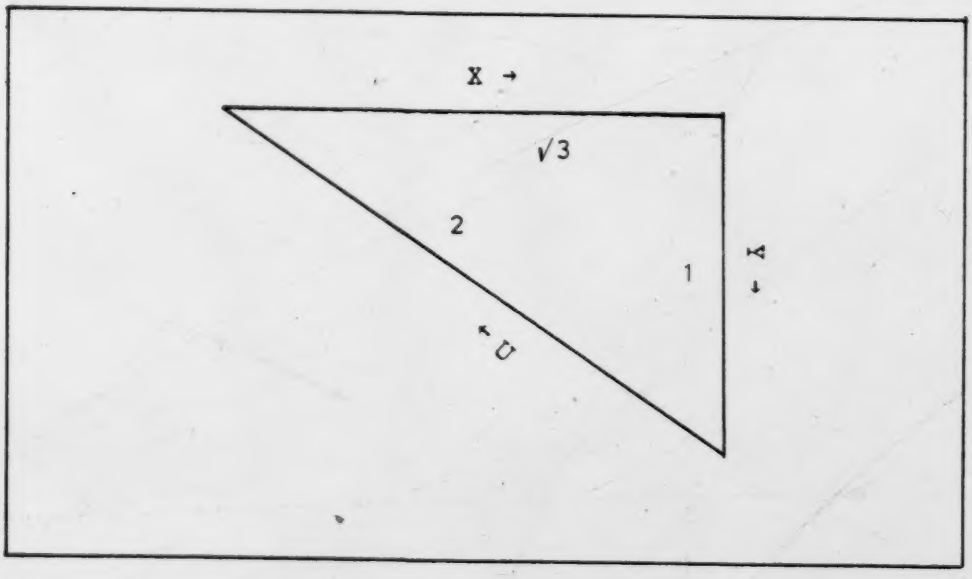

Figure 3.12 Vector diagram showing the calculation of 'Y' from 'X' and 'U' of the VDC's

where M'=120 since two adjacent anode wires are 6*mm* apart and the calculated resolution is about 50μ.

The position in the U plane can be calculated in a similar way. The coordinate Y can be calculated with the help of figure 3.12. Vectorially,

$$Y = \sqrt{3}\, X - 2U \quad . \tag{3.16}$$

In absolute value,

$$Y = \sqrt{3}\, X - 2U + C \tag{3.17}$$

where C is given by

$$Y_c = 0 = \sqrt{3}\, X_c - 2U_c + C \quad . \tag{3.18}$$

To locate Y_c at the centre of the chamber, X_c and U_c must be given values as shown in table (3.2). The relative channel numbers measure the position within the plane, in units of M'=120 μm per channel.

Table 3.2 Table of the *central* 'X' and 'U' TDC# and the corresponding relative channel number.

	TDC#	Relative chn#
$X1_c$	648	8640
$U1_c$	136	8640
$X2_c$	312	10560
$U2_c$	488	10560

4. Method of Analysis

4.1 Investigation of The Drift Chamber Efficiencies

If the MWC's are functionally operative, their overall inefficencies can be corrected by a correction factor [3]

MWCOR = (# proton events) / (# 'good' MWC events) (4.1)

A 'good' MWC event is classified as a non-'missing' and non-'multiple' event. 'Missing' and 'multiple' events are defined in table 4.1.

In the replay analysis, the efficiencies of the VDC's are checked against each other. 'Good' events in VDC#1 which have passed through the 'proton-window' (time-of-flight and energy loss window) and the solid angle window are used to define good events presented to VDC#2. A two-dimensional histogram of {ok,missing,multiple} of X2 against {ok,missing,multiple} of U2 is formed for these events (figure 4.1).

'Missing' in one plane (either X2 or U2) or 'multiple' in one plane represents 'genuine' inefficency of VDC#2, if their numbers are small. These events can be rejected and be corrected for by the correction factor.

However, 'missing' in both planes (X2 and U2) are probably due to false triggering of VDC#1. The number of these events should be small.

---

[3] *This formula will be given in a later section.*

Table 4.1 Table of definition for 'missing' and 'multiple' events in the MWC's

	Number of clusters		# adjacent wires hit	
FEC	0	> 1	< 1	>1 or >2
VDC's	0	> 1	< 3	—
	missing	multiple	missing	multiple

Table 4.2 Table of number of events in the {ok,missing,multiple} VDC#2 histogram shown in figure (4.1)

multiple	1568	47	1492
missing	315	8	37
ok	71557	196	1882
	ok	missing	multiple

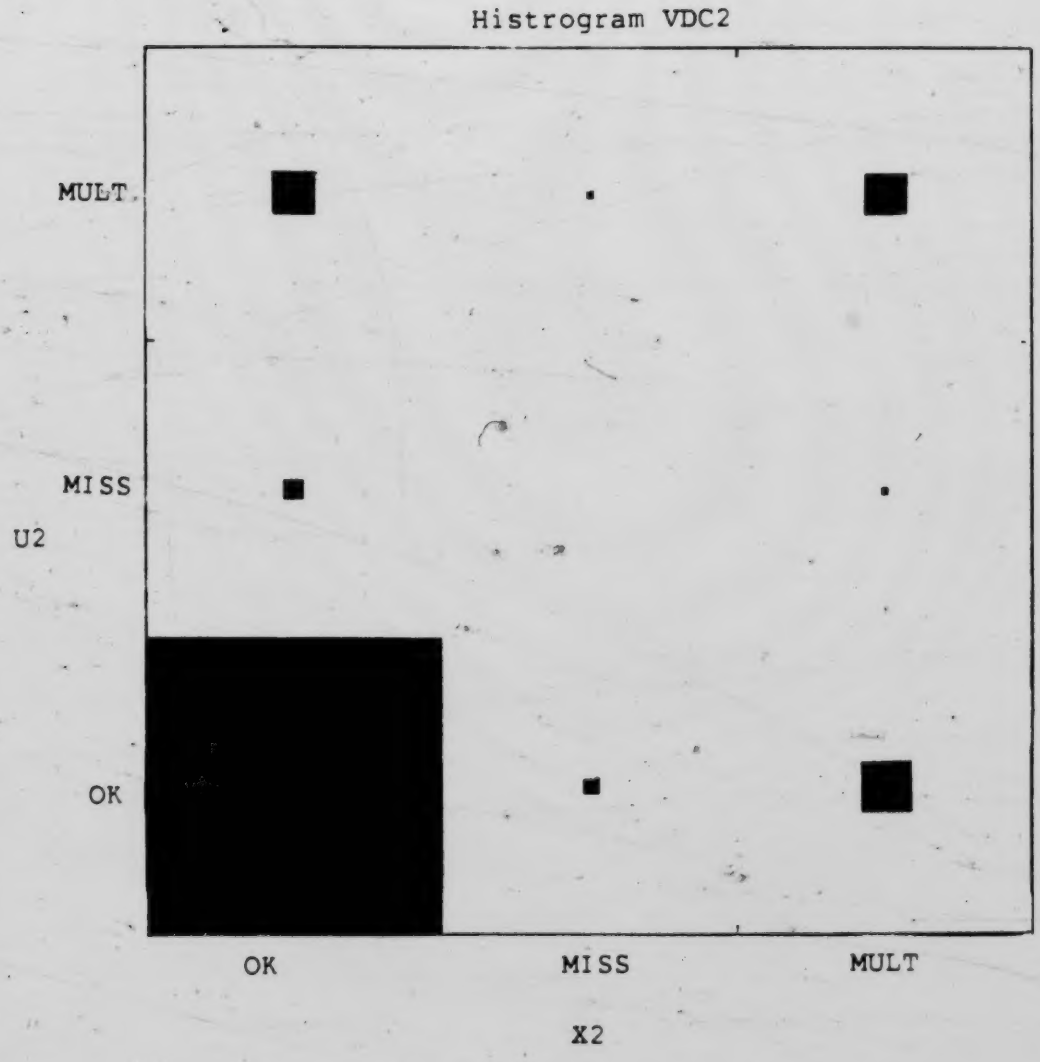

Figure 4.1 {ok,missing,multiple} scatter plot of VDC#2.

'Multiple' in both planes, on the other hand, might be due to multiple particle-tracks; if the number of these events is small, they can also be rejected and corrected for.

The efficiency of VDC#1 can similarly be tested against VDC#2. (Please see figure 4.2.)

For the front end chamber (FEC), 'good' triggers in both VDC#1 and VDC#2 are used to define a genuine particle trajectory. In addition, the PHI-window (Y2-Y1) and the THET-window are used to select trajectories that must have passed through the FEC. An 'efficiency-histogram' similar to that described for the VDC's is plotted for X0 and Y0. (See figure 4.3.) The analysis of it follows the same kind of reasoning outlined for the VDC's. Again, 'double-missing' and 'double-multiple' events should be small.

The actual number of events for each of the histograms discussed above are given in table 4.2 to table 4.4. The absolute small numbers of 'double missings' and the relatively small numbers of 'multiple' events indicate that the MWC's were in good working order.

4.2 Maximum Number of Adjacent Triggered Wires In The Front-end-chamber

There exists a possibility that ,for the FEC, two adjacent wires in the the same wire plane may be triggered by a single track as shown in figure 4.4. We investigated this possibility by allowing the number of triggered adjacent wires (NHIT) to have a maximum value of two in the

Table 4.3 Table of number of events in the {ok,missing,multiple} VDC#1 histogram shown in figure (4.2).

	ok	missing	multiple
multiple	1593	54	1624
missing	302	1	22
ok	71557	177	1989

Table 4.4 Table of number of events in the {ok,missing,multiple} FEC histogram shown in figure (4.3).

	ok	missing	multiple
multiple	1958	4	2017
missing	87	5	3
ok	75166	67	1999

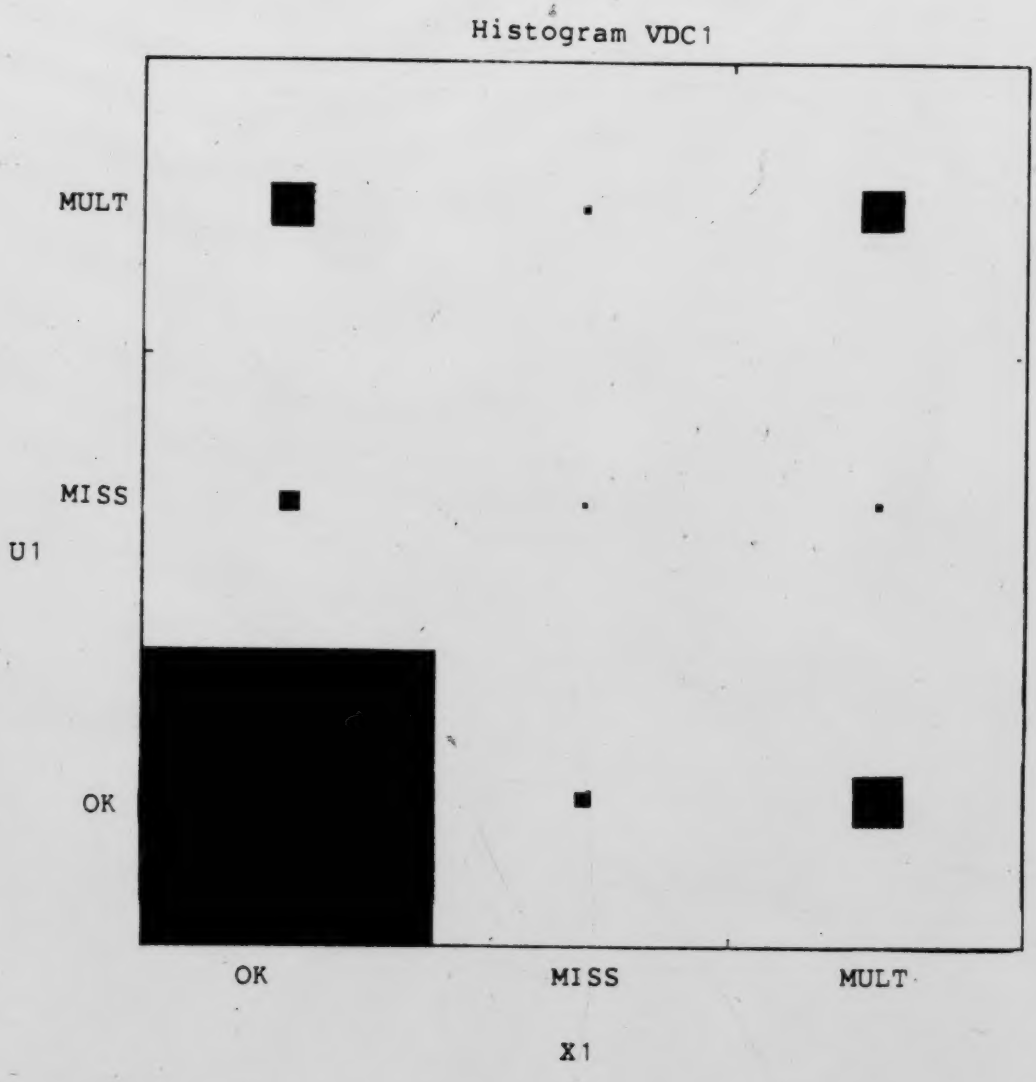

Figure 4.2 {ok,missing,multiple} scatter plot of VDC#1.

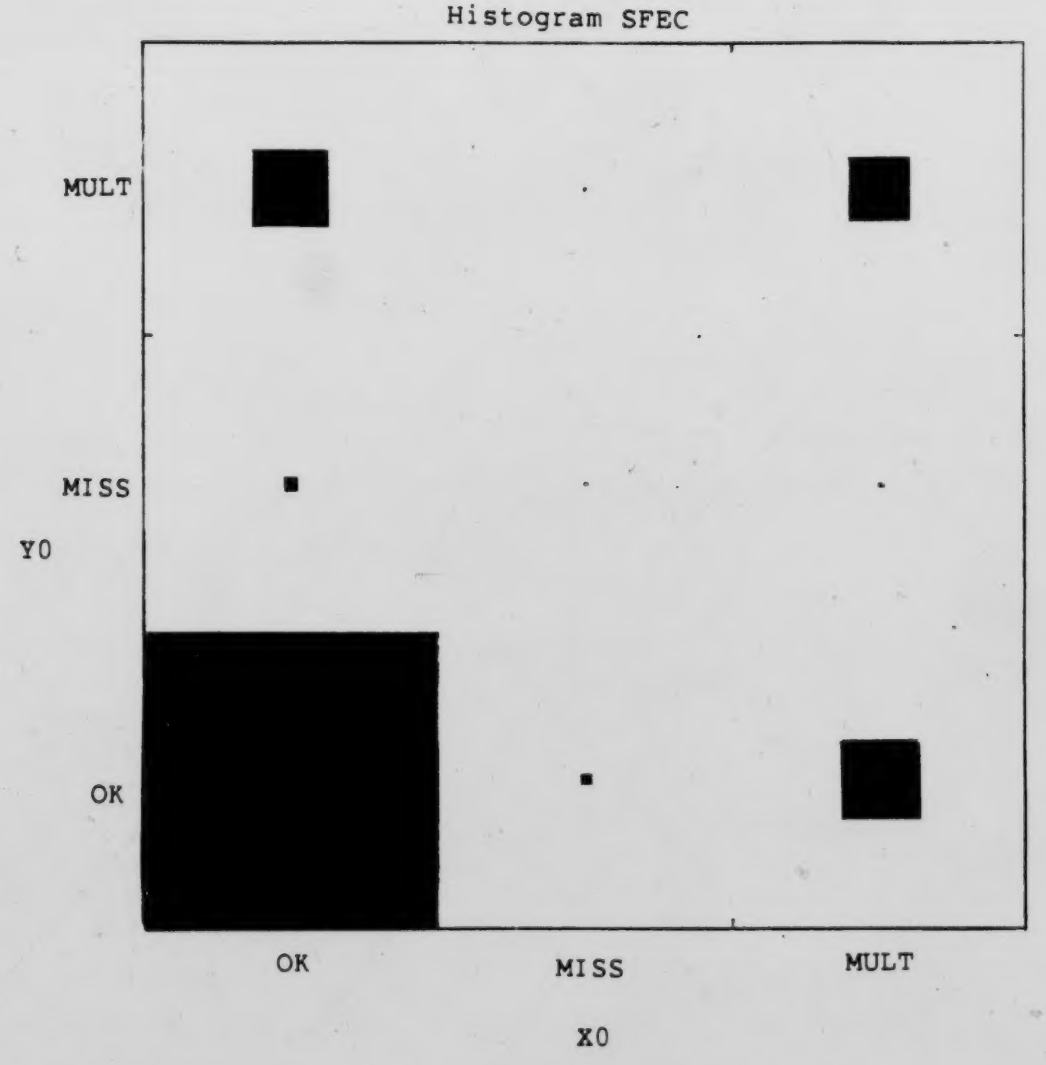

Figure 4.3 {ok,missing,multiple} scatter plot of FEC.

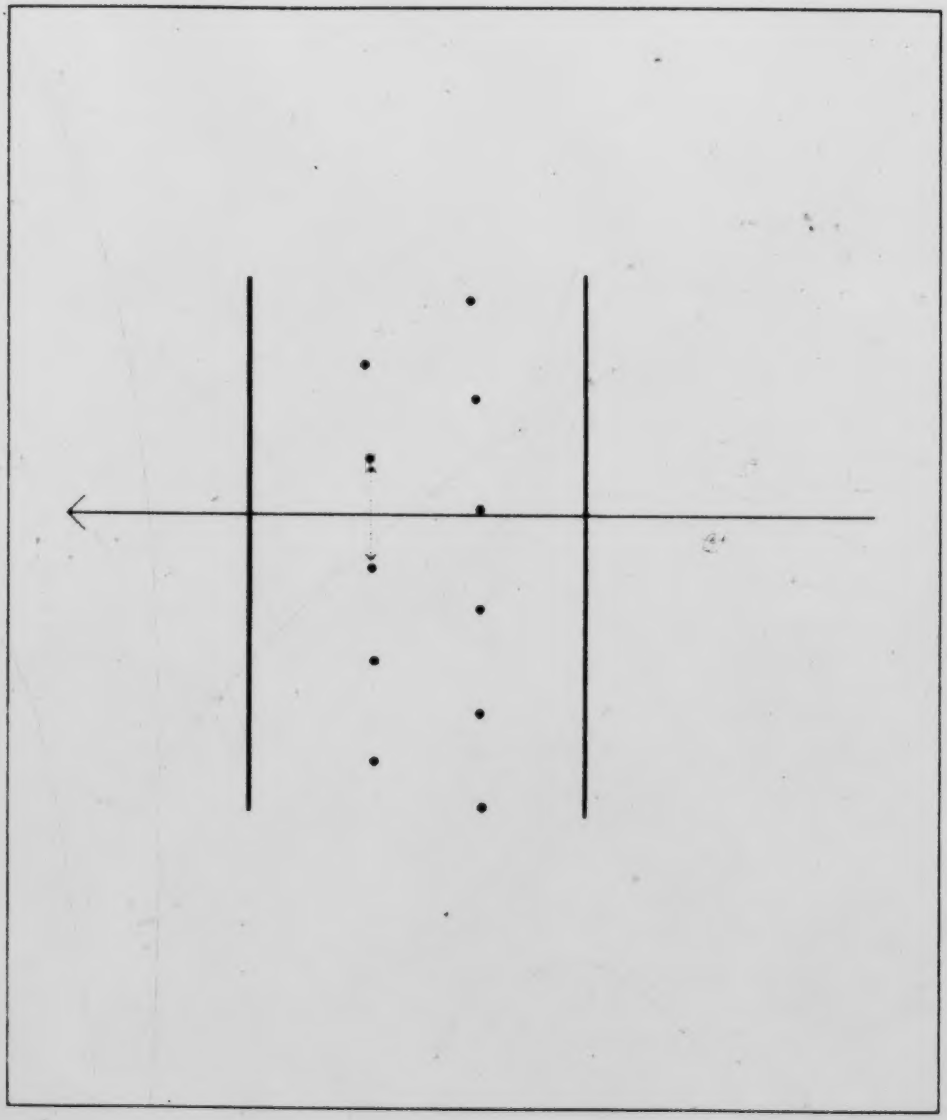

Figure 4.4 Diagram showing the possibility of a single particle track triggering two adjacent wires in the FEC.

FEC. The FEC efficiencies of the two alternatives were obtained by the above outlined method. The results are given in table 4.5 and table 4.6.

A comparision of the values given in the tables shows that 'multiple', and particularly 'double-multiple' events are reduced considerably with NHIT≤2.

In the replay analysis, we allowed a maximum of two adjacent 'hits' in each axis-defining FEC wire plane.

4.3 Determination of The Central Ray Location In The Solid angle Defining Front-end-chamber

The large momentum acceptance of the MRS allows the solid angle to be divided into smaller momentum bins. In order to define the scattering angle corresponding to each bin, one has to determine the central wire channel of the Y0 plane corresponding to the MRS central momentum ray.

Due to the large momentum acceptance of the MRS, protons scattered elastically and inelastically, leading to the first excited state of the oxygen nucleus, can be focused at the focal plane simultaneously. The ratio, ν, of the number of elastically scattered protons to the number of these inelastically scattered protons is a function of the scattering angle. At an angular region where this ratio varies rapidly with the scattering angle, ν can then be used to determine the scattering angle. The relationship between ν and the scattering angle can be found by dividing the solid angle into several bins and plotting the ratio ν

Table 4.5 Table of number of events in the {ok,missing,multiple} FEC histrogram for NHIT ≤ 1.

	ok	missing	multiple
multiple	5026	7	3372
missing	164	5	13
ok	75036	70	5137

Table 4.6 Table of number of events in the {ok,missing,multiple} FEC histrogram for NHIT ≤ 2.

	ok	missing	multiple
multiple	2276	5	2281
missing	172	5	5
ok	81646	72	2368

corresponding to each bin as a function of the centre 'Y0' wire channel of that bin.

When the quadrupole magnet of the spectrometer is turned off, the horizontal focusing property of the spectrometer is lost and only the central ray will reach the focal plane. The SXFY0 spectra with the quadrupole turned on and off, figure 4.5 and figure 4.6, show this clearly. (See section on focal plane calculations.)

Thus, from the ν-ratio vs. Y0-channel graph, the cental momentum 'Y0' channel is that corresponding to the ν-ratio when the quadrupole is turned off. This is shown in figure 4.7. The central 'Y0' channel determined in this way is Y0=770. The uncertainty is about 20 channels, corresponding to an uncertainty of 0.0016 radians in the scattering angle, or 0.09 degrees.

4.4 Determination of Energy Loss In Target

Since we do background subtractions by subtracting the differential cross section obtained from the target-empty run from that of the target-full run, we must be sure that counts in the appropriate XFK channels are used to calculate the target-empty differential cross section.

Since the beam loses energy in passing through the water in the full-target, the focal plane position of the elastic peak would be shifted towards higher XFK values. The energy loss in water can be obtained from the stopping power of water for protons ($-\frac{1}{\rho}\frac{dE}{dx}$). For example, at 200 MeV the

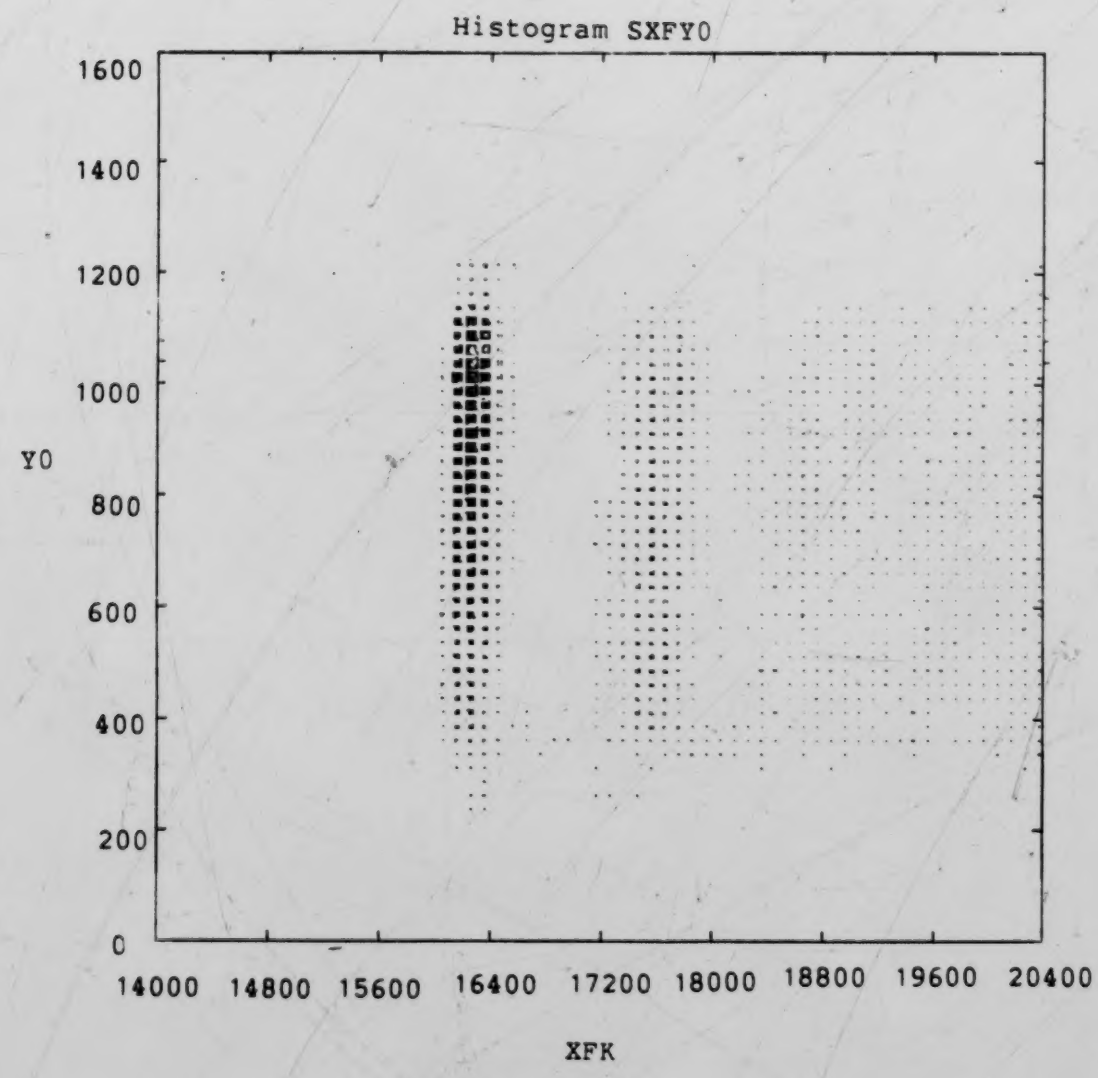

Figure 4.5 Spectrum showing the Y0 angular byte accepted by the spectrometer when the quadrupole is on.

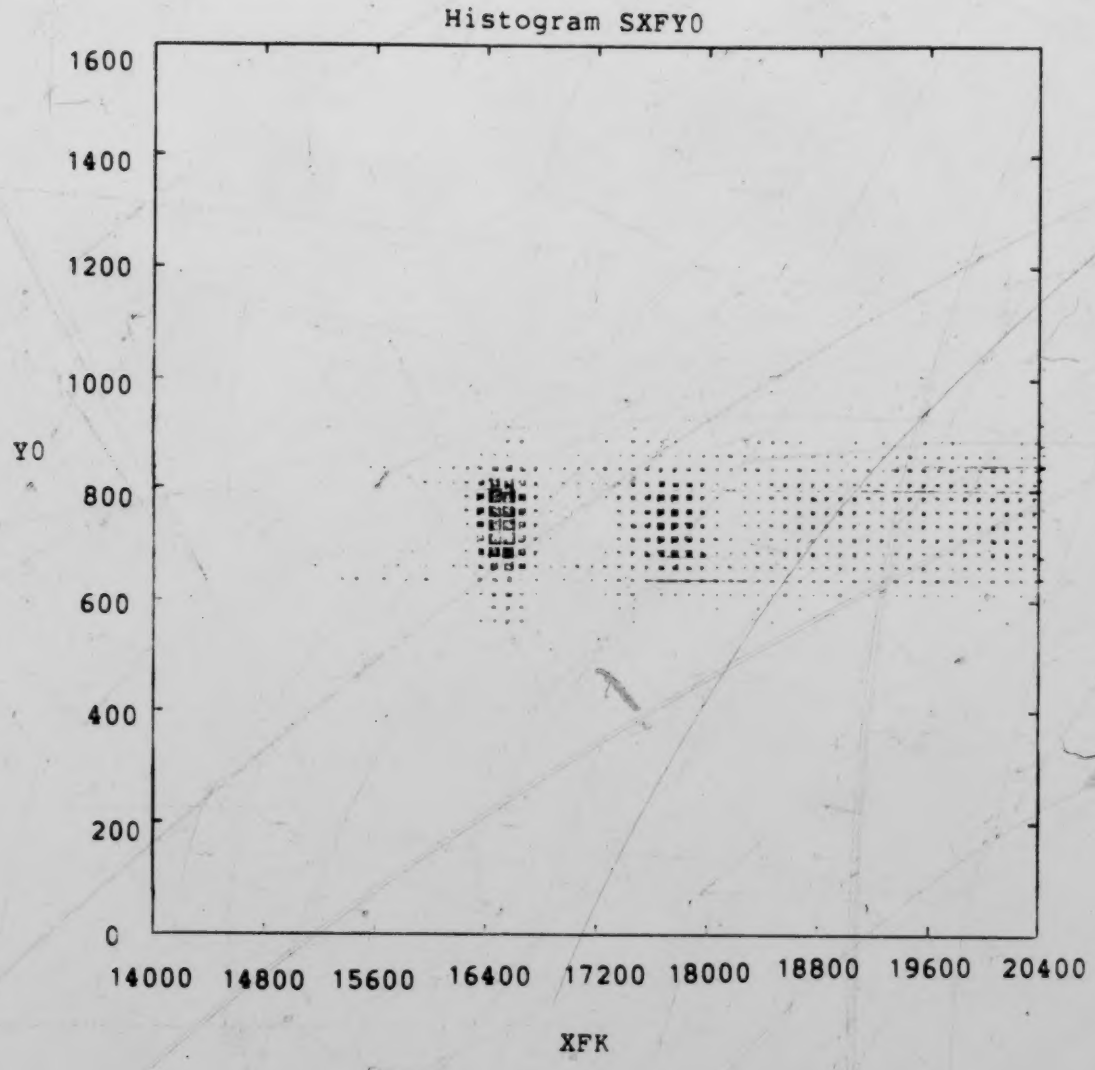

Figure 4.6 Spectrum showing the Y0 angular byte accepted by the spectrometer when the quadrupole is off.

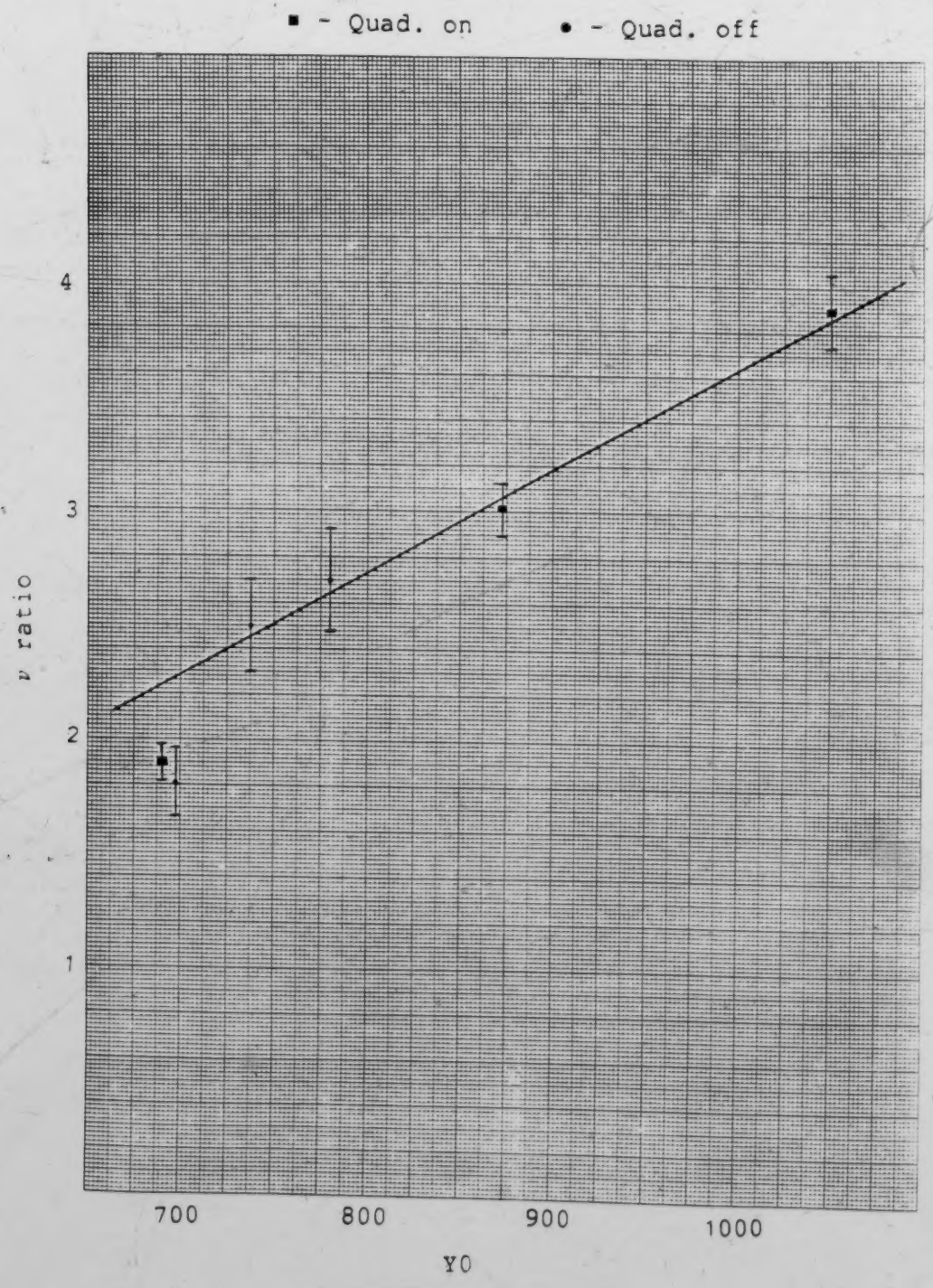

Figure 4.7 Graph of ground state to first excited state scattering ratio against Y0.

mass attenuation is about 4.55 *MeV-cm²/gm* (TRI KH). Assuming the target thickness to be about 0.145 *gm/cm²*, (this will change slightly as the target rotates,) the energy loss is about 0.66 MeV.

To determine the energy difference per XFK channel, we use the separation of the peaks corresponding to the carbon ground state and the first excited state, which is known to be 4.43 MeV. The energy per XFK channel is then found to be 4.9 KeV/channel. Hence, for 200 MeV, the energy shift is about 135 channels. Similarly, the energy shift for 300, 400, and 500 MeV are 107, 92, and 81 channels, respectively.

For illustration, at 200 MeV, if the target-full elastic peak is centred between channels 16000 to 17000, then the background subtraction should be taken from channel 15865 to 17865 of the target-empty SXF spectrum.

4.5 Calculation of The Differential Cross Section

Extraction of the elastic differential cross section from the raw data is essentially counting the number of events in the elastic peak, calculating the deadtime correction factor, the MWC efficiency correction, and determining the beam 'flux'.

First of all, any events recorded by the computer are counted (CNT2). Pulser events are then rejected and the number of non-pulser events are counted (CNPULS). Proton events are then selected by the particle identification window (SPID) of pulse height and time-of-flight values. The

number of proton events is counted (CPROT). 'Good' MWC events are then selected and the number of them counted (CMWOK). Finally, a 'window' is made on the solid angle by putting a restriction on the X0 and Y0 coordinates in the front-end chamber. These events are then divided into three bins as coming from three equally divided ranges of Y0 within the solid angle window so that data at three scattering angles separated by about one degree are extracted simultaneously. Events corresponding to each angle bin are then put into a spectrum according to their corrected focal plane position (XFK).

A typical focal plane spectrum (SXF) is shown in figure 4.8, the oxygen elastic peak stands between XFK channel 16000 to 17000 and is in general 'clean' and clear from the carbon elastic peak at channel 17000 to 18000 in this instance. At some angles, however, the carbon peak does get very close to the oxygen elastic peak (e.g. at 32° at 300 MeV in figure 4.9). Nevertheless, within the angular range of our data, the situation is tolerable.

Thirty-eight 'scalers' are accumulated as data are being taken in each run. Of particular interest to us are the scalers numbered 33 to 38. These are respectively,

scaler 33 : left polarimeter counts
scaler 34 : right polarimeter counts
scaler 35 : left accidental polarimeter counts
scaler 36 : right accidental polarimeter counts

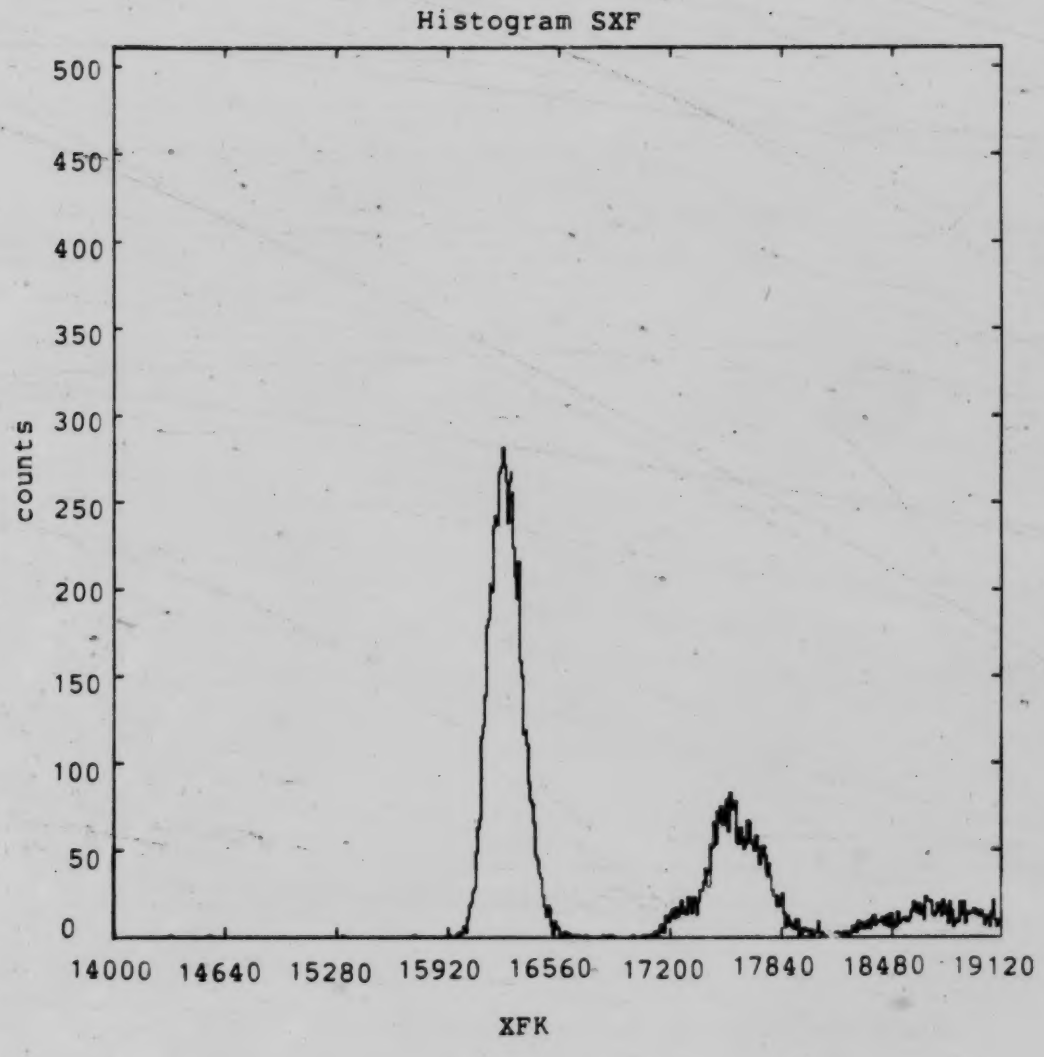

Figure 4.8 An SXF spectrum showing a clean oxygen elastic peak.

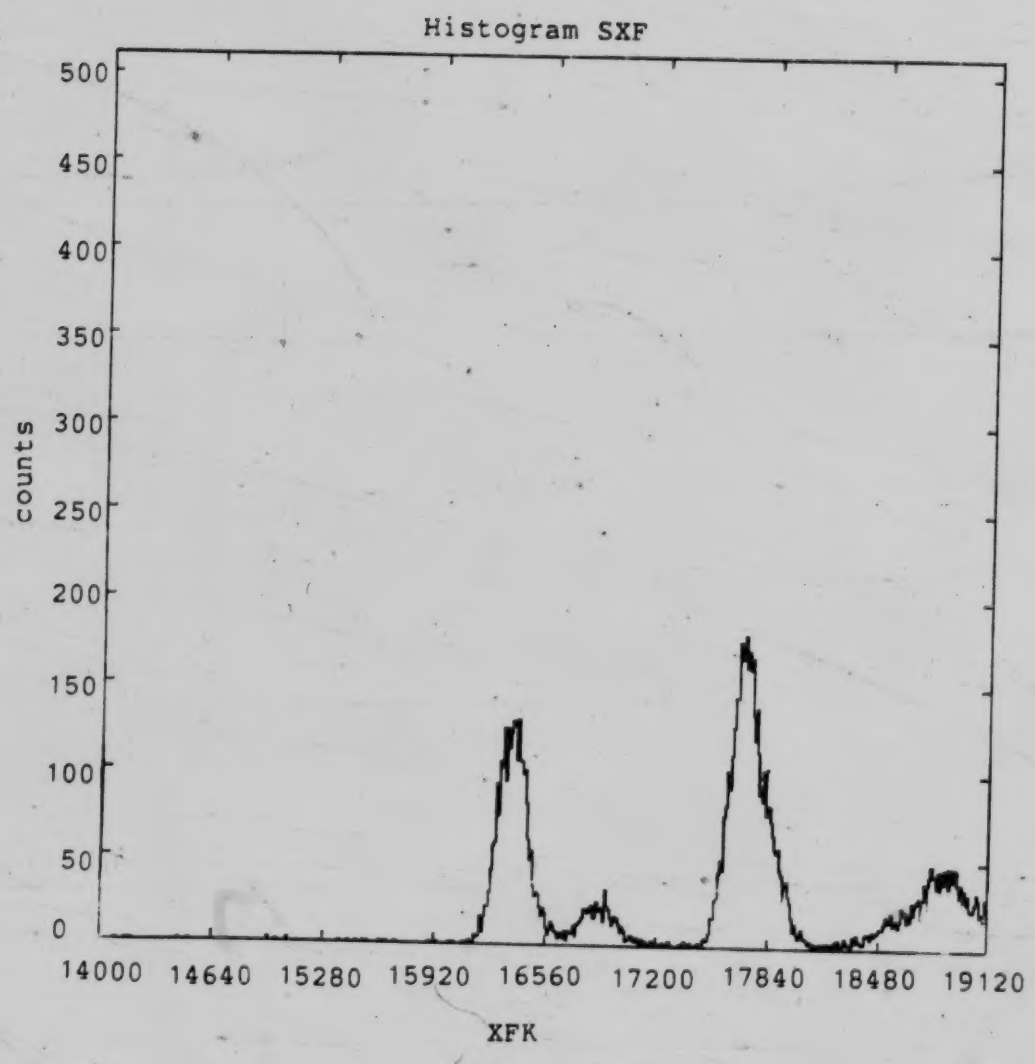

Figure 4.9 An SXF spectrum showing the carbon elastic peak close to the oxygen elastic peak.

scaler 37 : SEM accumulated charge

scaler 38 : number of pulsers presented to the computer.

The *live-time* of the computer (during data taking) is calculated as the ratio of the number of pulser events recorded by the computer to the number presented to it. The number of pulser events recorded is given by CNT2 minus CNPULS so that the deadtime correction factor (DTFACT) is calculated as

$$\text{DTFACT} = (\text{scaler 38})/(\text{CNT2} - \text{CNPULS}). \tag{4.2}$$

The MWC correction factor (MWCOR) is just the ratio of the number of protons determined by SPID to the number of 'good' events (CMWOK), thus

$$\text{MWCOR} = \text{CPROT}/\text{CMWOK} \tag{4.3}$$

as has already been stated in an earlier chapter.

The total incident beam charge is calculated as the polarimeter counts (minus the accidentals) divided by the count-to-charge conversion factor (CPNC),

$$\text{CHARGE} = (\text{scaler 33} + \text{scaler 34} - \text{scaler 35} - \text{scaler 36})/\text{CNPC} . \tag{4.4}$$

The total number of incident protons is then simply the CHARGE divided by the proton charge.

Finally, the differential cross section is given by

$$\frac{d\sigma}{d\Omega} = [(\text{counts in elastic peak}) \cdot (\text{deadtime correction}) \cdot (\text{MWC correction})] \; / \; [(\#\ \text{incident protons}) \cdot (\#\ \text{target nuclei per unit area}) \times (\text{solid angle})] \; . \tag{4.5}$$

4.6 Results of Data Analysis

There were two previous running periods on the elastic scattering of protons from oxygen before the July,1984 run. These occured in July'81 and April'82. Data from these runs will be referred as the 'old' data. The 'old' data had normalization problems in the differential cross sections in overlap regions of different runs. These are plotted in figure 4.10 to 4.13. A summary of the old data before re-normalization is given in appendix (2).

The major purpose of the present experiment was to solve the normalization problem in the previous experiments. Since analyzing power is not affected by normalization, the 'old' analyzing power data are believed to be valid. Consequently, we did not need, nor did we take, polarization data during the July,1984 run. The 'old' analyzing power data are given in appendix (3).

A summary of the angular range of the 'old' and 'new' data at each energy is given in table 4.7. Although smaller angle data were taken at 500 MeV with the Small Angle Configuration, we encountered technical difficulties with

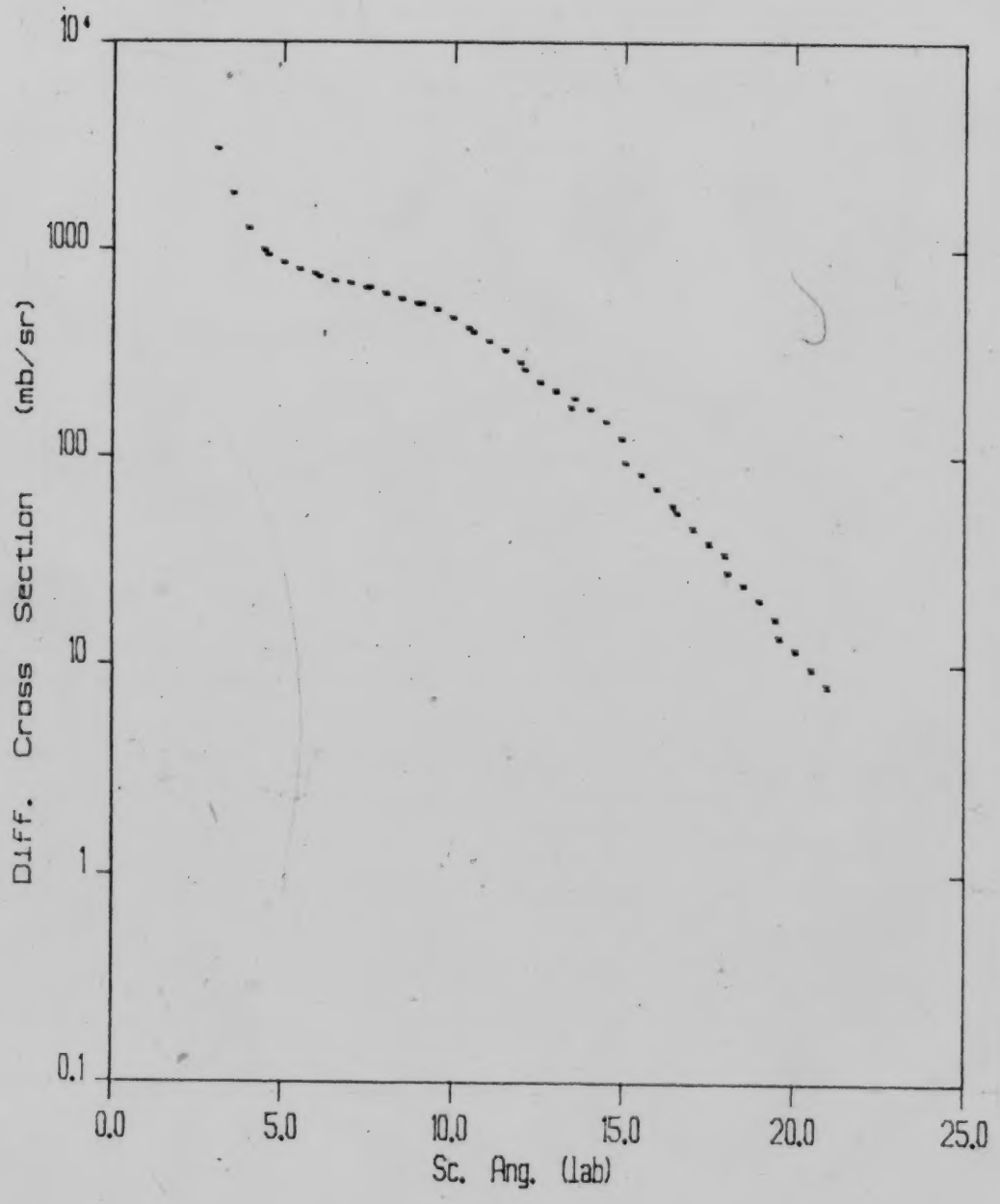

Figure 4.10 The differential cross section angular distribution of the 200 MeV 'old' data before re-normalization.

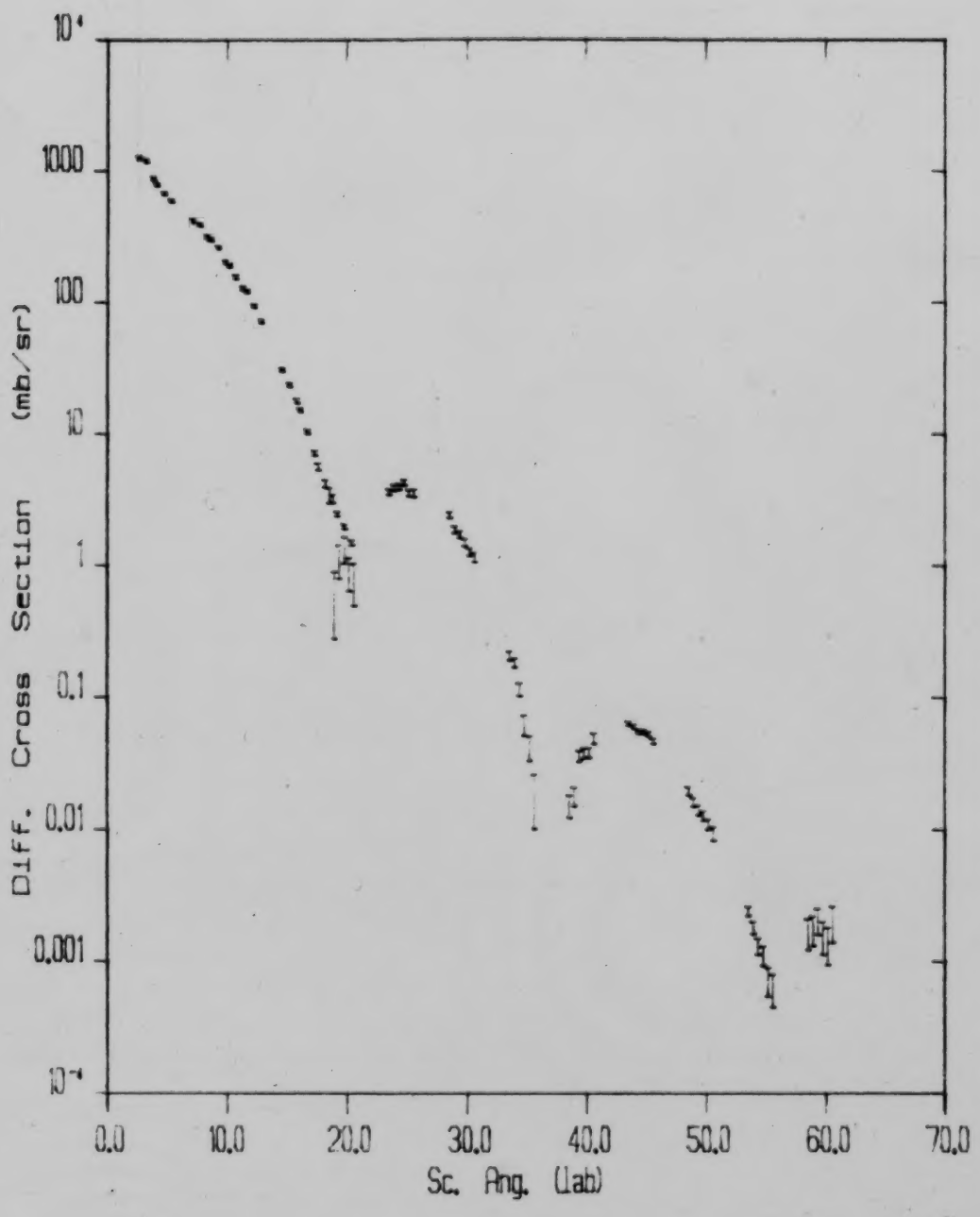

Figure 4.11 The differential cross section angular distribution of the 300 MeV 'old' data before re-normalization.

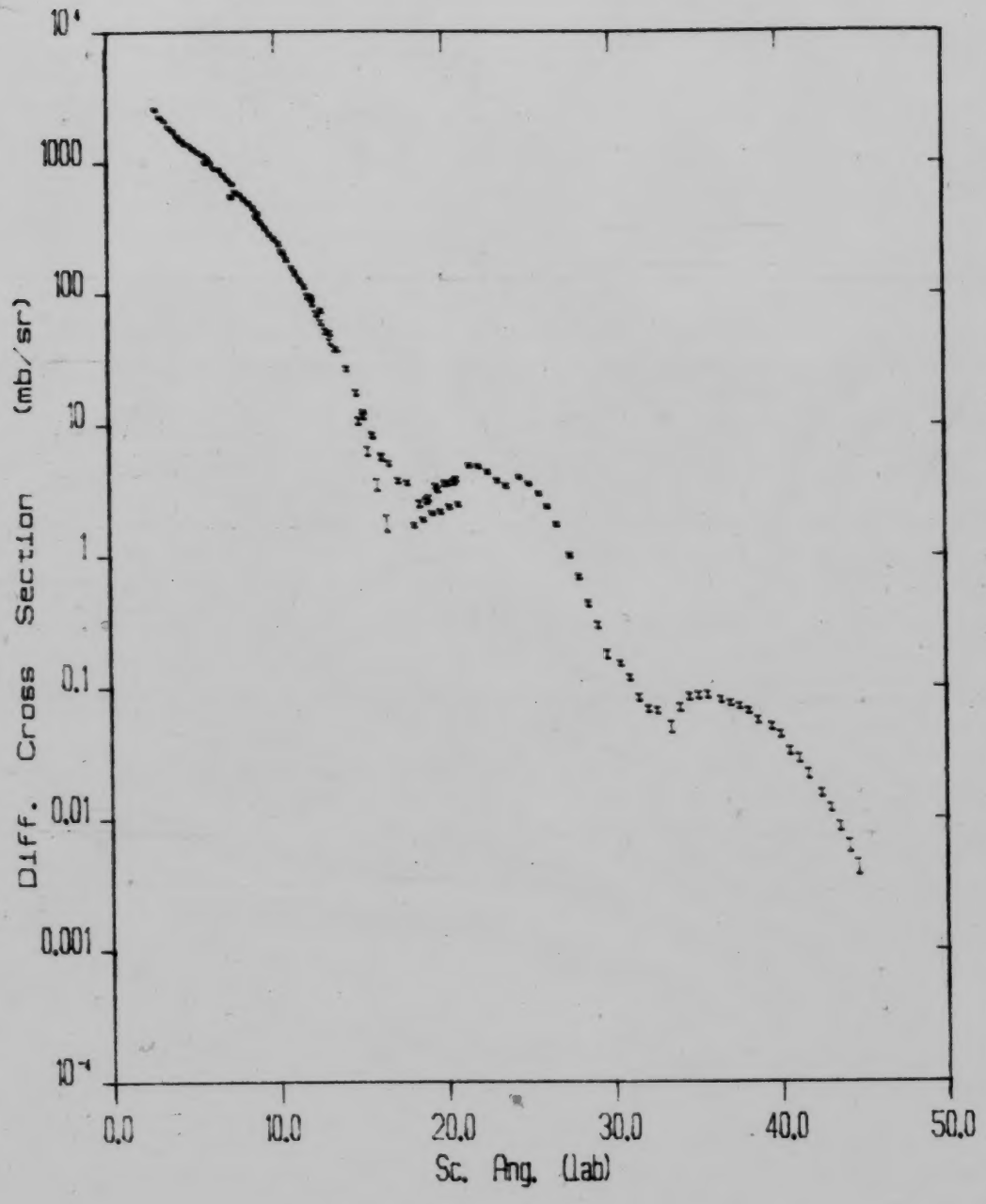

Figure 4.12 The differential cross section angular distribution of the 400 MeV 'old' data before re-normalization.

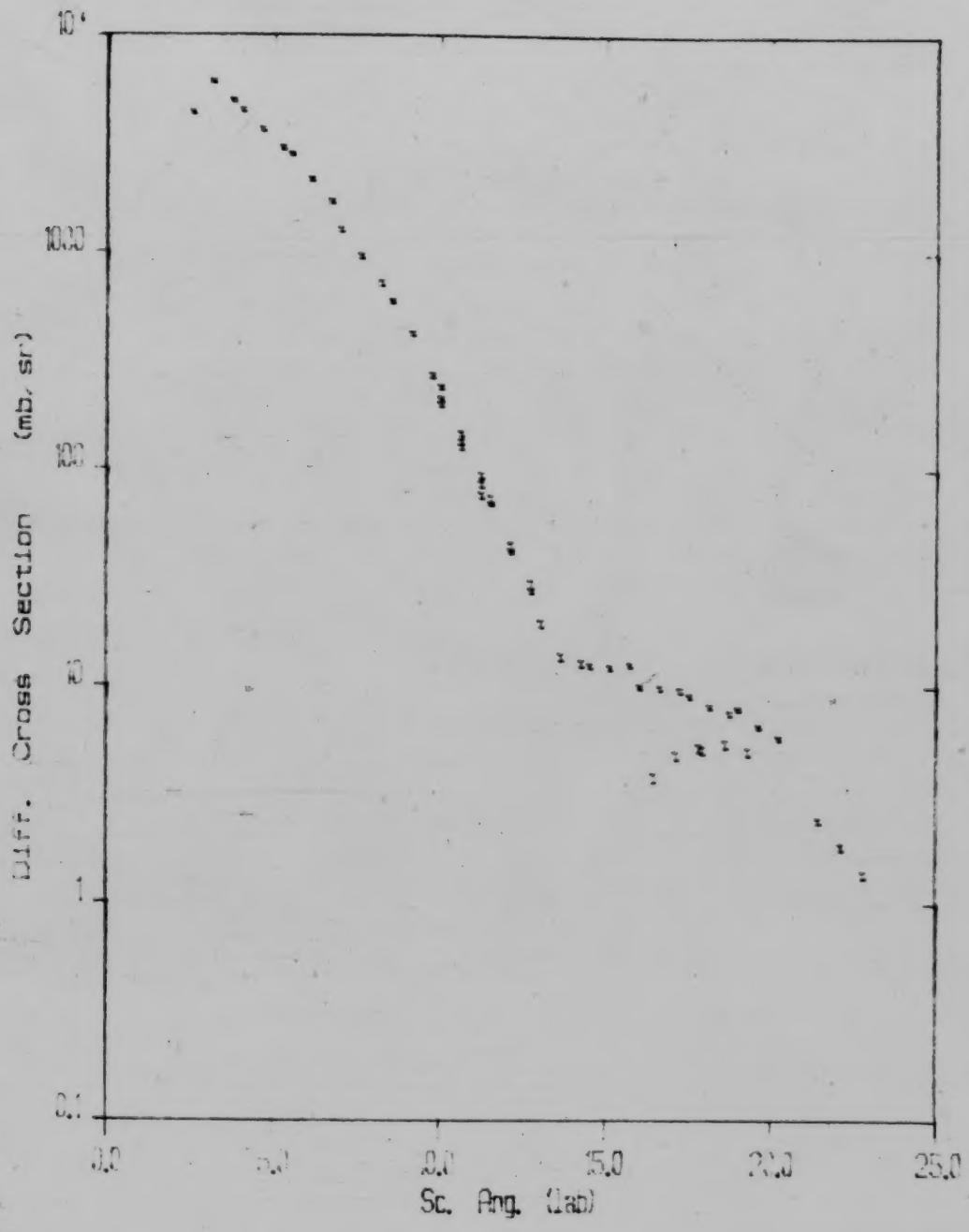

Figure 4.13 The differential cross section angular distribution of the 500 MeV 'old' data before re-normalization.

the front-end chamber. Therefore we decided afterwards to abandon the data taken in this configuration. The SAC 500 MeV data were therefore not analyzed.

The 'new' differential cross sections analyzed by the method outlined in previous sections are tabulated in appendix (1). Graphs of angular distributions at each energy are shown in figure 4.14 to 4.17 . The 'old' differential cross section data are renormalized according to the 'new' data. A total of one hundred ‘ differential cross section and analyzing power data points are randomly selected from the combined set of the 'new' and 'old' data to be used in the optical model analysis described in the next section. These are tabulated in appendix (4) and (5).

‘ *This is the maximum number allowed by the code MAGALI.*

Table 4.7 Table of angular range of data taken in July,1981, April,1982, and June,1984.

E(lab) Mev	Jul'81, Apr'82	June'84
200	2° - 21°	15° - 42°
300	2° - 61°	15° - 42°
400	3° - 45°	15° - 25°
500	3° - 20°	15° - 45°

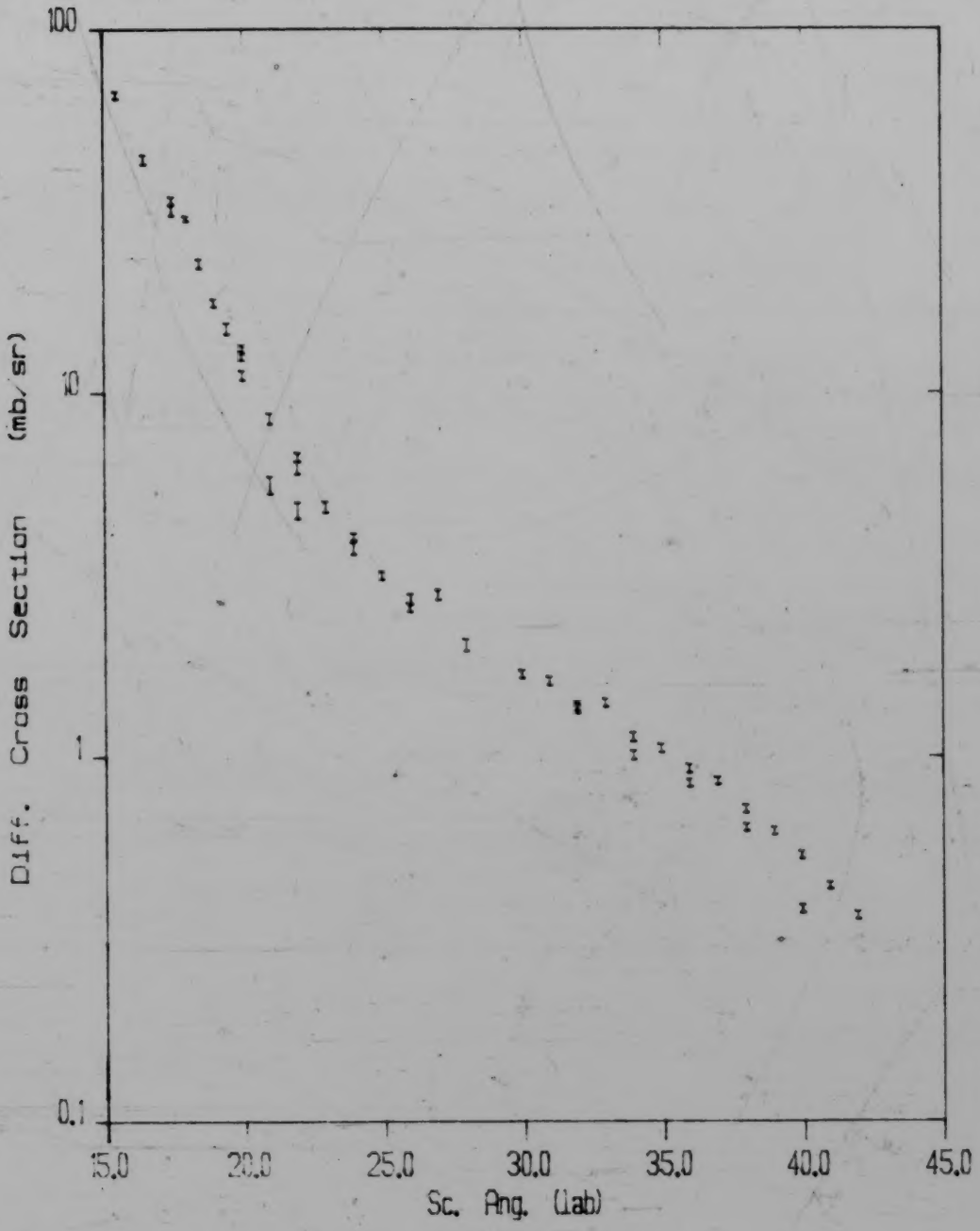

Figure 4.14 Differential cross section angular distribution of 'new' data at 200 MeV.

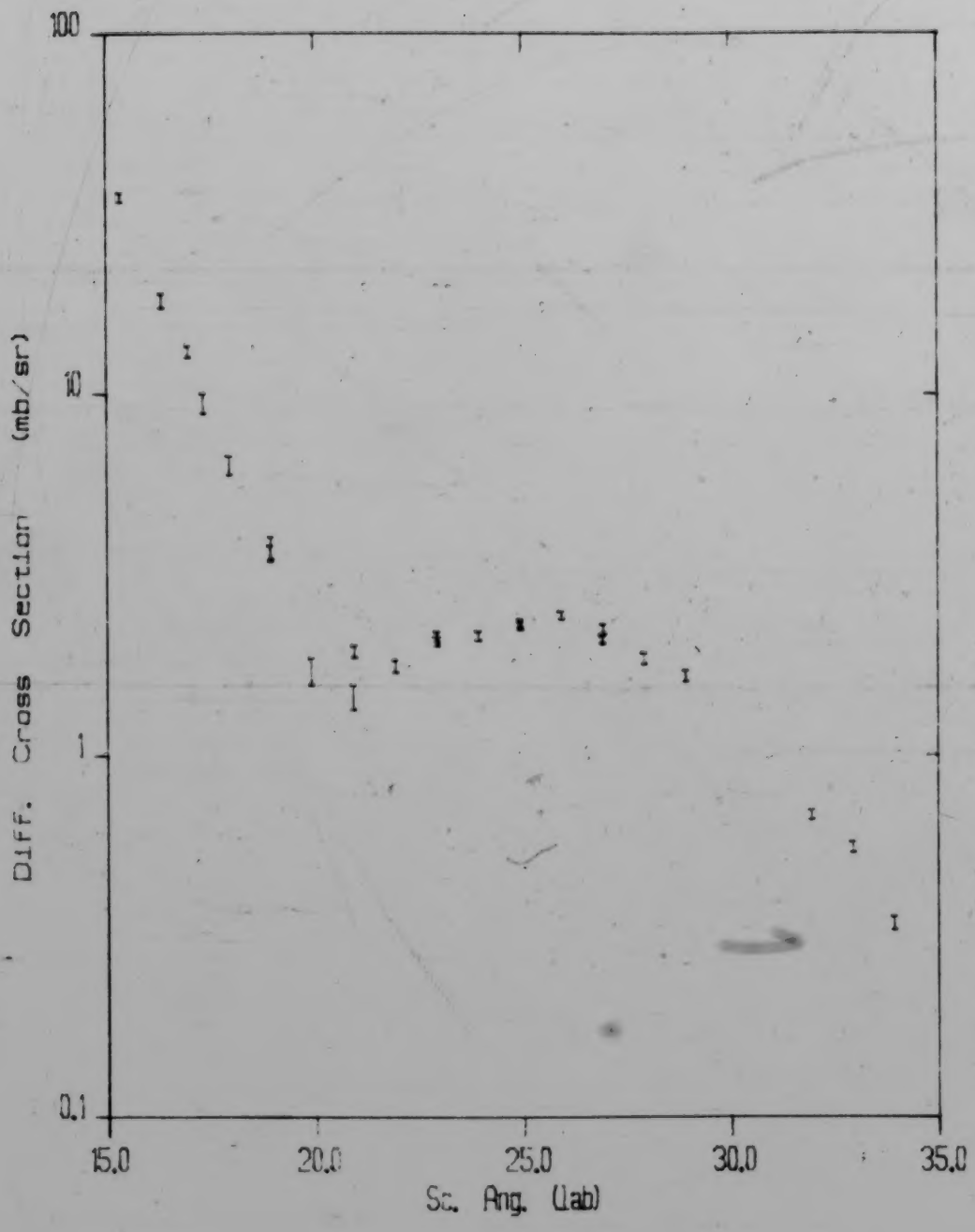

Figure 4.15 Differential cross section angular distribution of 'new' data at 300 MeV.

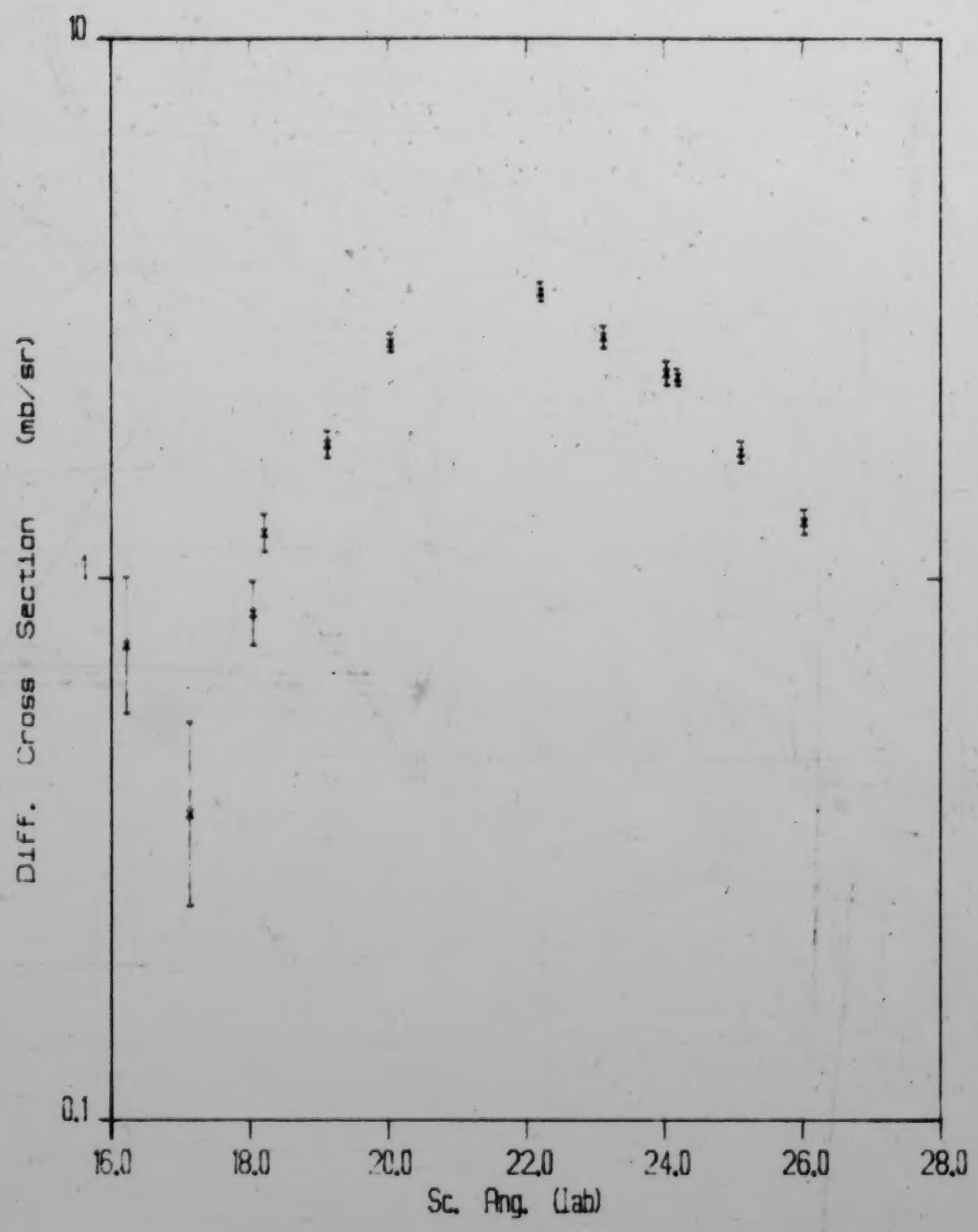

Figure 4.16 Differential cross section angular distribution of 'new' data at 400 MeV.

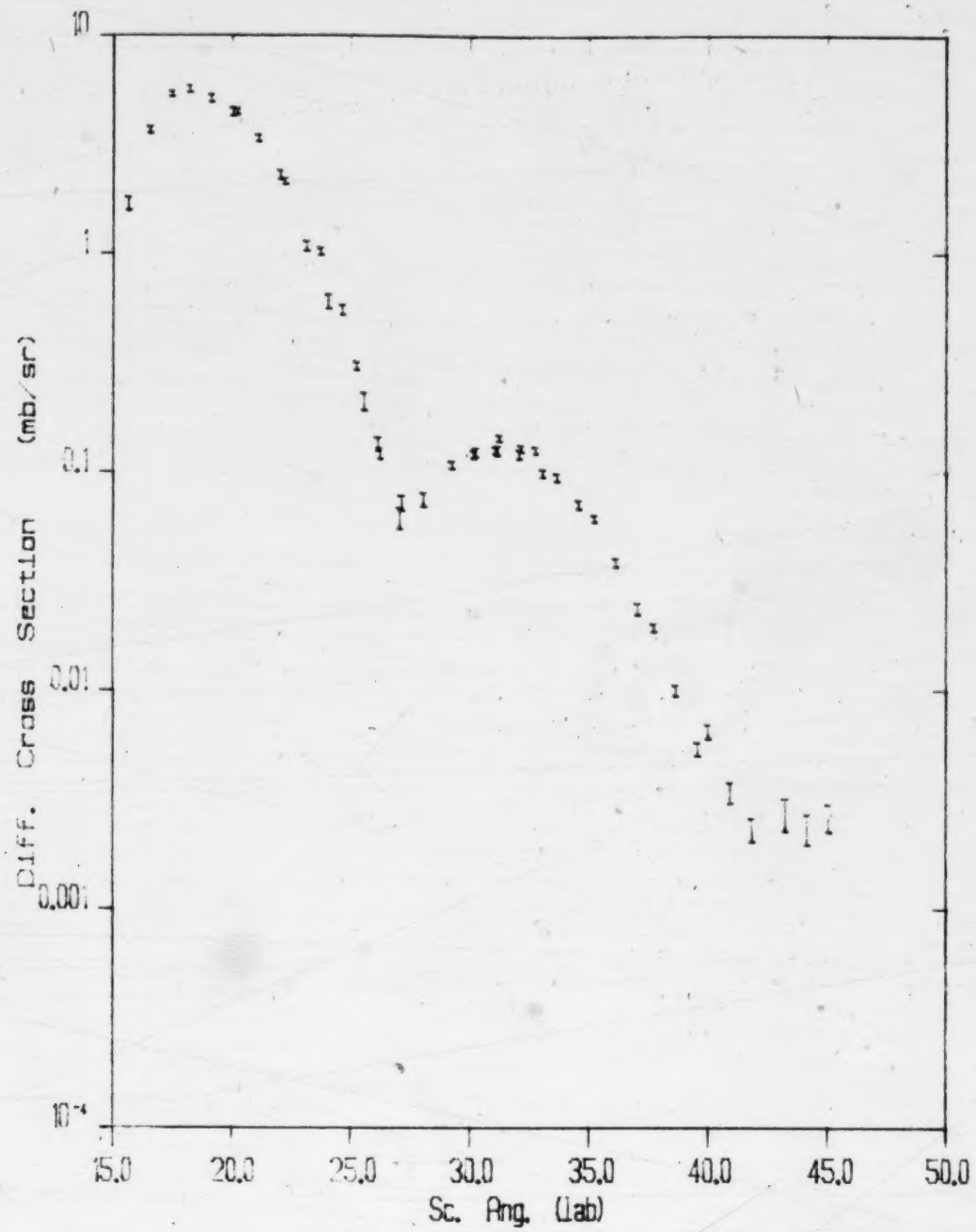

Figure 4.17 Differential cross section angular distribution of 'new' data at 508 MeV.

5. Optical Model Analysis

5.1 Non-relativistic Analysis Using The Standard Optical Model Code MAGALI

There have been indications (Glo 85, Arn 81) that the non-relativistic optical model parameterization using the simple Woods-Saxon form factors fails to fit experimental data in the 'transition energy' region between 200 and 500 MeV.

We tested fitting our data with the non-relativistic standard optical model code MAGALI (RAY 69). The parameterization is the standard one using the simple Woods-Saxon form factors:

$$U_{op} = V_{coul} + V_c F_c + i(W_c - 4W_D \frac{d}{dr})F_{ic}$$

$$+ (\hbar/m_\pi c)^2[V_{so} \frac{1}{r}\frac{d}{dr} F_{so} + W_{so} \frac{1}{r}\frac{d}{dr} F_{iso}] \underline{\sigma}\cdot\underline{l} \qquad (5.1)$$

where

$$F_x(r) = \{1 + \exp[(r-R_x)/a_x]\}^{-1}$$

are the simple Woods-Saxon form factors and

$$R_x = r_x A^{1/3} . \qquad (5.2)$$

The differential cross section in conjunction with the analyzing power data are analyzed at each energy to get the best total χ^2 fit

$$\chi^2 = \sum_i^n [(\text{model-expt})/\Delta\text{expt}]^2_{\sigma} + \sum_i^n [(\text{model-expt})/\Delta\text{expt}]^2_{Ay} . \quad (5.3)$$

5.2 Techniques of Search

Since there is considerable interplay between the parameters, there is usually more than one set of parameters which can give the same quality of fit to the data.

The criteria for choosing between different sets of parameters have been based on the physical meaning of the optical parameters. For example, it is an established fact that the real central potential should be increasingly repulsive towards higher energies. Therefore, this requirement must be met if the parameters are of any physical meaning at all. Furthermore, according to the folding model, the potential shapes should approximately follow the density distribution of the nucleus. Therefore, the radius parameter should be around 1.3 *fm* and the diffuseness parameter should be between 0.4 and 1.0 *fm*. Specifically, the diffuseness parameter should not be greater than the radius parameter.

When first starting a search, usually one cannot search on all parameters at once. It is useful to divide the parameters into three groups: the potential depths, the radius parameters, and the diffuseness parameters. If the radius and diffuseness (geometry) parameters are close to their 'true' values, one can start searching on the

potential depths first. Should one of the depths change sign contrary to the sign 'expected' for it, (usually the real spin-orbit potential,) then one should start instead with the radius or the diffuseness parameters.

Very often, one of the parameters in search tends to go away from the 'physical' range. In this case, that parameter can be fixed to a 'nominal' value while letting the rest of the group be searched.

When the χ^2's become 'steady' for each group of the parameters (possibily excluding one or two which tend to go out of range), combinations of parameters from different groups can be put in search. At this stage, one or more parameters may go 'wild', however, experience has shown that fixing one (the right one!) of them usually keeps the rest stable. This stage of the search is the most difficult, and time consuming. Considerable guess work is required in order to 'lead' the parameters close to their 'proper' values.

When at least nine of the parameters are stable and within their 'physical' range, all twelve parameters can be put in search. At this stage, the total χ^2 should be of the same order as the number of data to be fitted.

It will happen sometimes that at this final stage of the search one of the parameters 'drifts' away from the physical range. Should that happen, and should the total χ^2 be already small, the situation is very often impossible to fix: one might have to start over again.

5.3 Ambiguity of The Parameters

In our fitting process, we have found that the 200 and 300 MeV data are extremely difficult to fit. A possible explanation is perhaps that the simple Woods-Saxon form factors are not adequate at these two energies. One can imagine that the twelve parameters and the total χ^2 form a 13-dimensional manifold. If the form factors (geometry) are of the right shape, one can assume that there will be a deep, narrow minimum χ^2 in the manifold. In this case, the search would easily fall into the minimum.

On the other hand, if the geometry is of the wrong shape, then it is not inconceivable that a number of false minima will be present in the manifold. In this case, not only will the parameters be extremely unstable during the search, but also they will be ambiguous should these false minima be of the same order as the 'true' minimum.

Of course, there is also ambiguity in the parameters due to the limited number of data points available. It has been noted (Glo 85) that measurements up to large momentum transfers ($< 5\ fm^{-1}$) are needed to define the parameters unambiguously. In our experiment, we have only measured differential cross sections and analyzing powers to 50°, corresponding to a maximum momentum transfer of $\sim 3\ fm^{-1}$. Our data is therefore far from being a 'complete set', hence our parameters cannot be considered as 'precise'.

It has also been noted (Glo 85, Sch 83) that the spin-rotation function, $Q(\theta)$, is required in conjunction

with the differential cross section and analyzing power angular distributions to define the parameters accurately. We have not measured $Q(\theta)$ in our experiment, but such measurements would certainly be useful to further constrain the parameters especially at 200 and 300 MeV where the *shape transition* of the real central potential seems to be most noticable.

5.4 Results and Conclusions

We obtained good total χ^2 fits to the 400 and 500 MeV differential cross section and analyzing power angular distribution with the same Woods-Saxon radius and diffuseness parameters (geometry parameters). [5] However, we find that these parameters can not be applied to the 200 and 300 MeV data without sacrifice of good χ^2. With geometry parameters fixed to that for the 400 and 500 MeV cases, two potential parametrizations are found for the 300 MeV data. A close look at the parameters between these two alternative sets reveals that simply reversing the sign of the real central potential does not have any appreciable effect on the total χ^2. This probably indicates that attractive as well as repulsive contributions to the real central potential are equally important at this energy.

The one-geometry parametrizations are tabulated in table 5.1. The corresponding χ^2's are also given there. We see that the total χ^2 for the 200 and 300 MeV fits is about

---

[5] *The same set of geometry parameters were obtained in free search.*

Table 5.1 Table of one-geometry optical model parameterizations.

	E_{lab} (MeV)				
	200	300 (i)	300 (ii)	400	500
V_c	9.06	0.89	-0.88	5.19	10.41
r_c	1.11	1.11	1.11	1.11	1.11
a_c	0.64	0.64	0.64	0.64	0.64
W_c	-15.78	-15.17	-15.26	-24.20	-38.41
r_{ic}	1.13	1.13	1.13	1.13	1.13
a_{ic}	0.87	0.87	0.87	0.87	0.87
V_{so}	-3.17	-3.53	-3.51	-4.11	-3.84
r_{so}	1.11	1.11	1.11	1.11	1.11
a_{so}	0.57	0.57	0.57	0.57	0.57
W_{iso}	3.46	3.02	2.93	2.92	4.40
r_{iso}	1.17	1.17	1.17	1.17	1.17
a_{iso}	0.77	0.77	0.77	0.77	0.77
$\chi^2(\sigma)$	7770	1437	1261	324	247
χ^2(Ay)	29329	2301	2511	93	155
χ^2	37100	3738	3772	417	402

one order of magnitude higher than that for the 400 and 500 MeV fits. If we also require good χ^2 fits to the 200 and 300 MeV data comparable to that for the 400 and 500 MeV data, we have to allow the geometry parameters to differ from those of the 400 and 500 MeV fits. Two such parametrizations are found for each of the 200 and 300 MeV data sets. These are shown in table 5.2: the 400 and 500 MeV parametrizations are repeated in this table for completeness.

We note that the two parametrizations for the 200 MeV data are very similar, conforming to the possible 20% uncertainty intrinsic to the parameter ambiguity (Hod 63). Those for the 300 MeV data, however, differ considerably especially in the real central potentials. The fits to the experimental data according to the parametrizations given in table 5.2 are shown in figure 5.1 to 5.12. The radial distributions of the potentials are shown in figure 5.13 to 5.16. The volume integrals J_x of the potentials U_x are calculated by

$$J_x = \int U_x(r)\, dr \,. \tag{5.4}$$

These are tabulated in table 5.3.

In conclusion, we were able to fit the differential cross section and the analyzing power angular distribution at 200, 400 and 500 MeV energies using the standard optical model potentials. The 300 MeV parametrization using the simple Woods-Saxon form factors of the standard optical is ambiguous however. Moreover, the fit to the analyzing power

angular distribution data is relatively poor at this energy.

If we were to think in terms of the "wine-bottle-bottom" shape of the real central potential at the 'transition energy' region that has been borne out from theortical calculations, then we could conjecture that the relatively poor fit to the 300 MeV analyzing power angular distribution and the relatively large ambiguity of the parametrization at this energy are probably due to the increased importance of the interplay between the attractive and repulsive contributions to the real central potential at about 300 MeV for oxygen.

Table 5.2 Table of optical parameterizations with the geometry parameters in search for minimun χ^2.

	E_{lab} (MeV)					
	200 (i)	200 (ii)	300 (i)	300 (ii)	400	500
V_c	-11.52	-11.85	-9.264	1.49	5.19	10.41
r_c	1.33	1.33	1.29	1.13	1.11	1.11
a_c	0.67	0.67	0.76	0.56	0.64	0.64
W_c	-14.27	-13.24	-24.97	-15.30	-24.20	-38.41
r_{ic}	1.20	1.24	0.92	1.02	1.13	1.13
a_{ic}	0.75	0.73	0.83	0.75	0.87	0.87
V_{so}	-3.45	-3.22	-1.31	-2.79	-4.11	-3.84
r_{so}	1.03	1.03	1.12	1.17	1.11	1.11
a_{so}	0.51	0.49	0.72	0.54	0.57	0.57
W_{iso}	1.39	1.82	2.85	2.41	2.92	4.40
r_{iso}	1.25	1.15	0.73	0.87	1.17	1.17
a_{iso}	0.73	0.72	0.53	0.72	0.77	0.77
$\chi^2(\sigma)$	345	331	379	649	324	247
χ^2(Ay)	228	220	330	373	93	155
χ^2	573	551	709	1022	417	402

Table 5.3 Table of volume integrals (MeV-fm^3) of the optical model potentials using the parameters given in table 5.2

	E_{lab} (MeV)					
	200 (i)	200 (ii)	300 (i)	300 (ii)	400	500
U_c	-2543.57	-2605.51	-2068.41	199.13	721.90	1447.97
W_c	-2623.71	-2603.90	-2950.78	-2007.07	-4503.03	-7147.16
U_{so}	-351.23	-318.82	-199.85	-398.68	-531.83	-496.36
W_{so}	280.07	298.75	377.33	220.61	524.83	790.83

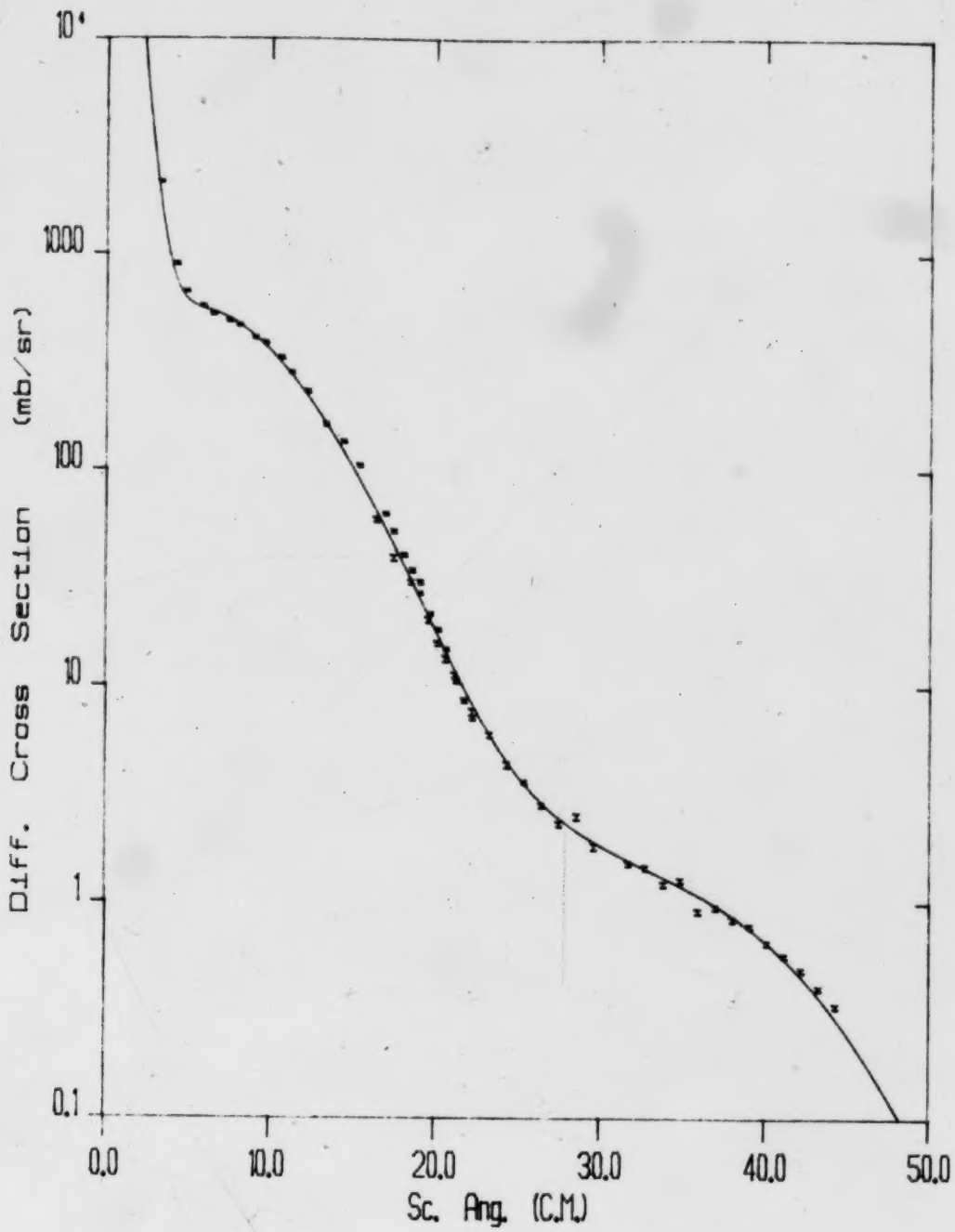

Figure 5.1 Non-relativistic standard optical model fit to the differential cross section angular distribution at 200 MeV using the parametrization (i) in table 5.2.

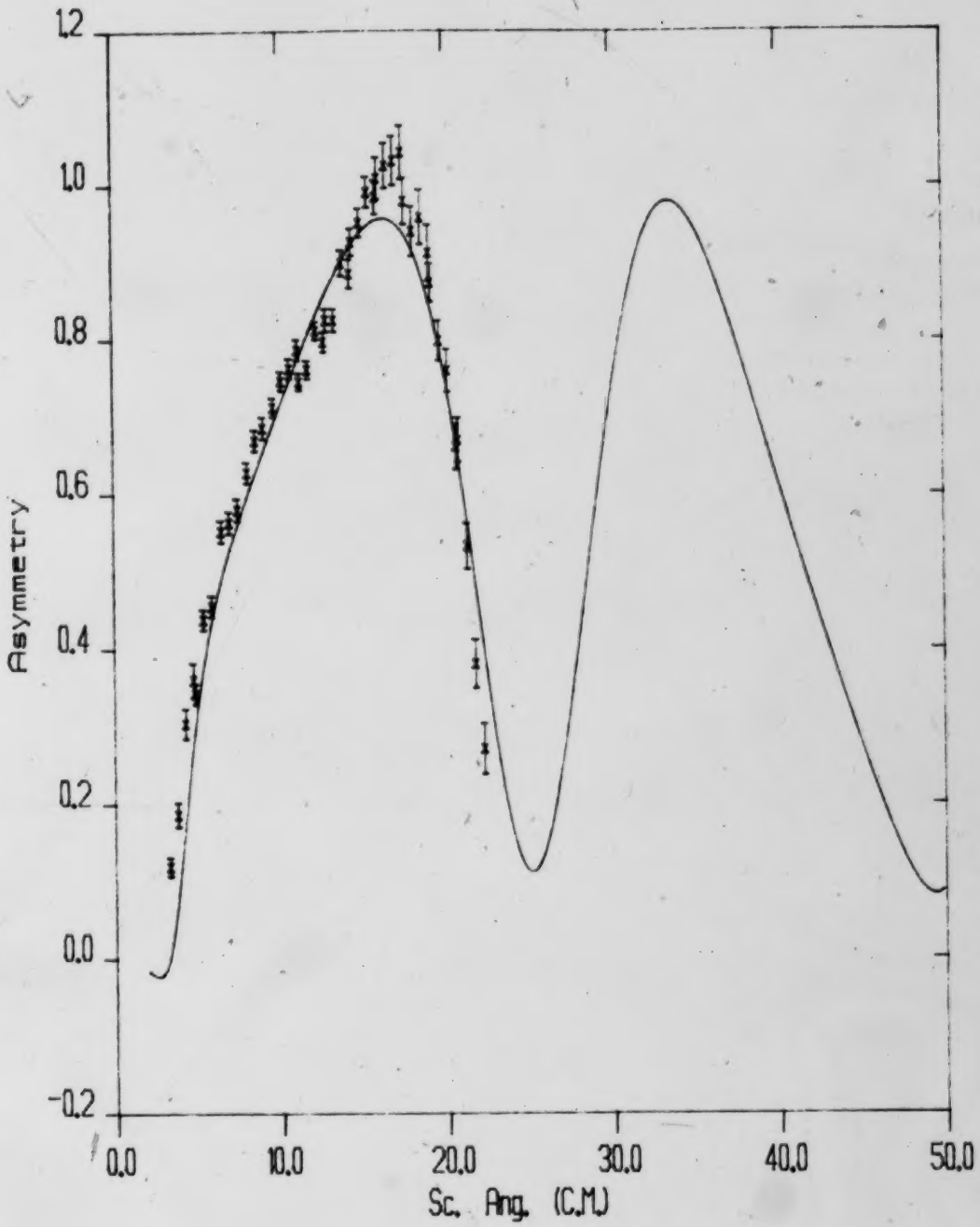

Figure 5.2 Non-relativistic standard optical model fit to the analyzing power angular distribution at 200 MeV using the parametrization (i) in table 5.2 .

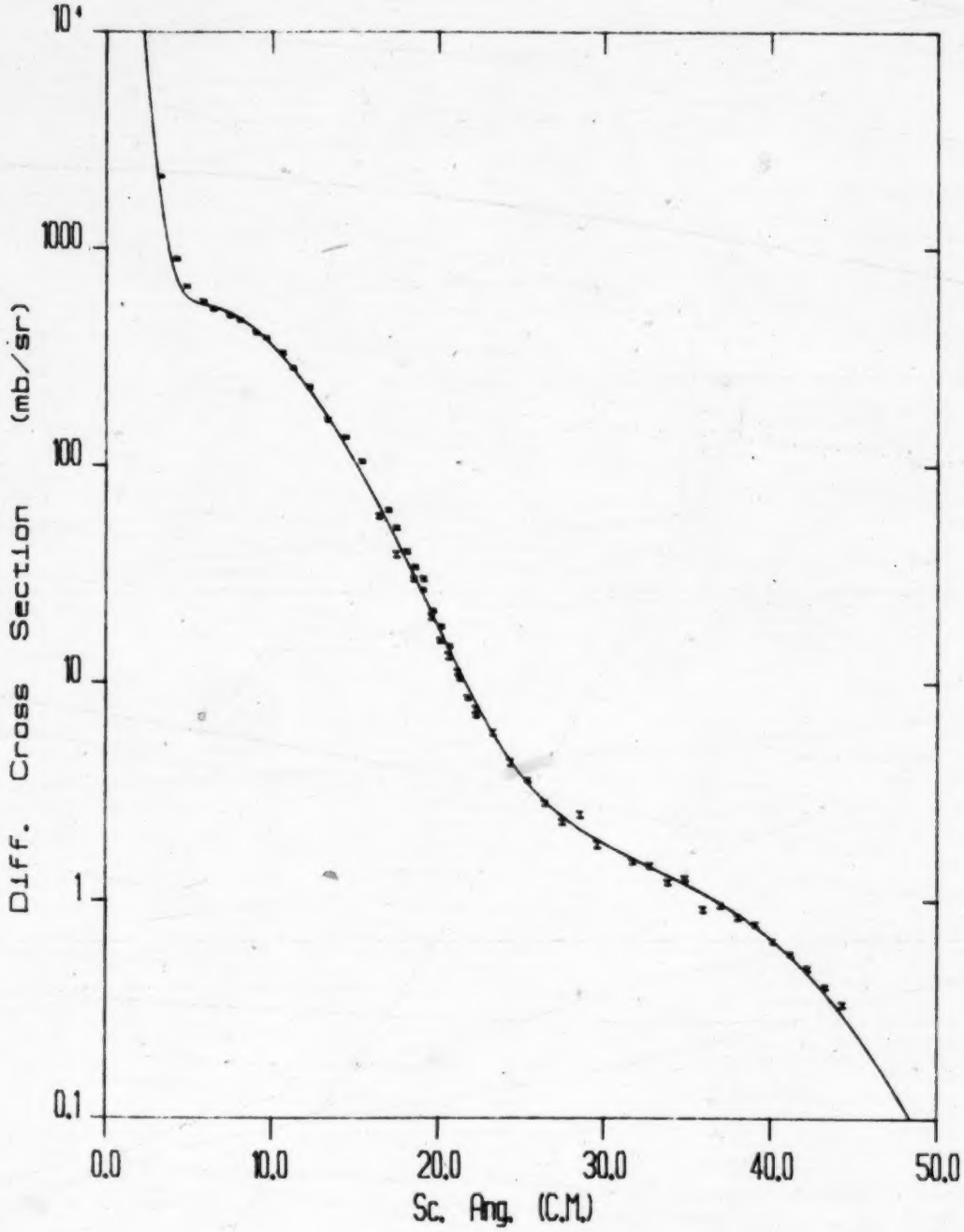

Figure 5.3 Non-relativistic standard optical model fit to the differential cross section angular distribution at 200 MeV using the parametrization (ii) in table 5.2 .

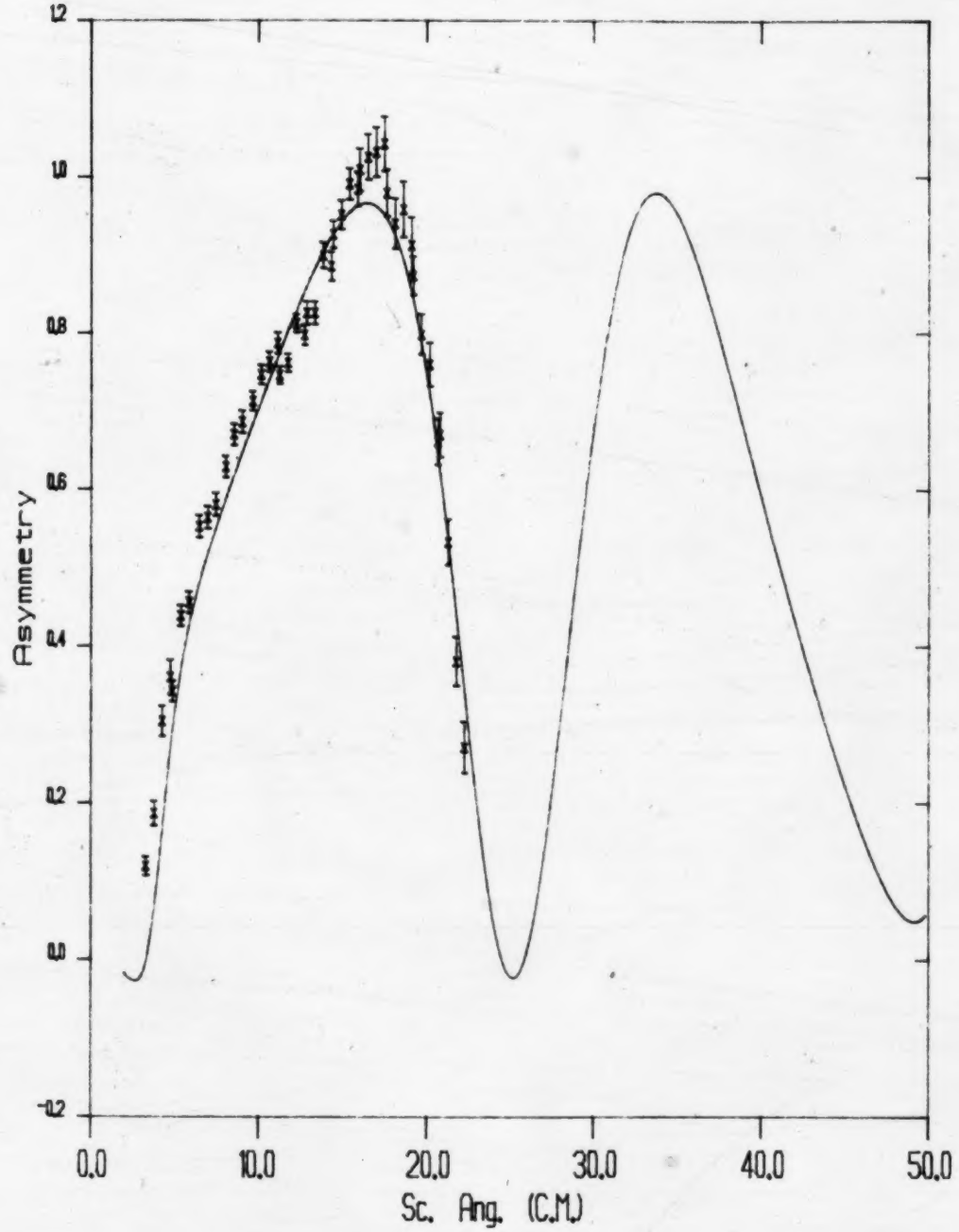

Figure 5.4 Non-relativistic standard optical model fit to the analyzing power angular distribution at 200 MeV using the parametrization (ii) in table 5.2 .

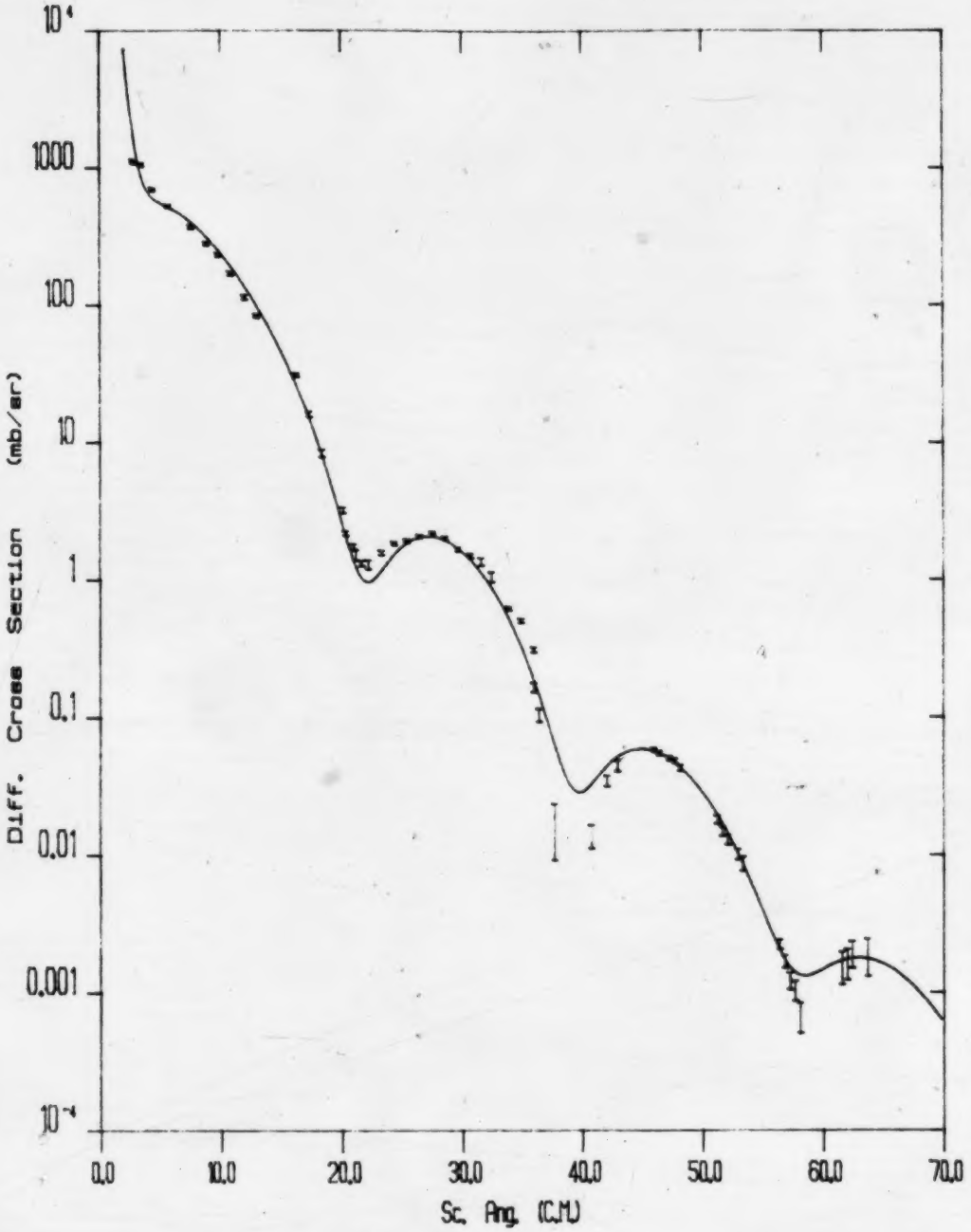

Figure 5.5 Non-relativistic standard optical model fit to the differential cross section angular distribution at 300 MeV using the parametrization (i) in table 5.2 .

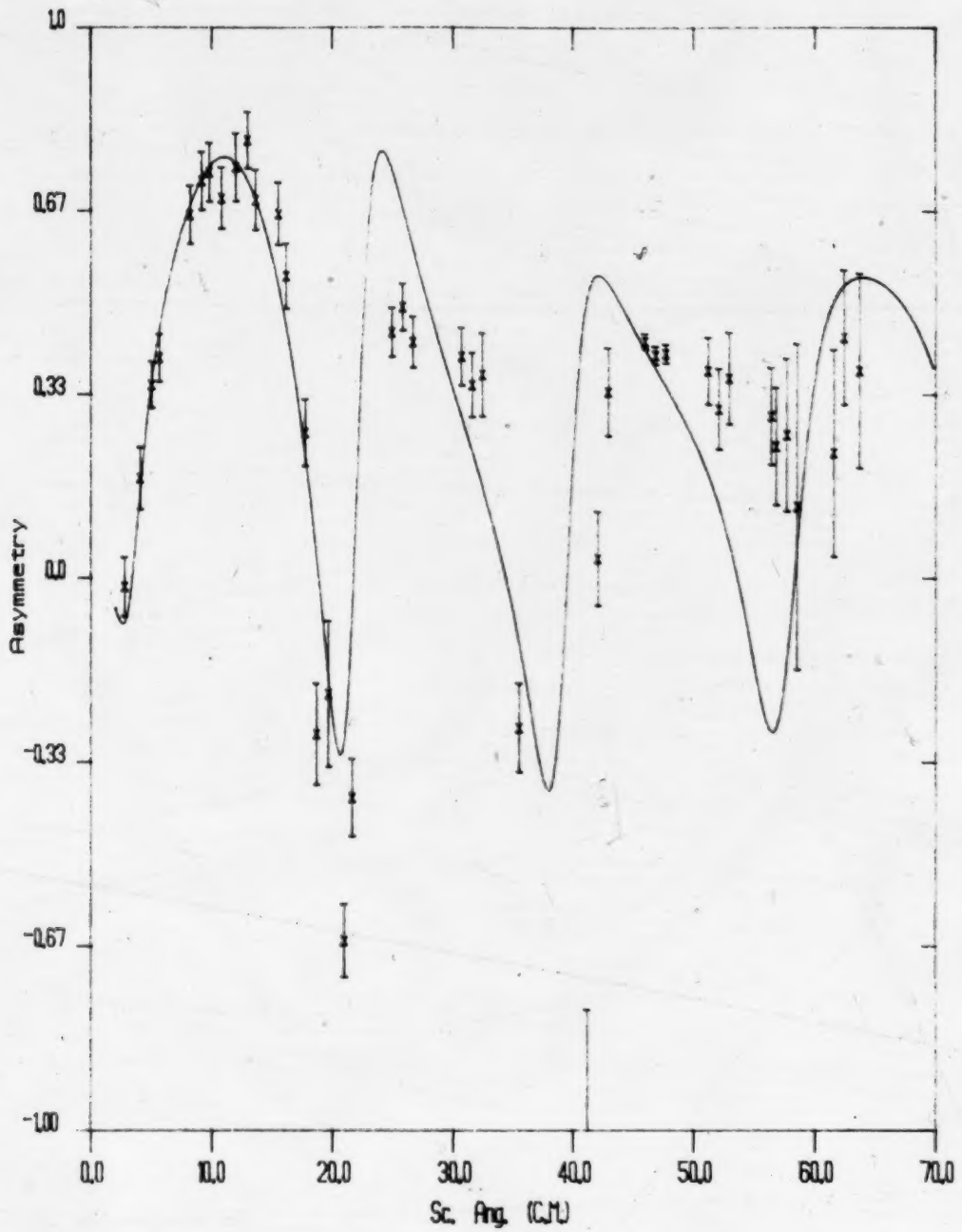

Figure 5.6 Non-relativistic standard optical model fit to the analyzing power angular distribution at 300 MeV using the parametrization (i) in table 5.2 .

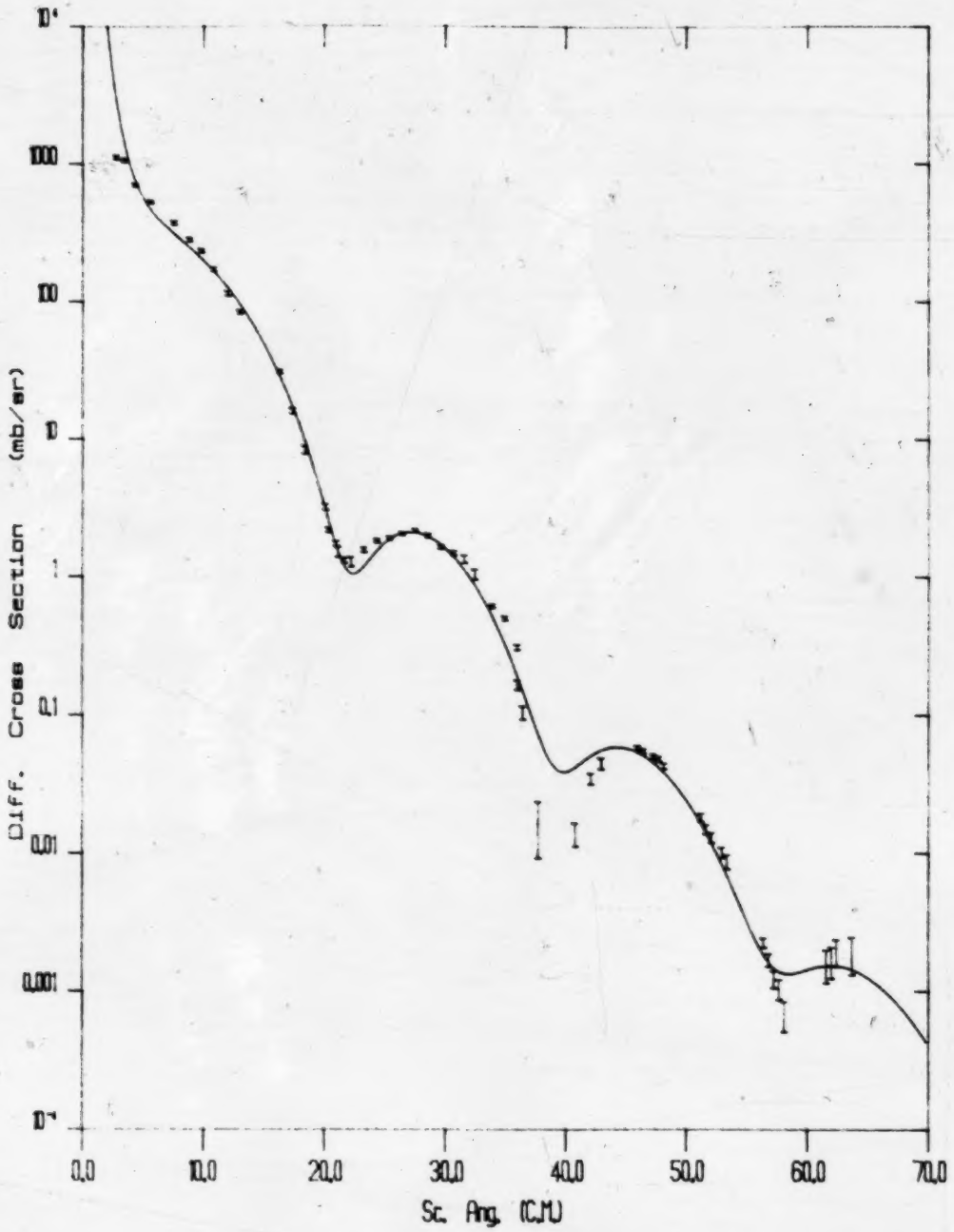

Figure 5.7 Non-relativistic standard optical model fit to the differential cross section angular distribution at 300 MeV using the parametrization (ii) in table 5.2 .

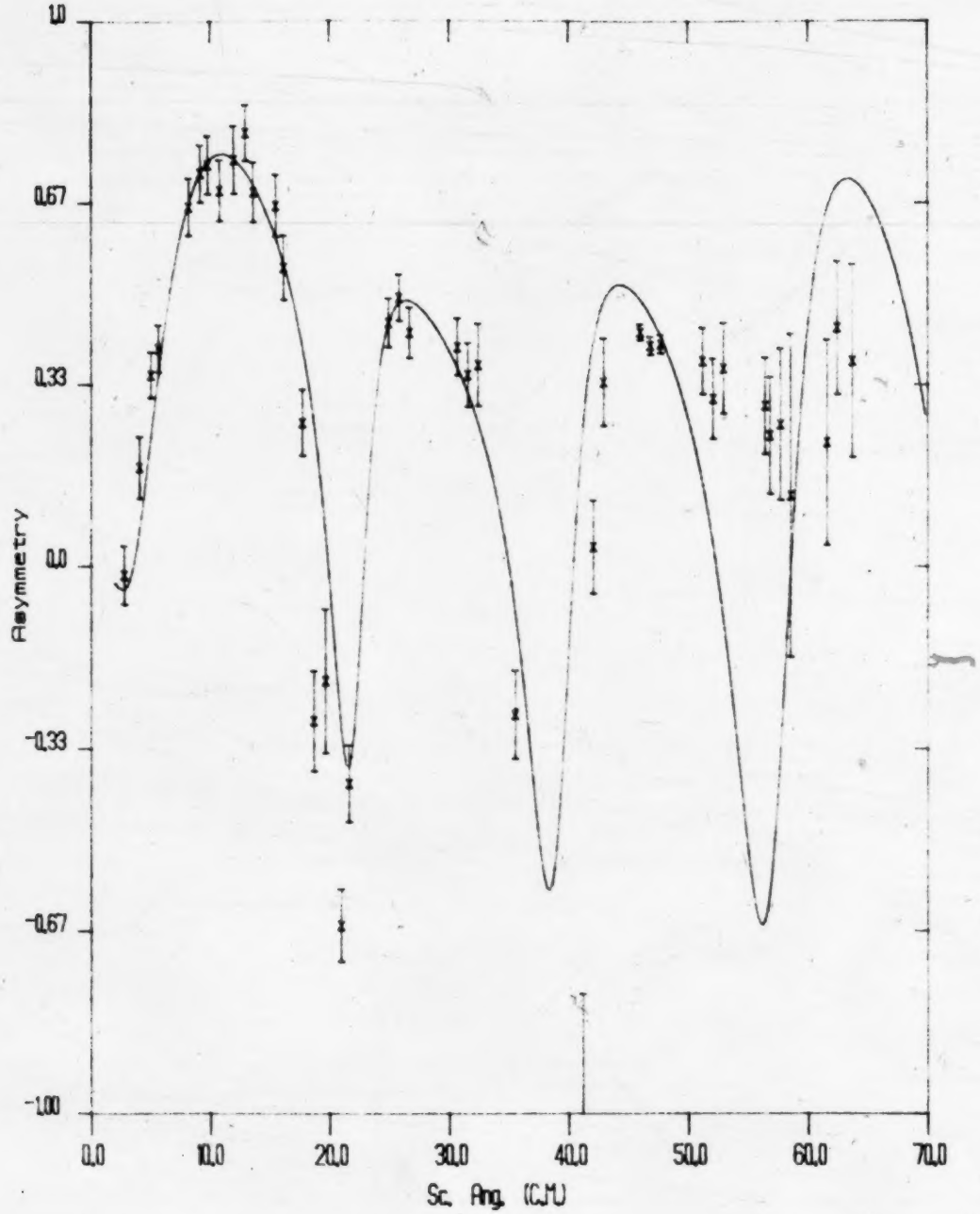

Figure 5.8 Non-relativistic standard optical model fit to the analyzing power angular distribution at 300 MeV using the parametrization (ii) in table 5.2 .

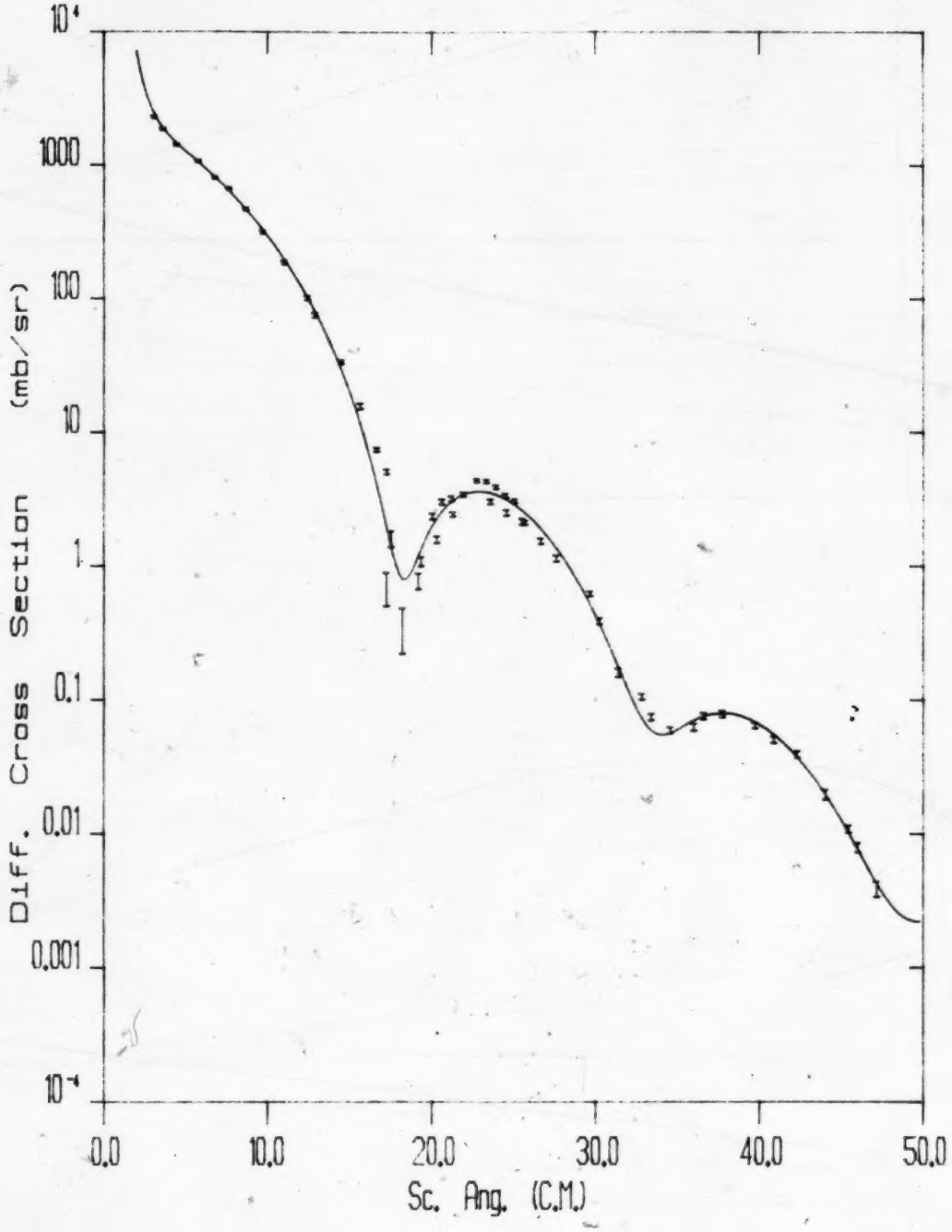

Figure 5.9 Non-relativistic standard optical model fit to the differential cross section angular distribution at 400 MeV using the parametrization given in table 5.2 .

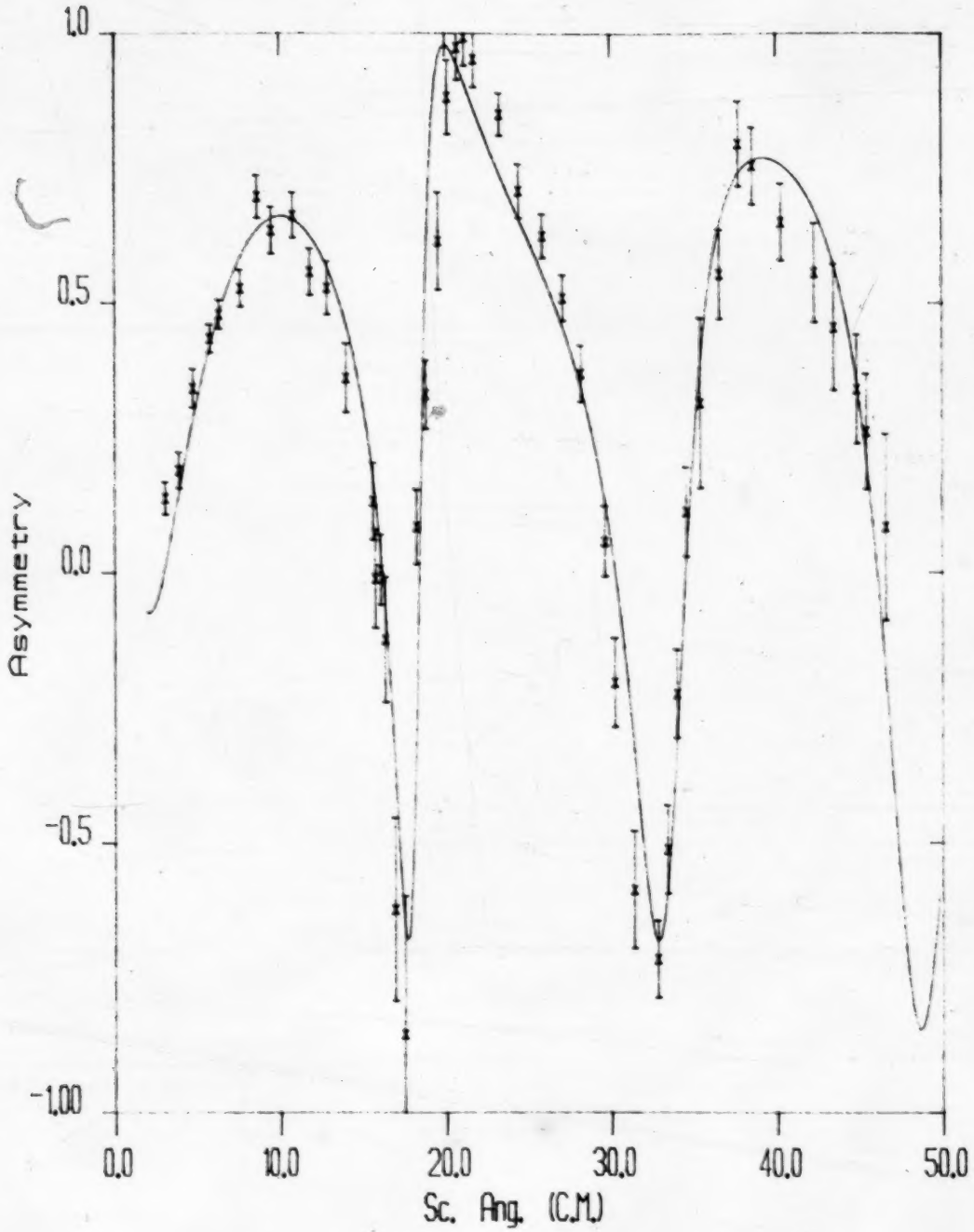

Figure 5.10 Non-relativistic standard optical model fit to the analyzing power angular distribution at 400 MeV using the parametrization given in table 5.2 .

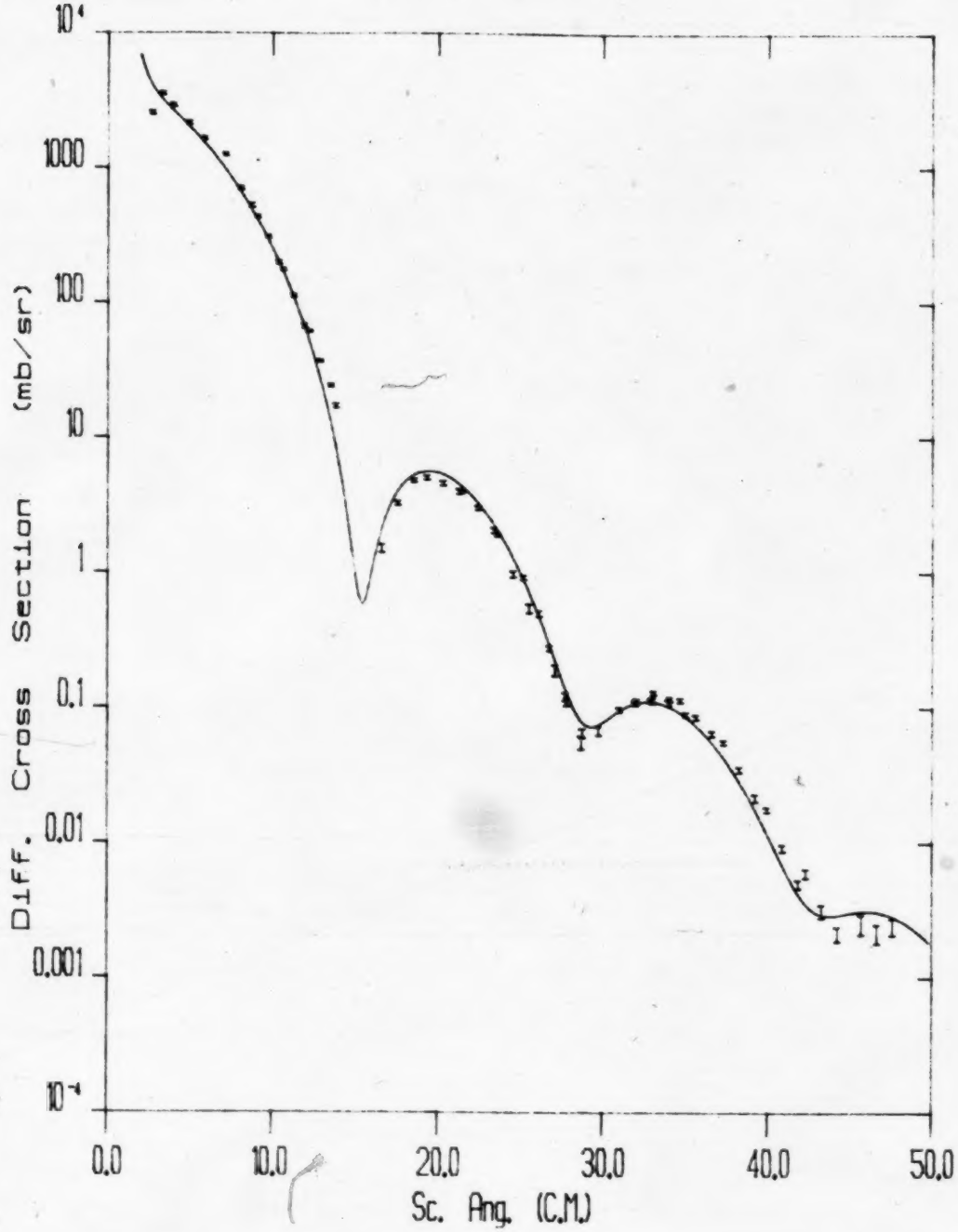

Figure 5.11 Non-relativistic standard optical model fit to the differential cross section angular distribution at 500 MeV using the parametrization given in table 5.2 .

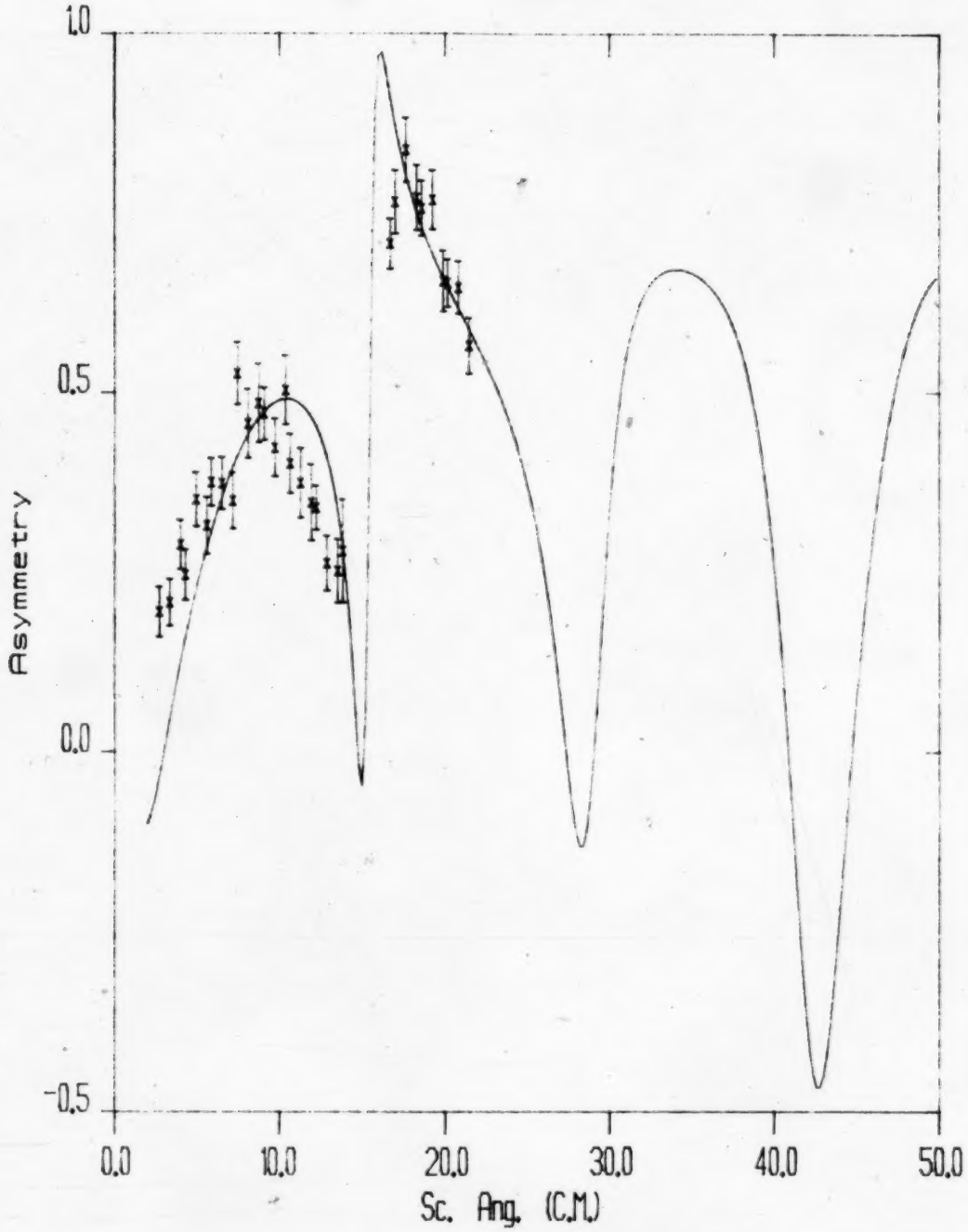

Figure 5.12 Non-relativistic standard optical model fit to the analyzing power angular distribution at 500 MeV using the parametrization given in table table 5.2 .

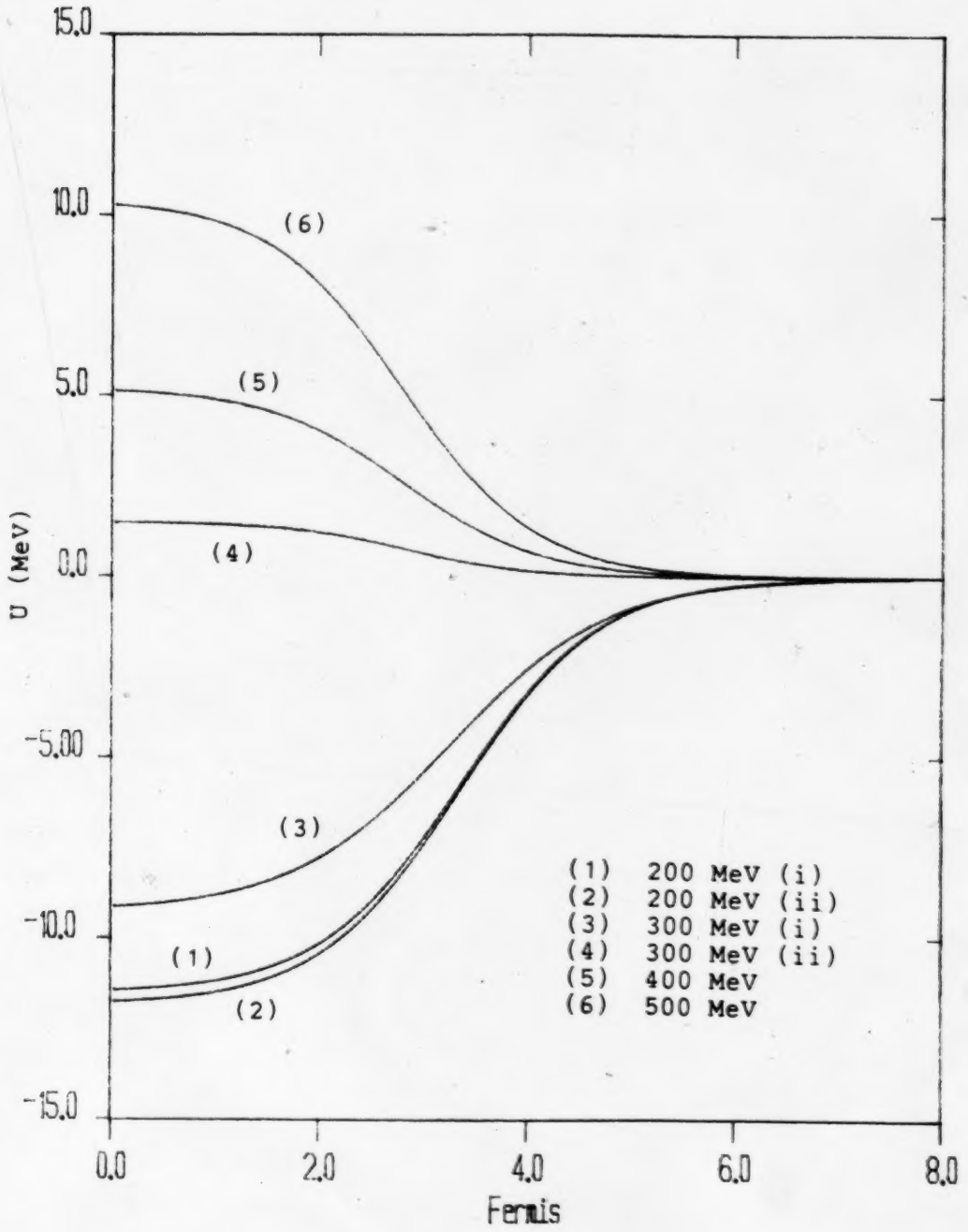

Figure 5.13 Radial distributions of the real central potentials according to the parameters given in table 5.2.

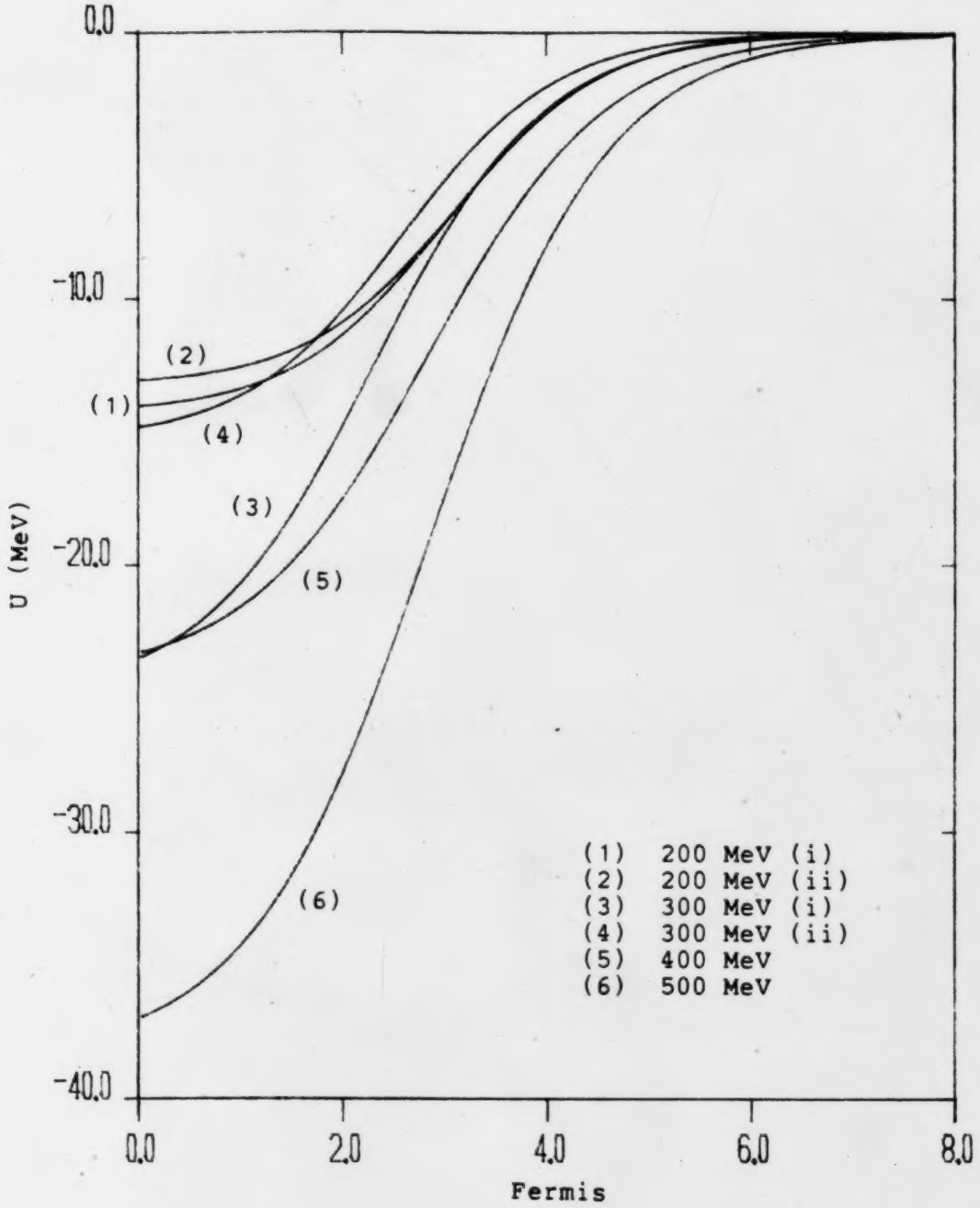

Figure 5.14 Radial distributions of the imaginary central potentials according to the parameters given in table 5.2.

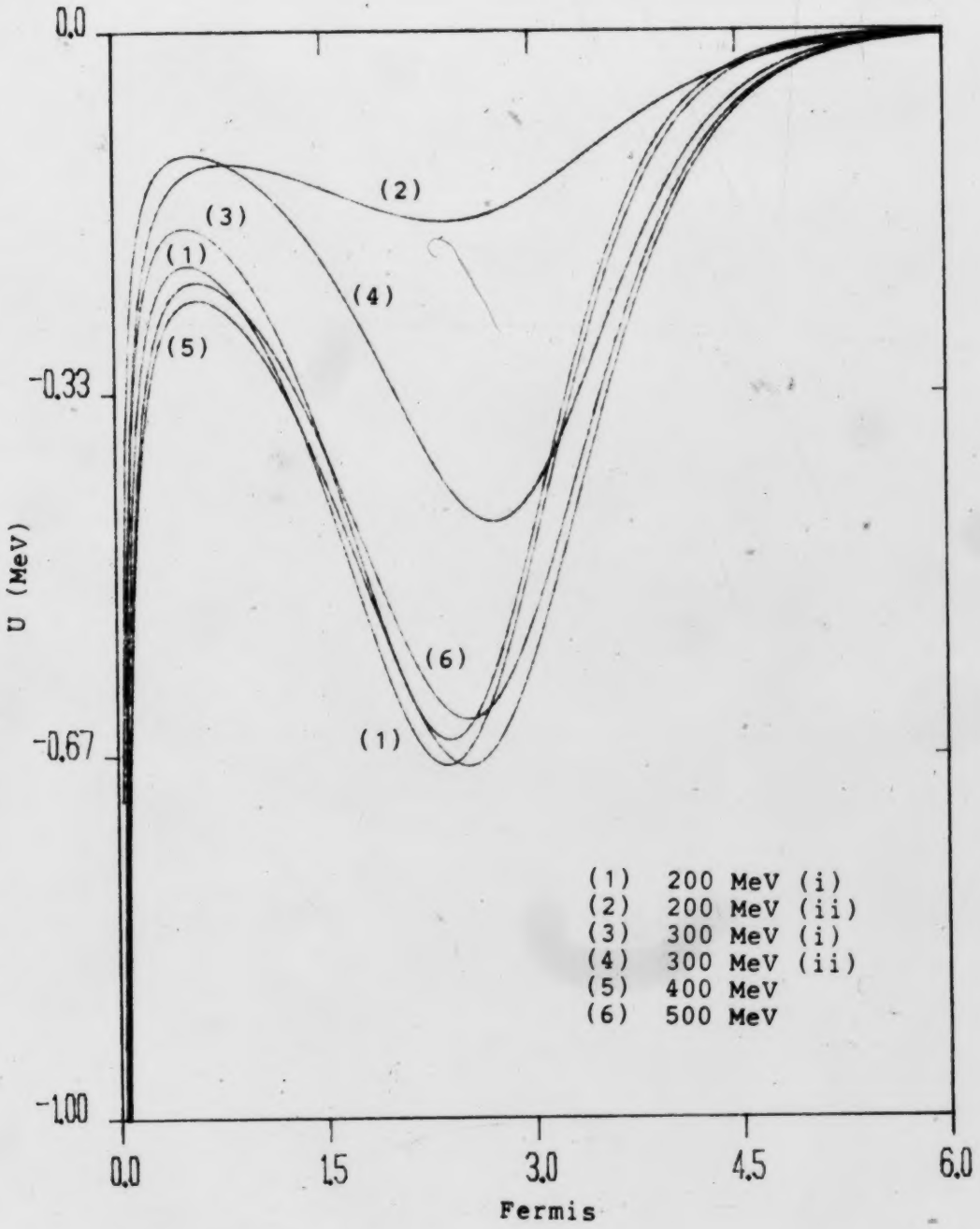

Figure 5.15 Radial distributions of the real spin-orbit potentials according to the parameters given in table 5.2.

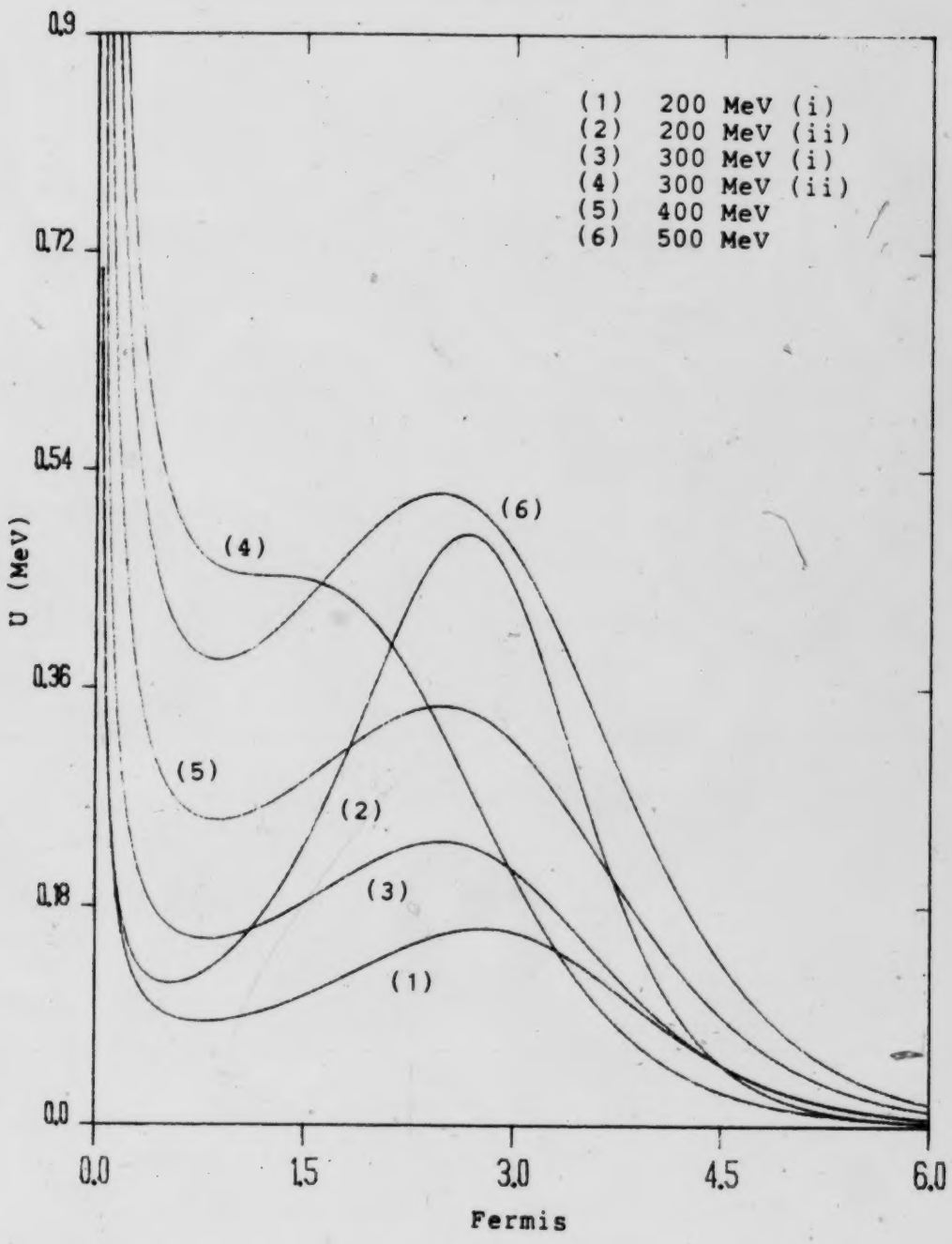

Figure 5.16 Radial distributions of the imaginary spin-orbit potentials according to the parameters given in table 5.2.

Bibliography

P.E. Hodgson, **The Optical Model Of Elastic Scattering**, Oxford University Press (1963).

D.F. Jackson, **Nuclear Reactions**, Methuen (1970).

The Interaction Between Medium Energy Nucleon In Nuclei - 1982 (Indiana University Cyclotron Facility), ed. H.O. Meyer, AIP Conference Proceedings No.97, American Institute Of Physics (1983).

A.L. Fetter and K.M. Watson, *The Optical Model* in **Advances In Theoretical Physics**, ed. K.A. Brueckner, vol. 1, Academic Press (1965).

M.A. Preston, **Physics Of The Nucleus**, Addison-Wesley (1962).

Microscopic Optical Potentials, Proceedings of the Hamburg Topical Workshop on Nuclear Physics, Held at the University of Hamburg, Hamburg, Germary, September 25-27, 1978, ed. H.V. Geramb, Springer-Verlag (1979).

References

(ALN 81) L.G. Arnold et al, Phys. Rev. C23,1949(1981).

(ALN 82) L.G. Arnold et al; Phys. Rev. C25,936(1982).

(BRI 77) F.A. Brieva and J.R. Rook, Nucl. Phys. A291,299(1977); A291,317(1977).

(ELT 66) L.R.B. Elton, Nucl. Phys. 89,69(1966).

(FES 58) H. Feshbach, Ann. Phys. 5,357(1958).

(FEY 49) R.P. Feynman, Phys. Rev. 76,749(1949).

(GLA 79) R.J. Glauber and P. Osland, Lett. Rev. 80B,401(1979).

(GRE 68) G.W. Greenlees, G.J. Pyle, and Y.C. Tang, Phys. Rev. 171,1115(1968).

(GLO 85) C.W. Glover et al, Phys. Rev. C31,1(1985).

(HOD 63) P.E. Hodgson, *The Optical Model of Elastic scattering*, Oxford University Press, London (1963).

(JAM 79) M.J. Jaminon, C. Mahaux, and P. Rochus, Phys. Rev. 43,1097(1979).

(KER 59) A.K. Kerman, H.McManus and R.M. Thaler, Ann. Phys. 8,551(1959).

(RAY 69) J. Raynal, **MAGALI**, *A Fortran IV-Program for automatic search in elastic scattering analysis with the nuclear optical model for spin 0, 1/2 and 1-particles*, Service de Physique Théorique Centre d'Eltudes Nucléaires de Saclay (1969).

(TIN 84) J. Tinsley and J. Rogers, Introduction to DACS, TRIUMF Design Note (TRI-DN-84-28), (1984);
The DACS EPROC compiler, TRIUMF Design Note (TRI-DN-84-29), (1984).

(TRI KH) TRIUMF Kinematics Handbook, ed. D.F. Measday, M.R. Menard, and J.E. Spuller.

Appendix A

```
;Event processor for MRS singles EXPT. 169 - 27/6/84
;
;Non-Linearity Correction for Top End VDC's (DF & PWG)
;New focal plane subr. XFOC + DRIFT mods. + XI calc (DAH)
;Redefining DRIFT function to use
;actual CAMAC word count (P.W.G)
;Including the LeCroy 4290 Drift chamber Readout
;Also, "improved" DRIFT
;Also including ECLine Programming
;
.TITLE EPROC
.EDFIN BLKDAT INLIN -LOCAL 1 LOCAL DIM
.EDFIN BLOCK BLOCK -LOCAL 2 LOCAL DIM LOCAL DATA
L=LOCAL
;NEED A SHORT FORM TO GET THIS NEXT MACRO ON ONE LINE
.EDFIN B1D BONED -SPECTRUM 4 L DIM L XDATA L XCOMP
      L XBIAS L LABEL
.EDFIN B2D BTWOD -SPECTRUM 9. L DIM L XDIM L XDATA
      L XCOM L XBIAS  L YDIM L YDATA L YCOMP L YBIAS
.EDFIN FAND IFAND LOCAL 2 LOCAL IN1 LOCAL IN2
.EDFIN DRIFT DRIFT -L 6 L DIM INPUT RAW L WIRE L IDCLO
      L IDCSL L TIME
.EDFIN XFOC XFOC L 6 L X1 L X2 L F L G L H L TILT
.EDFIN LINIT LINIT -LOCAL 2 LOCAL DIM LOCAL EFF#
.EDFIN L1COM L1COM LOCAL 4 LOCAL X LOCAL A
      LOCAL SCALE LOCAL B
```

```
.EDFIN L2COM L2COM LOCAL 6 L X L A L Y L B L SCALE L C
.EDFIN SCA1D SCA1D LOCAL 3 LOCAL X LOCAL LL LOCAL UL
.EDFIN SCALER SCOUN SPECTRUM 1 LOCAL DIM
.EDFIN SCAMAC SSCLR SPECTRUM 2 LOCAL DIM INPUT NEWS
.EDFIN SHIFT ISHFT LOCAL 3 LOCAL DATA LOCAL MASK
       LOCAL L-SHIFT
.EDFIN W1D WONED SPECTRUM 4 LOCAL DIM LOCAL XDATA
       LOCAL XCOMP LOCAL XBIAS LOCAL LABEL
.EDFIN W2D WTWOD SPECTRUM 9. L DIM L XDIM L XDATA
       L XCOMP L XBIAS  L YDIM L YDATA L YCOMP L YBIAS
.EDFIN MAXV MAXV LOCAL 4 LOCAL INDX LOCAL LIST
       LOCAL FRST LOCAL LAST
;
;
;*****************************************************
;First define symbols needed for event type #1.
;This event readsscalers at a uniform rate,
;checking for 24-bit overflow and calculating the
;average rate of each scaler.  CSCL is a spectrum
;type array of dimension = # of scalers read.
;Other definitions(OLDS,NEWS,DELS) are local scratch
;storage for overflows and rate.
;*****************************************************
;
.IDFIN SORG 4
;Origin skips event and block header words.
.DFIN CSCL SCAMAC 38. SORG
```

```
.DFIN OLDS BLKDAT 76.
.DFIN NEWS BLKDAT 76.
.DFIN DELS BLKDAT 76.
.DFIN CNT1 SCALER 1
;
;*****************************************************
;* Now for the definitions used in event type #2, *
;* the main event.  *
;*****************************************************
;
;The following constants must be defined in order to
;allow programming of the ECLine electronics.
;See the file MRSELECT.DC for a description of what
;they do and how to change them.
;
.EQUIV  FXMIN   0      ;Front End Chamber X-acceptance
.EQUIV  FXMAX   1600.  ;In 50 micron units
.EQUIV  FYMIN   0      ;Front End Chamber Y-acceptance
.EQUIV  FYMAX   1600.
.EQUIV  PDMIN   0      ;Selection of Top End Paddles
.EQUIV  PDMAX   7
.EQUIV  FPPOL   0
;Focal Plane Polarimeter in the Trigger?
.EQUIV  AUXTR   0      ;Fast Auxiliary Trigger?
.EQUIV  TRMIN   10.
;Minimum Top-Bottom Resolving Time in ns.
.EQUIV  TRMAX   133.   ;Maximum     "          "
```

```
.EQUIV  TRHS    0
.EQUIV  THRSH   30      ;FOCAL PLANE PADDLE THRESHOLDS
.EQUIV  PSCL    1       ;EVENT TRIGGER PRESCALER
.EQUIV  RFDEL   0       ;PHASE OF RF TDC STOP
.EQUIV  FETRIG  1       ;FRONT END TRIGGER REQUIREMENT
;
;Next, the logical variable used in hurry(EA/H)
;processing.HURRY is .FALSE. at the beginning
;of each input record. It becomes .TRUE. part way
;through the record if there are input events
;being delayed because the EPROC processing is
;taking too long.
;Next the definitions of MRS MWC decoded wires and
;associated calculations.
;Two constants are required
;for Non Linearity Correction.
;
.EQUIV IDCLO 340.       ;Times greater than this are
.EQUIV IDCSL 2000.      ;corrected by this slope
                        ;(divided by 1000)
.DFIN MWC0 DRIFT 37. MWORG LWIR IDCLO IDCSL DELT
.IDFIN MWORG 26.
;defines block header of variable length  MWC list
.EQUIV LWIR 0.
;Define N for some pair of wires (N & N+1).
.EQUIV DELT 50.         ;dTIME for FEC calculation
.EQUIV X0  MWC0 3.
```

```
.EQUIV Y0  MWC0 4.
.EQUIV X1  MWC0 8.
.EQUIV U1  MWC0 5.
.EQUIV X2  MWC0 6.
.EQUIV U2  MWC0 7.
.EQUIV TX0 MWC0 9.
.EQUIV TY0 MWC0 10.
.EQUIV TX1 MWC0 14.
.EQUIV TX2 MWC0 12.
.EQUIV WIRA MWC0 15.
.EQUIV WIRB MWC0 16.
.EQUIV NHT1 MWC0 21.
.EQUIV NHT2 MWC0 22.
.EQUIV NHT3 MWC0 23.
.EQUIV NHT4 MWC0 24.
.EQUIV NHT5 MWC0 25.
.EQUIV NHT6 MWC0 26.
.EQUIV NHT7 MWC0 27.
.EQUIV NHT8 MWC0 28.
.EQUIV NCL5 MWC0 33.
.EQUIV NCL6 MWC0 34.
.EQUIV NCL7 MWC0 35.
.EQUIV NCL8 MWC0 36.
;
;Next, the definition of the fixed position
;input data items.
.IDFIN IORG 0
```

```
;The beginning of the 4-word CAMAC header
.DFIN DATA BLOCK 40. IORG
;block moves all fixed position data items to local DATA.
;
.EQUIV DCR DATA 4
.EQUIV TTB DATA 6.
.EQUIV TRF DATA 7.
.EQUIV FPP DATA 14.
.EQUIV INDX 0
;
;Next, define spectra etc.
;
.DFIN CNT2 SCALER 1
.DFIN LPULSR FAND DCR 10000
.DFIN CNPULS SCALER 1
.DFIN ESUM MAXV INDX FPP PDMIN PDMAX
.DFIN LPROT FAND LAWIND LTWIND
.DFIN LAWIND SCA1D ESUM 0. 1024.
.DFIN LTWIND SCA1D TTB 0 1024.
.DFIN CPROT SCALER 1
.DFIN LMWNG FAND MWC0 37777
.DFIN CMWOK SCALER 1
.DFIN LFEC FAND MWC0 0
.DFIN LSOLID FAND LX0 LY0
.DFIN LX0 SCA1D X0 0 1600.
.DFIN LY0 SCA1D Y0 0 1600.
.DFIN XF XFOC X1 X2 -4210. 5472. 7392. -1066.
```

```
.DFIN Y0C L1COM Y0 1 1 -1000
.DFIN XFCC L1COM Y0C Y0C -100. XFC
.DFIN SXIXF W2D 40966 64.
      XFK 100. 5000. 64. XI 25. 0.
.DFIN XI L2COM X0 1000. THPC 6383. 1000. 0.
.DFIN XFK L2COM XFCC 1000. Y0 0. 1000. 0.
.DFIN XFC L1COM THPC THPC -30. XF
;QUADRATIC ABBERATION
.DFIN THET L2COM X1 -914. X2 914. 10000. -175.
;THETA in milliradians, center=0
.DFIN THPC L2COM THET 10000. XF -70. 10000. 122.
.DFIN THWN SCA1D THPC -500. 500.
.DFIN XFWN SCA1D XFK -32766. 32766.
.DFIN Y1 L2COM X1 1732. U1 -2000. 1000. 2315.
;Y1 in 50 micron units, center=0
.DFIN Y2 L2COM X2 1732. U2 -2000. 1000. 2829.
;Y2 in 50 micron units, center=0
.DFIN PHI L2COM Y1 -1827. Y2 1827. 1414. 0.
;PHI in 10ths of a milliradian centred on 0
.DFIN SPID W2D 4096. 64. TTB 16. 0 64. ESUM 4. 0
.DFIN SX0 W1D 160. X0 10. 0
.DFIN SY0 W1D 160. Y0 10. 0
.DFIN SX1 W1D 512. X1 40. 0
.DFIN SU1 W1D 512. U1 40. 0
.DFIN SX2 W1D 512. X2 40. 0
.DFIN SU2 W1D 512. U2 40. 0
.DFIN SXF W1D 512. XFK 40. 10000.
```

```
.DFIN SXFX0 W2D 4096. 64.
      XFK 100. 12000. 64. X0 25. 0.
.DFIN SXFY0 W2D 4096. 64.
      XFK 100. 12000. 64. Y0 25. 0
.DFIN SXFTH W2D 4096. 64.
      XFK 100. 12000. 64. THPC 4. -128.
.DFIN STX1 W1D 256. TX1 1 128.
.DFIN PAIR W2D 4096. 64. WIRA 8. 0 64. WIRB 8. 0
.DFIN SY0Y1 W2D 4096. 64.
      Y0 25. 0. 64. Y1 100. -3200.
.DFIN COR5 W2D 128. 16. NHT5 1 0 8. NCL5 1 0
.DFIN COR6 W2D 128. 16. NHT6 1 0 8. NCL6 1 0
.DFIN COR7 W2D 128. 16. NHT7 1 0 8. NCL7 1 0
.DFIN COR8 W2D 128. 16. NHT8 1 0 8. NCL8 1 0
.DFIN CORX W2D 64. 8. NHT1 1 0 8. NHT2 1 0
.DFIN CORY W2D 64. 8. NHT3 1 0 8. NHT4 1 0
.DFIN TDC W1D 512. WIRA 1 0
.DFIN STRF W2D 4096. 64. TRF 8. 0 ESUM 4. 0
.DFIN SANGL W1D 128. Y0 2 0
;
;*********************************************
;* And now for the operation sequence code. *
;*********************************************
;
.EVENT EVNT1
CNT1
CSCL
```

```
.EDONE
.EVENT EVNT2
CNT2
IF LPULSR
ELSE
  CNPULS       ;counts non-pulser events
  SPID
;to check particle i.d. window(selecting protons).
  STRF         ; R.F. timing to look for decel beam
  SX0
  SY0
  SX1
  SU1
  SX2
  SU2
  IF LPROT           ;protons only from here on.
    CPROT            ;counts them
   IF LFEC
   ELSE
   CORX
   CORY
   COR5
   COR6
   COR7
   COR8
   THEN
   PAIR
```

```
   IF LMWNG
;rejecting missing and multiple MWC events from here on.
   ELSE
      CMWOK
      IF XFWN
      SY0Y1      ;check non-bend plane focus
      ELSE
      THEN
      SXFX0
      IF THWN
SXFY0      ;check kinematic shift correction
      IF LSOLID
SXIXF     ;traceback to beam height at target
SXF
      IF XFWN
SANGL     ;angular distribution of selected peak
      ELSE
      THEN
      ELSE
      THEN
      ELSE
      THEN
               SXFTH
               STX1
               TDC
  THEN
 ELSE
```

```
  THEN
THEN
.EDONE
.EVENT EVNT3
.EDONE
.ALLDONE
.END
```

Appendix B

```
      SUBROUTINE DRIFT(X,LENX,BUF,IWIRE,IDCBASE,IDCSLOPE,DELT)
C
C  Including correction for for non-linearities in the
C  top end VDC's
C
C  If the time (T3) for a given wire is greater
C  than IDCBASE, it is scaled linearly by the
C  slope IDCSLOPE/1000
C
      PARAMETER AMASK=76000K,DMASK=1777K,SH5=40K,SH10=2000K,
     *  NPLANE=8,                          ;Number of wireplanes
     *  NDIM=6,NFEC=15,
C  ;Number of decoded coord. & "Front End Chambers"
     *  MINTDC=3, MAXTDC=5,
C  ;Minimun & Maximum # of TDC's desired
     *  METRIC=120, METRICB2=METRIC/2,
C  ;METRIC gives units of resulting X
     *  FECMTRC=100, FECMTRCB2=FECMTRC/2,
     *  FECMTRCB4=FECMTRC/4
      INTEGER   BUF(50),X(0:18),DELT,LL(NPLANE),
     *  UL(NPLANE),CHN(MAXTDC),
     *  TDC(MAXTDC),TEMP,FIRST,LAST,ADDR,T1,T3,TDC1
      LOGICAL ODD,ITEST
      LOGICAL BFEC
      DATA LL/0,16,32,48,64,224,400,576/
      DATA UL/15,31,47,63,223,399,575,735/
```

```
      DATA RNDM /-0.5/
C     NDAT = IAND (BUF(1), 377K) - 1
C     ;Length according to CAMAC
      NTDC=IAND(BUF(2),DMASK) + 1
C     ;Length according to Readout Controller
C     IF (NTDC .GT. NDAT) NTDC = NDAT
C     ;Choose the lesser (of two evils ?)
      DO 1 I=0,LENX-1
      X(I)=0
1     CONTINUE
      ODD=.FALSE.
      J=0                       ;Index of current wireplane
      K=2                       ;Index of current coordinate
      I=3                       ;Index of current input datum
C     For each wireplane...
C
C     Note that ITEST starts counting at bit 0
C
5     BFEC = ITEST (NFEC, J)
      J = J + 1
      IF (J .GT. NPLANE) GO TO 50
      FIRST=LL(J)
      LAST=UL(J)
      NHIT=0
      NCLUST=0
      MAX=0
C     For each element of raw data...
```

```
10 IF (I .GT. NTDC) GO TO 20
C  ;If we ain't got no more data, stop looping
   TEMP=BUF(I)
   IF (TEMP .GE. 0) GO TO 12
C  ;If MSB set this is module header.
   MODULE=IAND(TEMP,AMASK)/SH5
C  ;Extract module address & shift right 5
   GO TO 15
12 ADDR=TEMP/SH10+MODULE
C  ;Extract TDC address & shift right 10
   IF (ADDR .LT. FIRST) GO TO 15
   IF (ADDR .GT. LAST) GO TO 20
   T3=IAND(TEMP,DMASK)
   IF (T3 .GT. 511) GO TO 15        ;TDC time-out?
C  Now we have a GOOD hit in the current plane.
C  If this is the first hit in the plane
C  or if address isn't adjacent to last address,
C  increment # of CLUSTERS of hits.
   IF (NHIT .EQ. 0) GO TO 13
   IF (ADDR-CHN(NHIT) .EQ. 1) GO TO 14
13 NCLUST=NCLUST+1
14 NHIT=NHIT+1                      ;In any case boost # if HITS
   IF (NHIT .GT. MAXTDC) GO TO 15
   CHN(NHIT)=ADDR
C
C  This section currects non-linearities in the
C  Top End VDC's for particles which are close to a wire
```

```
C
      IF (IDCBASE .LE. 0) GO TO 19
      RNDM = RNDM + .00314159
      IF (RNDM .GE. 0.5) RNDM = -0.5
C
C  Not Front End Chambers
C
      IF (BFEC) GO TO 19
C
C  Only Large Times
C
      IF (T3 .LE. IDCBASE) GO TO 19
      T3 = IDCBASE + IFIX(FLOAT(IDCSLOPE)*
     *(T3+RNDM-FLOAT(IDCBASE))/1000.)
19    TDC(NHIT) = T3
      IF (T3 .LE. MAX) GO TO 15     ;Look for maximum time
      MAX=T3                        ;Save T(max)
      N=NHIT                        ;Save address of T(max)
15    I=I+1                         ;Boost pointer -> next item
C  Next 8 lines are temp. diagnostic stuff
      IF (ADDR .EQ. IWIRE) X(15)=TDC(NHIT)
      IF(IWIRE.LT.64)GO TO 16  ;F.E.C.'s are a special case
      IF (ADDR .EQ. IWIRE-1) GO TO 18
      GO TO 10
16    IF(IWIRE.LT.32 .AND. ADDR.EQ.32-IWIRE)GO TO 18
      IF(ADDR. NE .64-IWIRE)GO TO 10
18    X(16)=TDC(NHIT)
```

```
      GO TO 10
C     Analyze results for this plane
20    X(J+20)=NHIT
      X(J+28)=NCLUST
      IF (BFEC) GO TO 30    ;Decide how to handle this plane
C     Vertical Drift Chamber type
      K=K+1
      IF (NHIT .LT. MINTDC) GO TO 40
      IF (NHIT .GT. MAXTDC) GO TO 45
      IF (NCLUST .NE. 1) GO TO 45
      IF (N .EQ. 1) GO TO 40
      IF (N .EQ. NHIT) GO TO 40
      T1=TDC(N-1)
      T3=TDC(N+1)
      MIN=MIN0(T1,T3)
      X(K)=METRIC*(CHN(N)-FIRST)-METRICB2*(T3-T1)/(MIN-MAX)
      X(K+NDIM)=MAX+ABS(T3-T1)/2
      X(K+NDIM*2)=MAX-MIN
      GO TO 5
C     "Front End" type
30    ODD=.NOT.ODD
      IF (ODD) K=K+1
      IF (NHIT .GT. 1) GO TO 45
      IF (NCLUST .GT. 1) GO TO 45
      IF (ODD) GO TO 36
      IF (N1 .LT. 0) GO TO 35          ;1st plane not hit
C     1st Plane Was Hit
```

```
      X(K)=N1*FECMTRC
      IF (NHIT .EQ. 0) GO TO 5          ;2nd plane not hit
C     2nd Plane Hit Too
      T1=(LAST-CHN(1)-N1)*2+1
      IF (ABS(T1) .NE. 1) GO TO 45
C     ;Hits from each plane weren't adjacent
      X(K)=X(K)+T1*(TDC(1)-TDC1+DELT)*FECMTRCB4/DELT
      X(K+NDIM)=(TDC(1)+TDC1)/2
      IF (IWIRE .EQ. N1) X(16)=TDC(1)
      GO TO 5
C     Only 2nd Plane Hit (?)
35    IF (NHIT .EQ. 0) GO TO 40         ;No - neither was hit
      X(K)=(LAST-CHN(1))*FECMTRC+FECMTRCB2
      GO TO 5
C     First plane of 2 for a coordinate
36    N1=CHN(1)-FIRST                   ;Save address of hit
      IF (NHIT .EQ. 0) N1=-1            ;No hit in this plane
      TDC1=TDC(1)
      GO TO 5
C     "MISSING" a hit in plane
40    CALL ISET(X(2),K-3)
      GO TO 5
C     "MULTIPLE" hit in plane
45    CALL ISET(X(1),K-3)
      T1=METRIC
      IF (BFEC) T1 = FECMTRC
      X(K)=(LAST-FIRST+1)*T1
```

```
      GO TO 5
50    X(0)=IOR(X(1),X(2))
      END
```

Appendix 1

June'84 ('new') differential cross section data.
All data given in lab. reference.

200 MeV

Angle	(mb/sr)	error	Angle	(mb/sr)	error
15.4443	66.1999	1.5978	16.4342	43.9285	1.3678
17.4242	31.8985	1.0924	17.4243	33.9206	0.7855
17.9443	30.2312	0.4998	18.4142	22.6576	0.6807
18.9342	17.6543	0.4450	19.4042	14.9914	0.5461
19.9242	12.6525	0.3599	19.9443	13.1981	0.3278
19.9543	11.1644	0.3402	20.9342	8.4923	0.3005
20.9442	5.5650	0.3078	21.9242	6.2197	0.2450
21.9342	4.7416	0.2560	21.9443	6.6532	0.1881
22.9342	4.8470	0.1720	23.9242	3.7310	0.1450
23.9343	4.0136	0.0895	24.9242	3.1435	0.0835
25.9142	2.5723	0.0716	25.9443	2.7105	0.0912
26.9342	2.7831	0.0905	27.9242	2.0223	0.0776
29.9243	1.6826	0.0440	30.9142	1.6105	0.0436
31.9042	1.3741	0.0393	31.9343	1.3504	0.0365
32.9242	1.4050	0.0364	33.9142	1.1315	0.0324
33.9243	1.0082	0.0289	34.9142	1.0536	0.0289
35.9042	0.9256	0.0263	35.9343	0.8446	0.0202
36.9242	0.8572	0.0201	37.9142	0.7170	0.0181
37.9342	0.6373	0.0151	38.9242	0.6232	0.0145
39.9142	0.5359	0.0133	39.9343	0.3808	0.0096
40.9243	0.4408	0.0102	41.9142	0.3653	0.0092

300MeV

Angle	(mb/sr)	error	Angle	(mb/sr)	error
26.9100	2.0900	0.0550	25.9100	2.4380	0.0590
24.9200	2.2790	0.0550	24.9100	2.3150	0.0620
23.9100	2.1410	0.0640	22.9200	2.0630	0.0610
22.9200	2.1280	0.0690	21.9200	1.7660	0.0710
20.9300	1.9410	0.0740	20.9000	1.4480	0.1170
19.9000	1.7070	0.1520	18.9100	3.6210	0.1840
18.9300	3.7550	0.2810	17.9300	6.3500	0.3880
16.9400	13.1240	0.4800	17.3100	9.4170	0.6240
16.3100	18.0990	0.8420	15.3200	35.0470	1.0580
33.9200	0.3420	0.0150	32.9200	0.5560	0.0190
31.9300	0.6840	0.0210	28.9200	1.6590	0.0610
27.9200	1.8520	0.0650	26.9300	2.2350	0.0700

400 MeV

Angle	(mb/sr)	error	Angle	(mb/sr)	error
24.0336	2.4080	0.1275	23.1198	2.8046	0.1382
22.2060	3.3964	0.1422	26.0236	1.2738	0.0703
25.1098	1.7174	0.0815	24.1960	2.3649	0.0860
20.0336	2.7376	0.1087	19.1198	1.7726	0.1043
18.2060	1.2149	0.1017	18.0436	0.8618	0.1270
17.1298	0.3670	0.1759	16.2160	0.7518	0.2532

500 MeV

Angle	(mb/sr)	error	Angle	(mb/sr)	error
15.6260	1.6922	0.1222	16.5398	3.6888	0.1345
17.4536	5.4194	0.1529	18.2060	5.6995	0.2063
19.1198	5.1526	0.2078	20.0336	4.4713	0.1939
20.1960	4.4928	0.1373	21.1098	3.3729	0.1292
22.0236	2.2899	0.1102	22.2160	2.1403	0.0689
23.1298	1.0857	0.0589	23.7160	1.0243	0.0384
24.0436	0.6025	0.0461	24.6298	0.5521	0.0289
25.2160	0.3058	0.0134	25.5436	0.2099	0.0204
26.1298	0.1344	0.0097	26.2060	0.1218	0.0070
27.0436	0.0612	0.0073	27.1198	0.0719	0.0058
28.0336	0.0746	0.0056	29.2160	0.1076	0.0043
30.1298	0.1204	0.0048	30.2160	0.1229	0.0059
31.0436	0.1256	0.0047	31.1298	0.1249	0.0062
31.2060	0.1430	0.0047	32.0436	0.1205	0.0059
32.1198	0.1278	0.0045	32.7160	0.1256	0.0044
33.0336	0.0985	0.0039	33.6298	0.0942	0.0039
34.5436	0.0709	0.0033	35.2060	0.0612	0.0023
36.1198	0.0384	0.0018	37.0336	0.0236	0.0015
37.7060	0.0194	0.0008	38.6198	0.0100	0.0006
39.5336	0.0054	0.0004	39.9860	0.0065	0.0005
40.8998	0.0034	0.0004	41.8136	0.0023	0.0003
43.2160	0.0027	0.0005	44.1298	0.0023	0.0004
45.0436	0.0026	0.0004			

Appendix 2

July'81 and April'82 ('old') differential cross sectiondata
- without re-normalization.
All data given in lab. reference.

200 MeV

Angle	(mb/sr)	error	Angle	(mb/sr)	error
3.0630	3060.3999	24.8630	3.5260	1854.4000	19.5090
3.9900	1266.8000	16.3130	4.4530	995.3200	14.5440
4.5630	945.1000	9.7267	5.0260	865.9800	9.3670
5.4900	806.8100	9.0850	5.9530	764.6500	8.8966
6.0630	743.1400	7.8401	6.5260	708.6500	7.6702
6.9900	691.9800	7.5850	7.4530	654.2500	7.4365
7.5530	661.7300	8.0938	8.0160	615.5200	7.8579
8.4800	579.3200	7.6653	8.9430	549.6500	7.4675
9.0630	549.6600	6.7976	9.5260	514.9300	6.6696
9.9900	467.5900	6.3794	10.4530	416.1600	6.0517
10.5730	399.0800	5.1749	11.0360	360.2100	4.9600
11.5000	325.9600	4.7613	11.9630	284.6300	4.4459
12.0830	263.9600	3.8835	12.5460	229.4900	3.6740
13.0100	207.9300	3.5017	13.4730	172.3600	3.2411
13.5630	191.1400	2.1882	14.0260	170.3000	2.0701
14.4900	147.9700	1.9369	14.9530	122.6200	1.7597
15.0630	94.0290	1.4161	15.5260	82.5270	1.3321
15.9900	70.6000	1.2360	16.4530	58.4810	1.1287
16.5830	54.1540	0.9442	17.0460	45.4270	0.8670
17.5100	38.5460	0.8011	17.9730	33.9970	0.7391
18.0630	27.8400	0.4301	18.5260	24.2400	0.4001
18.9900	20.4750	0.3680	19.4530	16.6410	0.3290
19.5730	13.5700	0.2519	20.0360	11.8040	0.2329
20.5000	9.6267	0.2080	20.9630	7.9967	0.1833

300 MeV

Angle	(mb/sr)	error	Angle	(mb/sr)	error
11.5970	122.9400	3.4200	12.2050	94.5030	2.8538
12.8140	72.1900	2.3745	10.1570	192.8900	6.5811
10.6650	157.1900	5.6254	11.2740	128.8500	4.8247
8.6070	304.3800	9.0824	9.2150	263.6500	7.9758
9.8240	203.6600	6.6896	7.0770	422.1600	13.1330
7.6850	396.0800	11.9690	8.2940	318.6100	10.1860
4.0770	792.1100	20.2980	4.6850	679.2100	17.7310
5.2940	598.7600	15.9430	2.5870	1264.3000	40.9430
3.1950	1201.6000	38.5240	3.8040	880.3600	29.7190

14.5970	30.6590	0.9948	15.2050	23.6420	0.8140
15.8140	17.7980	0.6546	16.0870	15.1950	0.4683
16.6950	10.4010	0.3685	17.3040	7.1381	0.2933
17.5770	5.6302	0.3378	18.1850	4.1795	0.2792
18.7940	3.2030	0.2388	19.1370	2.4622	0.0991
19.7450	1.9699	0.0828	20.3540	1.4842	0.0675
38.5160	0.0149	0.0032	38.9290	0.0177	0.0031
39.3410	0.0359	0.0035	39.7540	0.0379	0.0035
40.1660	0.0381	0.0035	40.5790	0.0488	0.0047
43.4960	0.0633	0.0022	43.9090	0.0601	0.0022
44.3210	0.0550	0.0021	44.7340	0.0549	0.0021
45.1460	0.0527	0.0020	45.5590	0.0467	0.0024
48.4960	0.0196	0.0014	48.9090	0.0161	0.0013
49.3210	0.0140	0.0012	49.7340	0.0127	0.0011
50.1460	0.0109	0.0010	50.5590	0.0093	0.0012
53.4760	0.0024	0.0002	53.8890	0.0018	0.0002
54.3010	0.0013	0.0002	54.7140	0.0011	0.0002
55.1260	0.0007	0.0002	55.5390	0.0006	0.0002
58.4760	0.0016	0.0005	58.8890	0.0017	0.0005
59.3010	0.0020	0.0005	59.7140	0.0015	0.0005
60.1260	0.0013	0.0005	60.5390	0.0019	0.0007
18.4960	3.4130	0.4922	18.9090	0.4955	0.3975
19.3210	1.0586	0.3600	19.7340	1.3043	0.3372
20.1460	0.8509	0.2890	20.5590	0.7089	0.3174
23.4760	3.6297	0.1955	23.8890	3.9189	0.2118
24.3010	3.9952	0.2063	24.7410	4.2954	0.2179
25.1260	3.5780	0.2116	25.5390	3.5580	0.2499
28.5160	2.4358	0.1293	28.9290	1.8756	0.1139
29.3410	1.7323	0.1068	29.7540	1.5006	0.0994
30.1660	1.2711	0.0893	30.5790	1.1593	0.0990
33.5160	0.2060	0.0164	33.9290	0.1822	0.0151
34.3410	0.1145	0.0132	34.7540	0.0610	0.0117
35.1660	0.0409	0.0098	35.5790	0.0162	0.0098

400 MeV

Angle	(mb/sr)	error	Angle	(mb/sr)	error
2.8590	2602.0000	49.4400	3.1230	2258.1001	44.8500
3.3880	2118.6001	42.6190	3.6520	1886.7000	39.5910
3.9170	1778.8000	38.0060	4.1820	1613.5000	35.9870
4.4460	1496.1000	34.1990	4.3580	1495.5000	25.7550
4.6230	1405.8000	24.8190	4.8880	1382.8000	24.6070
5.1520	1286.8000	23.4760	5.4170	1215.2000	22.7480
5.6820	1160.2000	22.1250	5.9460	1110.7000	21.5380
5.8480	1009.3000	20.5310	6.1130	1017.3000	20.3320
6.3780	913.1600	19.2750	6.6420	897.2200	18.9400
6.9070	819.7100	17.8300	7.1720	754.5400	16.8550
7.4360	698.9000	16.0980	7.3580	555.3100	16.5960
7.6230	604.7200	15.3410	7.8880	578.9600	15.4010
8.1520	533.4200	14.4520	8.4170	498.0400	13.8750

8.6820	459.0100	13.1100	8.9460	414.1100	12.2010
8.8580	388.0900	11.6680	9.1230	357.9800	11.0380
9.3880	321.8000	10.3060	9.6520	289.3800	9.5274
9.9170	267.9700	8.9764	10.1820	243.7600	8.5095
10.4460	209.4400	7.7130	10.3580	211.2300	6.7341
10.6230	184.1200	6.0248	10.9880	158.6400	5.3841
11.1520	144.5600	4.9924	11.4170	128.4800	4.5322
11.6820	114.7800	4.1391	11.9460	97.2330	3.6476
11.8680	96.1770	3.7467	12.1330	85.1540	3.3999
12.3980	71.0270	2.9912	12.6620	61.0390	2.6699
12.9270	52.3330	2.3150	13.1920	43.5000	2.1099
13.4560	38.4550	1.8268	14.8300	10.7960	0.6565
15.3800	6.3481	0.4898	15.9300	3.5165	0.3679
16.4800	1.7862	0.2674	18.8500	2.6479	0.1362
19.4000	3.4037	0.1521	19.9500	3.5894	0.1597
20.5000	3.6659	0.1615	19.6870	2.1939	0.0815
20.2280	2.3771	0.0855	20.7690	2.4782	0.0883
18.1170	1.7255	0.0651	18.6580	1.9104	0.0591
19.1990	2.1354	0.0580	16.6270	5.1379	0.2112
17.1680	3.7814	0.1724	17.7090	3.6372	0.1476
15.1270	12.6660	0.3732	15.6680	8.3603	0.3065
16.2090	5.7051	0.2485	15.1270	11.7090	0.5148
15.6680	8.3614	0.4294	16.2090	5.7319	0.3483
13.6270	37.9590	1.2666	14.1680	26.9700	1.0509
14.7090	17.7190	0.8547	12.1270	95.1310	2.9193
12.6680	74.9820	2.5136	13.2090	50.6440	2.0712
18.4370	2.5052	0.1433	18.9870	2.7675	0.1281
19.5370	3.2116	0.1361	20.0870	3.5997	0.1428
20.6370	3.8510	0.1487	21.4170	4.8912	0.1447
21.9670	4.8175	0.1358	22.5170	4.3795	0.1327
23.0670	3.7729	0.1255	23.6170	3.4279	0.1178
24.4170	4.0064	0.1111	24.9670	3.5690	0.0963
25.5710	2.9922	0.0849	26.0670	2.3765	0.0730
26.6170	1.7363	0.0597	27.4070	1.0061	0.0379
27.9570	0.6920	0.0286	28.5070	0.4315	0.0223
29.0570	0.2959	0.0173	29.6070	0.1779	0.0132
30.4070	0.1517	0.0069	30.9570	0.1177	0.0060
31.5070	0.0829	0.0048	32.0570	0.0677	0.0037
32.6070	0.0659	0.0036	33.4270	0.0492	0.0051
33.9770	0.0695	0.0046	34.5270	0.0840	0.0049
35.0770	0.0858	0.0051	35.6270	0.0870	0.0050
36.4270	0.0799	0.0042	36.9770	0.0753	0.0038
37.5270	0.0713	0.0036	38.0770	0.0656	0.0033
38.6270	0.0557	0.0031	39.4370	0.0498	0.0031
39.9870	0.0432	0.0026	40.5370	0.0323	0.0023
41.0870	0.0284	0.0022	41.6370	0.0216	0.0019
42.4170	0.0154	0.0010	42.9670	0.0119	0.0008
43.5170	0.0086	0.0007	44.0670	0.0061	0.0007
44.6170	0.0042	0.0006			

500 MeV

Angle	(mb/sr)	error	Angle	(mb/sr)	error
8.5390	595.1500	11.4900	9.1470	420.7100	9.0411
9.7560	269.5200	6.8066	6.9990	1272.2000	28.9580
7.6070	959.2800	24.3940	8.2160	717.8200	20.6630
5.5090	2832.8000	50.0260	6.1170	2159.1001	41.6280
6.7260	1710.2000	35.7310	4.0290	4524.5000	88.1940
4.6370	3686.1001	75.8170	5.2460	3020.3999	65.5890
2.5290	4401.6001	82.9230	3.1370	6114.8999	108.5400
3.7460	5016.2002	92.7340	11.5090	69.5950	1.2485
12.1170	41.8640	0.9139	12.7260	27.4850	0.6969
10.0090	210.9700	4.4004	10.6170	133.8400	3.3700
11.2260	85.3460	2.6216	10.0090	199.1000	4.4818
10.6170	126.8900	3.3686	11.2260	75.8600	2.5211
14.5090	12.4190	0.2917	15.1170	12.2040	0.2760
15.7260	12.5240	0.2722	16.0190	9.9709	0.2254
16.6270	9.8585	0.2255	17.2360	9.5777	0.2237
17.5190	9.0438	0.1786	18.1270	8.0874	0.1733
18.7360	7.5279	0.1689	18.9890	7.9144	0.1415
19.5970	6.5935	0.1312	20.2060	5.8219	0.1240
13.0190	19.4010	0.7122	13.6270	13.6240	0.5214
14.2360	12.7430	0.4486	11.5090	73.0970	2.8098
12.1170	43.9780	1.8528	12.7260	29.3570	1.3003
10.0090	239.6500	5.4656	10.6170	146.0800	3.9028
11.2260	93.7830	2.9476	3.0630	0.1193	0.0120

Appendix 3

July'81 and April'82 analyzing power data.
All data given in lab. reference.

200 MeV

Angle	Asymmetry	error	Angle	Asymmetry	error
3.5260	0.1866	0.0156	3.9900	0.3042	0.0193
4.4530	0.3603	0.0221	4.5630	0.3424	0.0131
5.0260	0.4383	0.0132	5.4900	0.4556	0.0137
5.9530	0.4956	0.0139	6.0630	0.5524	0.0142
6.5260	0.5639	0.0145	6.9900	0.5805	0.0145
7.4530	0.6529	0.0147	7.5530	0.6285	0.0135
8.0160	0.6701	0.0138	8.4800	0.6864	0.0141
8.9430	0.7157	0.0142	9.0630	0.7131	0.0121
9.5260	0.7471	0.0124	9.9900	0.7635	0.0129
10.4530	0.7876	0.0135	10.5730	0.7465	0.0112
11.0360	0.7621	0.0117	11.5000	0.8127	0.0119
11.9630	0.7979	0.0129	12.0830	0.8262	0.0149
12.5460	0.8262	0.0149	13.0100	0.9001	0.0166
13.4730	0.8861	0.0188	13.5630	0.9270	0.0177
14.0260	0.9521	0.0186	14.4900	0.9917	0.0199
14.9530	0.9852	0.0218	15.0630	1.0096	0.0269
15.5260	1.0258	0.0290	15.9900	1.0321	0.0315
16.4530	1.0426	0.0348	16.5830	0.9799	0.0300
17.0460	0.9407	0.0324	17.5100	0.9590	0.0355
17.9730	0.9127	0.0367	18.0630	0.8740	0.0247
18.5260	0.7991	0.0258	18.9900	0.7605	0.0278
19.4530	0.6618	0.0298	19.5730	0.6706	0.0286
20.0360	0.5330	0.0294	20.5000	0.3806	0.0313
20.9630	0.2709	0.0328			

300 MeV

Angle	Asymmetry	error	Angle	Asymmetry	error
11.5970	0.7945	0.0472	12.2050	0.7955	0.0512
12.8140	0.6868	0.0545	10.1570	0.6900	0.0559
10.6650	0.7274	0.0592	11.2740	0.7460	0.0619
8.6070	0.7212	0.0524	9.2150	0.7369	0.0533
9.8240	0.7223	0.0575	7.0770	0.5628	0.0510
7.6850	0.6595	0.0525	8.2940	0.6793	0.0557
4.0770	0.3046	0.0412	4.6850	0.3506	0.0421
5.2940	0.3993	0.0431	2.5870	-0.0159	0.0536
3.1950	0.0572	0.0527	3.8040	0.1811	0.0565
14.5970	0.6616	0.0568	15.2050	0.5479	0.0590

15.8140	0.4518	0.0624	16.0870	0.3813	0.0531
16.6950	0.2636	0.0606	17.3040	0.0537	0.0702
17.5770	-0.2828	0.0917	18.1850	-0.3958	0.1020
18.7940	-0.6133	0.1150	19.1370	-0.6607	0.0650
19.7450	-0.6572	0.0664	20.3540	-0.3973	0.0707
38.5160	-1.6751	0.4521	38.9290	-1.0677	0.2861
39.3410	-0,1387	0.0986	39.7540	0.0354	0.0856
40.1660	0.0178	0.0864	40.5790	0.3372	0.0802
43.4960	0.4287	0.0145	43.9090	0.3935	0.0161
44.3210	0.4037	0.0166	44.7340	0.4136	0.0161
45.1460	0.4069	0.0170	45.5590	0.3957	0.0232
48.4960	0.3761	0.0608	48.9090	0.3646	0.0672
49.3210	0.3069	0.0736	49.7340	0.3624	0.0768
50.1460	0.3629	0.0835	50.5590	0.3224	0.1120
53.4760	0.2946	0.0885	53.8890	0.2398	0.1070
54.3010	0.2503	0.1326	54.7140	0.2604	0.1390
55.1260	0.2935	0.1786	55.5390	0.1304	0.2961
58.4760	0.2275	0.1878	58.8890	0.3419	0.1493
59.3010	0.4377	0.1220	59.7140	0.3374	0.1681
60.1260	0.2265	0.2113	60.5390	0.3771	0.1775
18.4960	-0.2097	0.1320	18.9090	-5.2500	4.3575
19.3210	-1.4287	0.6120	19.7340	-0.7054	0.3159
20.1460	-0.9536	0.4815	20.5590	-1.1485	0.7048
23.4760	0.4463	0.0447	23.8890	0.4689	0.0436
24.3010	0.4920	0.0424	24.7410	0.4999	0.0412
25.1260	0.4283	0.0463	25.5390	0.4432	0.0552
28.5160	0.4245	0.0462	28.9290	0.4018	0.0524
29.3410	0.3851	0.0540	29.7540	0.3505	0.0584
30.1660	0.3607	0.0615	30.5790	0.3689	0.0752
33.5160	-0.2711	0.0806	33.9290	-0.2603	0.0842
34.3410	-0.6640	0.1471	34.7540	-1.6457	0.3956
35.1660	-2.0302	0.5797	35.5790	-4.7346	3.0408

400 MeV

Angle	Asymmetry	error	Angle	Asymmetry	error
2.8590	0.1380	0.0303	3.1230	0.1758	0.0316
3.3880	0.1830	0.0320	3.6520	0.1897	0.0333
3.9170	0.3224	0.0334	4.1820	0.2618	0.0350
4.4460	0.3417	0.0356	4.3580	0.3602	0.0246
4.6230	0.3792	0.0251	4.8880	0.4268	0.0249
5.1520	0.4116	0.0257	5.4170	0.4339	0.0262
5.6820	0.4771	0.0264	5.9460	0.4785	0.0268
5.8480	0.4307	0.0314	6.1130	0.4607	0.0308
6.3780	0.4672	0.0325	6.6420	0.4388	0.0324
6.9070	0.5071	0.0333	7.1720	0.5272	0.0342
7.4360	0.5281	0.0351	7.3580	0.6159	0.0375
7.6230	0.6368	0.0386	7.8880	0.6928	0.0385
8.1520	0.6973	0.0392	8.4170	0.6532	0.0409
8.6820	0.6341	0.0421	8.9460	0.6349	0.4936

8.8580	0.6130	0.0366	9.1230	0.6318	0.0373
9.3880	0.3091	0.0394	9.6520	0.5907	0.0411
9.9170	0.6243	0.0410	10.1820	0.6627	0.0420
10.4460	0.6451	0.0450	10.3580	0.5899	0.0389
10.6230	0.5740	0.0405	10.9880	0.5556	0.0425
11.1520	0.5574	0.0434	11.4170	0.5154	0.0453
11.6820	0.5167	0.0465	11.9460	0.4977	0.0490
11.8680	0.4239	0.0408	12.1330	0.4715	0.0488
12.3980	0.4220	0.0531	12.6620	0.4438	0.0549
12.9270	0.3469	0.0583	13.1920	0.3609	0.0638
13.4560	0.2986	0.0642	14.8300	-0.0104	0.0917
15.3800	-0.1234	0.1162	15.9300	-0.6236	0.1704
16.4800	-0.8555	0.2575	18.8500	1.0612	0.0660
19.4000	1.0440	0.0528	19.9500	0.9935	0.0532
20.5000	0.9522	0.0520	19.6870	0.8404	0.0676
20.2280	0.8765	0.0642	20.7690	0.8756	0.0632
18.1170	0.3506	0.0637	18.6580	0.6231	0.0553
19.1990	0.7625	0.0496	16.6270	-0.1077	0.0629
17.1680	0.0855	0.0694	17.7090	0.3305	0.0640
15.1270	0.1225	0.0439	15.6680	-0.0395	0.0539
16.2090	-0.0282	0.0644	15.1270	0.0059	0.0650
15.6680	-0.0009	0.0756	16.2090	0.0229	0.0894
13.6270	0.3593	0.0502	14.1680	0.3381	0.0583
14.7090	0.1322	0.0710	12.1270	0.5278	0.0494
12.6680	0.4386	0.0528	13.2090	0.3009	0.0640
18.4370	0.6151	0.0904	18.9870	0.8817	0.0691
19.5370	0.9740	0.0602	20.0870	1.0412	0.0532
20.6370	0.9782	0.0519	21.4170	0.9094	0.0406
21.9670	0.8501	0.0396	22.5170	0.8811	0.0430
23.0670	0.7081	0.0498	23.6170	0.6805	0.0518
24.4170	0.6248	0.0409	24.9670	0.5895	0.0400
25.5710	0.5096	0.0425	26.0670	0.4689	0.0460
26.6170	0.3694	0.0523	27.4070	0.1205	0.0594
27.9570	0.0583	0.0649	28.5070	-0.2032	0.0827
29.0570	-0.2844	0.0897	29.6070	-0.5878	0.1088
30.4070	-0.6431	0.0634	30.9570	-0.7167	0.0716
31.5070	-0.5130	0.0823	32.0570	-0.2243	0.0822
32.6070	0.1132	0.0830	33.4270	0.3151	0.1580
33.9770	0.5600	0.0993	34.5270	0.5540	0.0831
35.0770	0.6929	0.0820	35.6270	0.7960	0.0794
36.4270	0.7550	0.0716	36.9770	0.7695	0.0670
37.5270	0.7861	0.0680	38.0770	0.6504	0.0714
38.6270	0.7688	0.0753	39.4370	0.7588	0.0886
39.9870	0.5568	0.0918	40.5370	0.5779	0.1086
41.0870	0.4556	0.1169	41.6370	0.5389	0.1358
42.4170	0.3407	0.1010	42.9670	0.2621	0.1072
43.5170	0.3568	0.1311	44.0670	0.0846	0.1727
44.6170	0.2452	0.2282			

500 MeV

Angle	Asymmetry	error	Angle	Asymmetry	error
8.5390	0.4704	0.0367	9.1470	0.4229	0.0406
9.7560	0.5034	0.0482	6.9990	0.5267	0.0434
7.6070	0.4567	0.0480	8.2160	0.4852	0.0548
5.5090	0.3751	0.0333	6.1170	0.3735	0.0364
6.7260	0.3491	0.0392	4.0290	0.2456	0.0353
4.6370	0.3508	0.0377	5.2460	0.3146	0.0396
2.5290	0.1944	0.0348	3.1370	0.2071	0.0326
3.7460	0.2878	0.0344	11.5090	0.3392	0.0310
12.1170	0.2621	0.0383	12.7260	0.2514	0.0445
10.0090	0.4406	0.0364	10.6170	0.3851	0.0437
11.2260	0.3468	0.0532	10.0090	0.4416	0.0400
10.6170	0.4236	0.0471	11.2260	0.4245	0.0589
14.5090	0.6492	0.0396	15.1170	0.7056	0.0371
15.7260	0.7076	0.0350	16.0190	0.7658	0.0441
16.6270	0.8379	0.0448	17.2360	0.7717	0.0452
17.5190	0.7569	0.0383	18.1270	0.7687	0.0411
18.7360	0.6555	0.0424	18.9890	0.6523	0.0332
19.5970	0.6463	0.0368	20.2060	0.5652	0.0390
13.0190	0.2793	0.0717	13.6270	0.5160	0.0771
14.2360	0.5565	0.0709	11.5090	0.4637	0.0814
12.1170	0.4381	0.0893	12.7260	0.4739	0.0926
10.0090	0.4009	0.0413	10.6170	0.3738	0.0485
11.2260	0.3661	0.0571			

Appendix 4

June'84 ('new') and *renormalized* July'81, April'82 differential cross section data - selected set. All data given in lab. references.

200 MeV

Angle	(mb/sr)	error	Angle	(mb/sr)	error
3.0630	2448.3201	24.8630	3.9900	1013.4400	16.3130
4.5630	756.0800	9.7267	5.4900	645.4000	9.0850
6.0630	594.5000	7.8401	6.9900	553.6000	7.5850
7.5530	529.4000	8.0938	8.4800	463.5000	7.6653
9.0630	439.7000	6.7976	9.9900	374.1000	6.3794
10.5730	319.3000	5.1749	11.5000	260.8000	4.7613
12.5460	183.6000	3.6740	13.5630	152.9000	2.1882
14.4900	118.4000	1.9369	15.4443	66.1999	1.5978
15.9900	70.6000	1.2360	16.4342	43.9285	1.3678
16.4530	58.4810	1.1287	17.0460	45.4270	0.8670
17.4243	33.9206	0.7855	17.5100	38.5460	0.8011
17.9443	30.2312	0.4998	17.9730	33.9970	0.7391
18.4142	22.6576	0.6807	18.5260	24.2400	0.4001
18.9342	17.6543	0.4450	18.9900	20.4750	0.3680
19.4042	14.9914	0.5461	19.4530	16.6410	0.3290
19.9242	12.6525	0.3599	20.0360	11.8040	0.2329
20.5000	9.6267	0.2080	20.9342	8.4923	0.3005
20.9630	7.9967	0.1833	21.9443	6.6532	0.1881
22.9342	4.8470	0.1720	23.9343	4.0136	0.0895
24.9242	3.1435	0.0835	25.9142	2.5723	0.0716
26.9342	2.7831	0.0905	27.9242	2.0223	0.0776
29.9243	1.6826	0.0440	30.9142	1.6105	0.0436
31.9343	1.3504	0.0365	32.9242	1.4050	0.0364
33.9243	1.0082	0.0289	34.9142	1.0536	0.0289
35.9042	0.9256	0.0263	36.9242	0.8572	0.0201
37.9142	0.7170	0.0181	38.9242	0.6232	0.0145
39.9142	0.5359	0.0133	40.9243	0.4408	0.0102
41.9142	0.3653	0.0092			

300 MeV

Angle	(mb/sr)	error	Angle	(mb/sr)	error
2.5870	1264.3000	40.9430	3.1950	1201.6000	38.5240
4.0770	792.1100	20.2980	5.2940	598.7600	15.9430
7.0770	422.1600	13.1330	8.2940	318.6100	10.1860
9.2150	263.6500	7.9758	10.1570	192.8900	6.5811
11.2740	128.8500	4.8247	12.2050	94.5030	2.8538

15.3200	35.0470	1.0580	16.3100	18.0990	0.8420
17.3100	9.4170	0.6240	18.9100	3.6210	0.1840
19.1370	2.4622	0.0991	19.7450	1.9699	0.0828
19.9000	1.7070	0.1520	20.3540	1.4842	0.0675
20.9000	1.4480	0.1170	21.9200	1.7660	0.0710
22.9200	2.0630	0.0610	23.9100	2.1410	0.0640
24.9100	2.3150	0.0620	25.9100	2.4380	0.0590
26.9300	2.2350	0.0700	27.9200	1.8520	0.0650
28.9200	1.6590	0.0610	29.7540	1.5006	0.0994
30.5790	1.1593	0.0990	31.9300	0.6840	0.0210
32.9200	0.5560	0.0190	33.9200	0.3420	0.0150
33.9290	0.1822	0.0151	34.3410	0.1145	0.0132
35.5790	0.0162	0.0098	38.5160	0.0149	0.0032
39.7540	0.0379	0.0035	40.5790	0.0488	0.0047
40.5790	0.0488	0.0047	43.4960	0.0633	0.0022
43.9090	0.0601	0.0022	44.7340	0.0549	0.0021
45.1460	0.0527	0.0020	45.5590	0.0467	0.0024
48.4960	0.0196	0.0014	48.9090	0.0161	0.0013
49.3210	0.0140	0.0012	50.1460	0.0109	0.0010
50.5590	0.0093	0.0012	53.4760	0.0024	0.0002
53.8890	0.0018	0.0002	54.3010	0.0013	0.0002
54.7140	0.0011	0.0002	55.1260	0.0007	0.0002
58.4760	0.0016	0.0005	58.8890	0.0017	0.0005
59.3010	0.0020	0.0005	60.5390	0.0019	0.0007

400 MeV

Angle	(mb/sr)	error	Angle	(mb/sr)	error
2.8590	2602.0000	49.4400	3.3880	2118.6001	42.6190
4.1820	1613.5000	35.9870	5.4170	1215.2000	22.7480
6.3780	913.1600	19.2750	7.1720	754.5400	16.8550
8.1520	533.4200	14.4520	9.1230	357.9800	11.0380
10.3580	211.2300	6.7341	11.6820	114.7800	4.1391
12.1330	85.1540	3.3999	13.6270	37.9590	1.2666
14.7090	17.7190	0.8547	15.6680	8.3603	0.3065
16.2090	5.7051	0.2485	16.2160	0.7518	0.2532
16.4800	1.7862	0.2674	17.1298	0.3670	0.1759
18.0436	0.8618	0.1270	18.2060	1.2149	0.1017
18.8500	2.6479	0.1362	19.1198	1.7726	0.1043
19.4000	3.4037	0.1521	19.9500	3.5894	0.1597
20.0336	2.7376	0.1087	20.6370	3.8510	0.1487
21.4170	4.8912	0.1447	21.9670	4.8175	0.1358
22.2060	3.3964	0.1422	22.5170	4.3795	0.1327
23.0670	3.7729	0.1255	23.1198	2.8046	0.1382
23.6170	3.4279	0.1178	24.0336	2.4080	0.1275
24.1960	2.3649	0.0860	25.1098	1.7174	0.0815
26.0236	1.2738	0.0703	27.9570	0.6920	0.0286
28.5070	0.4315	0.0223	29.6070	0.1779	0.0132
30.9570	0.1177	0.0060	31.5070	0.0829	0.0048
32.6070	0.0659	0.0036	33.9770	0.0695	0.0046

34.5270	0.0840	0.0049	35.6270	0.0870	0.0050
37.5270	0.0713	0.0036	38.6270	0.0557	0.0031
39.9870	0.0432	0.0026	41.6370	0.0216	0.0019
42.9670	0.0119	0.0008	43.5170	0.0086	0.0007
44.6170	0.0042	0.0006			

500 MeV

Angle	(mb/sr)	error	Angle	(mb/sr)	error
2.5290	2905.1001	82.9230	3.1370	4035.8000	108.5400
3.7460	3310.7000	92.7340	4.6370	2432.8000	75.8170
5.5090	1869.4000	50.0260	6.7260	1419.5000	35.7310
7.6070	796.2000	24.3940	8.2160	595.8000	20.6630
8.5390	494.0000	11.4900	9.1470	349.2000	9.0411
9.7560	223.7000	6.8066	10.0090	199.1000	4.4818
10.6170	126.8900	3.3686	11.2260	75.8600	2.5211
11.5090	69.5950	1.2485	12.1170	41.8640	0.9139
12.7260	27.4850	0.6969	13.0190	19.4010	0.7122
15.6260	1.6922	0.1222	16.5398	3.6888	0.1345
17.4536	5.4194	0.1529	18.2060	5.6995	0.2063
19.1198	5.1526	0.2078	20.0336	4.4713	0.1939
20.1960	4.4928	0.1373	21.1098	3.3729	0.1292
22.0236	2.2899	0.1102	22.2160	2.1403	0.0689
23.1298	1.0857	0.0589	23.7160	1.0243	0.0384
24.0436	0.6025	0.0461	24.6298	0.5521	0.0289
25.2160	0.3058	0.0134	25.5436	0.2099	0.0204
26.1298	0.1344	0.0097	26.2060	0.1218	0.0070
27.0436	0.0612	0.0073	27.1198	0.0719	0.0058
28.0336	0.0746	0.0056	29.2160	0.1076	0.0043
30.1298	0.1204	0.0048	30.2160	0.1229	0.0059
31.0436	0.1256	0.0047	31.1298	0.1249	0.0062
31.2060	0.1430	0.0047	32.0436	0.1205	0.0059
32.1198	0.1278	0.0045	32.7160	0.1256	0.0044
33.0336	0.0985	0.0039	33.6298	0.0942	0.0039
34.5436	0.0709	0.0033	35.2060	0.0612	0.0023
36.1198	0.0384	0.0018	37.0336	0.0236	0.0015
37.7060	0.0194	0.0008	38.6198	0.0100	0.0006
39.5336	0.0054	0.0004	39.9860	0.0065	0.0005
40.8998	0.0034	0.0004	41.8136	0.0023	0.0003
43.2160	0.0027	0.0005	44.1298	0.0023	0.0004
45.0436	0.0026	0.0004			

Appendix 5

Selected analyzing power data used in optical model analysis.
All data given in lab. reference.

200 MeV

Angle	Asymmetry	error	Angle	Asymmetry	error
3.0630	0.1193	0.0120	3.5260	0.1866	0.0156
3.9900	0.3042	0.0193	4.4530	0.3603	0.0221
4.5630	0.3424	0.0131	5.0260	0.4383	0.0132
5.4900	0.4556	0.0137	6.0630	0.5524	0.0142
6.5260	0.5639	0.0145	6.9900	0.5805	0.0145
7.5530	0.6285	0.0135	8.0160	0.6701	0.0138
8.4800	0.6864	0.0141	9.0630	0.7131	0.0121
9.5260	0.7471	0.0124	9.9900	0.7635	0.0129
10.4530	0.7876	0.0135	10.5730	0.7465	0.0112
11.0360	0.7621	0.0117	11.5000	0.8127	0.0119
11.9630	0.7979	0.0129	12.0830	0.8262	0.0149
12.5460	0.8262	0.0149	13.0100	0.9001	0.0166
13.4730	0.8861	0.0188	13.5630	0.9270	0.0177
14.0260	0.9521	0.0186	14.4900	0.9917	0.0199
14.9530	0.9852	0.0218	15.0630	1.0096	0.0269
15.5260	1.0258	0.0290	15.9900	1.0321	0.0315
16.4530	1.0426	0.0348	16.5830	0.9799	0.0300
17.0460	0.9407	0.0324	17.5100	0.9590	0.0355
17.9730	0.9127	0.0367	18.0630	0.8740	0.0247
18.5260	0.7991	0.0258	18.9900	0.7605	0.0278
19.4530	0.6618	0.0298	19.5730	0.6706	0.0286
20.0360	0.5330	0.0294	20.5000	0.3806	0.0313
20.9630	0.2709	0.0328			

300 MeV

Angle	Asymmetry	error	Angle	Asymmetry	error
2.5870	-0.0159	0.0536	3.8040	0.1811	0.0565
4.6850	0.3506	0.0421	5.2940	0.3993	0.0431
7.6850	0.6595	0.0525	8.6070	0.7212	0.0524
9.2150	0.7369	0.0533	10.1570	0.6900	0.0559
11.2740	0.7460	0.0619	12.2050	0.7955	0.0512
12.8140	0.6868	0.0545	14.5970	0.6616	0.0568
15.2050	0.5479	0.0590	16.6950	0.2636	0.0606
17.5770	-0.2828	0.0917	18.4960	-0.2097	0.1320
19.7450	-0.6572	0.0664	20.3540	-0.3973	0.0707
23.4760	0.4463	0.0447	24.3010	0.4920	0.0424

25.1260	0.4283	0.0463	28.9290	0.4018	0.0524
29.7540	0.3505	0.0584	30.5790	0.3689	0.0752
33.5160	-0.2711	0.0806	34.7540	-1.6457	0.3956
38.9290	-1.0677	0.2861	39.7540	0.0354	0.0856
40.5790	0.3372	0.0802	43.4960	0.4287	0.0145
44.3210	0.4037	0.0166	45.1460	0.4069	0.0170
48.4960	0.3761	0.0608	49.3210	0.3069	0.0736
50.1460	0.3629	0.0835	53.4760	0.2946	0.0885
53.8890	0.2398	0.1070	54.7140	0.2604	0.1390
55.5390	0.1304	0.2961	58.4760	0.2275	0.1878
59.3010	0.4377	0.1220	60.5390	0.3771	0.1775

400 MeV

Angle	Asymmetry	error	Angle	Asymmetry	error
2.8590	0.1380	0.0303	3.6520	0.1897	0.0333
4.4460	0.3417	0.0356	5.4170	0.4339	0.0262
5.9460	0.4785	0.0268	7.1720	0.5272	0.0342
8.1520	0.6973	0.0392	8.9460	0.6349	0.0436
10.1820	0.6627	0.0420	11.1520	0.5574	0.0434
12.1270	0.5278	0.0494	13.1920	0.3609	0.0638
14.7090	0.1322	0.0710	14.8300	-0.0104	0.0917
15.1270	0.0059	0.0650	15.3800	-0.1234	0.1162
15.9300	-0.6236	0.1704	16.4800	-0.8555	0.2575
17.1680	0.0855	0.0694	17.7090	0.3305	0.0640
18.4370	0.6151	0.0904	18.9870	0.8817	0.0691
19.5370	0.9740	0.0602	19.9500	0.9935	0.0532
20.5000	0.9522	0.0520	21.9670	0.8501	0.0396
23.0670	0.7081	0.0498	24.4170	0.6248	0.0409
25.5710	0.5096	0.0425	26.6170	0.3694	0.0523
27.9570	0.0583	0.0649	28.5070	-0.2032	0.0827
29.6070	-0.5878	0.1088	30.9570	-0.7167	0.0716
31.5070	-0.5130	0.0823	32.0570	-0.2243	0.0822
32.6070	0.1132	0.0830	33.4270	0.3151	0.1580
34.5270	0.5540	0.0831	35.6270	0.7960	0.0794
36.4270	0.7550	0.0716	38.0770	0.6504	0.0714
39.9870	0.5568	0.0918	41.0870	0.4556	0.1169
42.4170	0.3407	0.1010	42.9670	0.2621	0.1072
44.0670	0.0846	0.1727			

500 MeV

Angle	Asymmetry	error	Angle	Asymmetry	error
2.5290	0.1944	0.0348	3.1370	0.2071	0.0326
3.7460	0.2878	0.0344	4.0290	0.2456	0.0353
4.6370	0.3508	0.0377	5.2460	0.3146	0.0396

5.5090	0.3751	0.0333	6.1170	0.3735	0.0364
6.7260	0.3491	0.0392	6.9990	0.5267	0.0434
7.6070	0.4567	0.0480	8.2160	0.4852	0.0548
8.5390	0.4704	0.0367	9.1470	0.4229	0.0406
9.7560	0.5034	0.0482	10.0090	0.4009	0.0413
10.6170	0.3738	0.0485	11.2260	0.3468	0.0532
11.5090	0.3392	0.0310	12.1170	0.2621	0.0383
12.7260	0.2514	0.0445	13.0190	0.2793	0.0717
15.7260	0.7076	0.0350	16.0190	0.7658	0.0441
16.6270	0.8379	0.0448	17.2360	0.7717	0.0452
17.5190	0.7569	0.0383	18.1270	0.7687	0.0411
18.7360	0.6555	0.0424	18.9890	0.6523	0.0332
19.5970	0.6463	0.0368	20.2060	0.5652	0.0390